Title
Materials Science and Device Physics of 2-Dimensional Semiconductors

Author
Fang, Hui

Publication Date
2014

Peer reviewed|Thesis/dissertation

Materials Science and Device Physics of 2-Dimensional Semiconductors

By

Hui Fang

A dissertation submitted in partial satisfaction of the

requirements for the degree of

Doctor of Philosophy

In

Engineering - Materials Science and Engineering

in the

Graduate Division

of the

University of California, Berkeley

Committee in charge:

Professor Ali Javey, Co-chair
Professor Ramamoorthy Ramesh, Co-chair
Professor Junqiao Wu
Professor Eli Yablonovitch

Spring 2014

Abstract

Materials Science and Device Physics of 2-Dimensional Semiconductors

by

Hui Fang

Doctor of Philosophy in Engineering - Materials Science and Engineering

University of California, Berkeley

Professor Ali Javey, Co-chair
Professor Ramamoorthy Ramesh, Co-chair

Materials and device innovations are the keys to future technology revolution. For MOSFET scaling in particular, semiconductors with ultra-thin thickness on insulator platform is currently of great interest, due to the potential of integrating excellent channel materials with the industrially mature Si processing. Meanwhile, ultra-thin thickness also induces strong quantum confinement which in turn affect most of the material properties of these 2-dimensional (2-D) semiconductors, providing unprecedented opportunities for emerging technologies.

In this thesis, multiple novel 2-D material systems are explored. Chapter one introduces the present challenges faced by MOSFET scaling. Chapter two covers the integration of ultrathin III-V membranes with Si. Free standing ultrathin III-V is studied to enable high performance III-V on Si MOSFETs with strain engineering and alloying. Chapter three studies the light absorption in 2-D membranes. Experimental results and theoretical analysis reveal that light absorption in the 2-D quantum membranes is quantized into a fundamental physical constant, where we call it the quantum unit of light absorption, irrelevant of most of the material dependent parameters.

Chapter four starts to focus on another 2-D system, atomic thin layered chalcogenides. Single and few layered chalcogenides are first explored as channel materials, with focuses in engineering the contacts for high performance MOSFETs. Contact treatment by molecular doping methods reveals that many layered chalcogenides other than MoS_2 exhibit good transport properties at single layer limit. Finally, Chapter five investigated 2-D van der Waals heterostructures built from different single layer chalcogenides. The investigation in a WSe_2/MoS_2 hetero-bilayer shows a large Stokes like shift between photoluminescence peak and lowest absorption peak, as well as strong photoluminescence intensity, consistent with spatially indirect transition in a type II band alignment in this van der Waals heterostructure. This result enables new family of semiconductor heterostructures having tunable optoelectronic properties with customized composite layers and highlights the ability to build van der Waals semiconductor heterostructure lasers/LEDs.

To my parents, my sister, Fang, and my wife, Sophia

Table of Contents

Acknowledgement

First and foremost, I would like to thank my Ph.D. advisor Prof. Ali Javey. Nothing in this thesis can be achieved without his guidance and spurring over the past five years. I have learned not only a great deal of knowledge from him, but also how to become a better researcher, a team-player, and a leader. For that I am eternally indebted. His broad vision, constant enthusiasm, and extremely hard working have set a very high bar for me to always look up to. It has been truly an honor and luck for me to have the chance being with him for five years of my life.

I have been also extremely lucky to have an eminent group of other mentors. I would like to first thank Prof. Eli Yablonovitch for all his advice, inspiration and support. Furthermore, I would like to thank Prof. Chenming Hu, Prof. Roya Maboudian and Dr. Carlo Carraro for their support and education during my Ph.D. study as well. I would also express my great appreciation to Prof. Ramamoorthy Ramesh for serving as my advisor in the MSE department, and Prof. Junqiao Wu, Prof. Daryl Chrzan, Prof. Tsu-Jae King Liu and Prof. Eli Yablonovitch for serving on my qualifying exam committee and helping me refining my research. And I would like to acknowledge the fruitful collaborations between us and Prof. Andrew Minor's group and Prof. Charles Fadley's group on further understanding the lattice and electronic structure for the chalcogenide heterostructures, Prof. Jing Guo's group of UFL on the theoretical modeling for the surface charge transfer for contact engineering.

Next, I would like to thank all the senior researchers in the Javey lab, with whom I have the opportunity to work, most of who are now professors. I would like to particularly thank Prof. Johnny Ho, Prof. Zhiyong Fan, Prof. Yulun Cheuh, Prof. Kuniharu Takei, Prof. Hyunhyub Ko, Prof. Morten Madsen, Prof. Junghyo Nah, Prof. Chuan Wang, Prof. Rehan Kapdia, Dr. Corsin Battaglia, Dr. Zhibin Yu, Dr. Yuping Zeng, and Dr. Toshitake Takahashi. Moreover I would like to thank my fellow graduate researcher in the Javey lab, especially to Steven Chuang, Maxwell Zheng, Mahmut Tosun, Sujay Desai and Mark Hettick. Finally, I want to thank the undergraduates who I had the honor to mentor and work with, Ting-Chia (Jerry) Chang, Peida (Peter) Zhao, Jeongseuk (Louis) Kang and David Huang. They are all talented students and I wish them big success in their graduate schools.

Finally, I would like to thank my parents, my sister and my wife. To them I dedicate this thesis.

Chapter 1 Introduction

1.1 The need for materials and device innovation for future scaling

Silicon integrated circuit (IC) technology has been benefiting for over 5 decades from a so called "smaller is better" motto. As the MOSFETs scale down in their dimensions, more and more transistors can be packed into a single chip, yielding the exponential increase in the device density and therefore the same trend in chip functionality. At the same time, the performance of transistors also boost with device miniaturization, by lowering the supply voltage needed to deliver certain ON current, with an essential decrease in the gate delay and an increase in the clock frequency of the circuits. This scaling trend, which has been driven by apparent economic reasons, is usually generalized as the Moore's Law, where Gordon Moore observed and predicted in 1965 that the chip functionality doubles approximately every 18 months. The evolution of many aspects of the digital integrated circuits have been tied with Moore's law, such as the clock frequency, the capacity of memory devices and even the number of pixels in digital cameras. This phenomenological law is still used in today's semiconductor industry to guide the product research and development.

As the channel length entered into nanometer regime, conventional bulk MOSFETs would suffer from various short channel effects due to inefficient gate control over the regions far away from the gate. The competing drain electrostatic control would consequently roll off the threshold voltage (V_T), increase the OFF current, worsen the Subthreshold Swing (SS), and eventually, turn the transistor into a not functional switch. This electrostatic control challenge is more severe when the channel length is ultra-scaled for bulk MOSFETs.

On the other hand, the power density of the chip has increased drastically with continued scaling. This was not an issue at the constant field scaling stage, when transistor dimensions (width, W,

and length, L), gate dielectric thickness (t_{ox}) and the supply voltage (V_{DD}) as well as the threshold voltage (V_T) are scaled by the same scaling factor 1/k (k > 1, W' = W/k). As a result, the device density is scaled by the factor k^2, the gate capacitance is scaled by 1/k, the drive current of the transistor is scaled by 1/k, and power dissipation per device is scaled by $1/k^2$. The increase in the device density while decrease in power per device cancels out, resulting in non-scaling for the power density. And this has a huge technological implication since packaging of the scaled device does not require more rigorous heat-sinking. But due to the tolerance for the OFF current, a high enough V_T is needed therefore V_T cannot be scaled down with the same scaling factor. Consequently the supply voltage V_{DD} stops scaling as aggressively as the device dimensions. As shown in Fig. 1.1, the V_{DD} scaling has slowed down quite drastically since year 2001, and this lagging has caused continuous increase for the power density and increasing burden for heat dissipation.

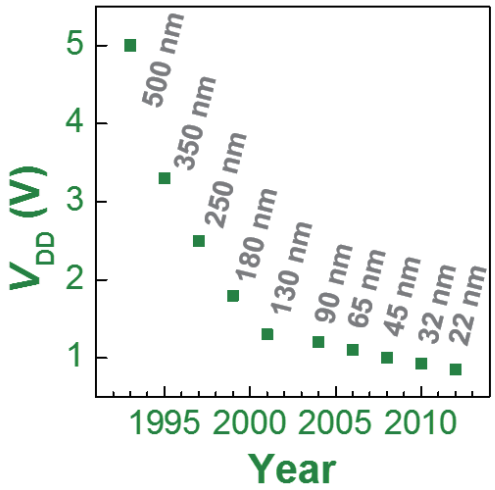

Figure 1.1. Supply voltage scaling as a function of year for the past two decades (1992-2012). The technology nodes are also labeled for each year. The data is acquired from the International Technology Roadmap for Semiconductors (ITRS).

To overcome the electrostatic and power challenges during scaling, global research efforts have been devoted by engineers and scientists, with emphasis on innovations in new materials from semiconductors, metals to dielectrics, and novel device structures. To solve the electrostatic problem at very short channel length, two novel device architectures have been proposed and later on implemented in chips, ultrathin body (UTB) silicon-on-insulator (SOI) technology and FinFET technology. The ideas behind these two innovations are the same, to eliminate the part of the channel father away from the gate then the drain, with UTB SOI technology being a planar gate structure, while FinFET a 3D tri-gate configuration. Alternatively, new channel materials are also intensively explored to potentially replace Si for high performance/low power MOSFETs. They range from organic molecules, carbon nanotube, III-V nanowires, to graphene etc. Key transport metrics such as carrier mobilities and saturation velocities are investigated and integrating these materials with Si platform are studied in parallel.

1.2 New science and opportunities from material dimension miniaturization

As the material dimensions scale, especially when the material enters nanometer regime, the electrons often "feel" structural quantum confinement and the electronic states are therefore quantized. These new discontinuous electronic states can be solved from the Schrodinger's equation with applicable boundary conditions, and they form electronic subbands along the none-quantized reciprocal direction. Figure 1.2 illustrates the conduction and valence (including both heavy hole, hh, and light hole, lh) subbands dispersion in the not confined direction.

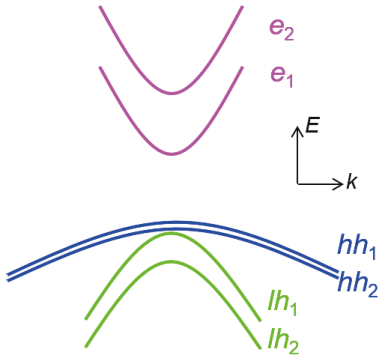

Figure 1.2. Illustration of electronic subbands at reduced dimensions. e_1, e_2, hh_1, hh_2, lh_1, and lh_2 are the indexes for the conduction and valence subbands.

The quantization effects have been observed in a lot of reduced dimensional materials, including 0-D quantum dots, 1-D quantum wires, and few-layer graphite previously, and they have remarkable influence upon nearly all of the material's properties, from physical to chemical. Using quantum dots as an example, it has been found that the fluorescence of quantum dots can be tuned from infrared to ultraviolet just by changing the diameter of the dots only. This influence in the material properties provides new opportunities for new technologies, and has been manipulated and utilized in different kinds of applications such as LED technology, bio-detection, memory devices, and thermoelectric devices and so on.

1.3 Summary

In this thesis, multiple novel 2-D material systems are explored. First, free standing ultrathin III-V is studied to enable high performance III-V on Si MOSFETs with strain engineering, followed by the light absorption study revealing the interband optical transition in the 2-D III-V quantum membranes. Next, single and few layered chalcogenides are explored, with focuses in engineering the contacts for high performance MOSFETs. Finally, 2-D van der Waals heterostructures built from different single layer chalcogenides are presented. These material systems are all in ultrathin body form, ensuring good electrostatic control of using them as channel materials. Meanwhile, strong quantum confinement effects are affecting their material properties, among which the optoelectronic property is mainly investigated here.

Chapter 2 Ultra-Thin III-Vs on Si for Next Generation Electronics

2.1 Introduction

Global research efforts have been devoted by engineers and scientists to overcome various challenges during transistor scaling, with emphasis on innovations in new materials and novel device structures. To solve the electrostatic problem at very short channel length, FinFET and UTB FET device architectures have been proposed and later on implemented in chips. The ideas behind these two innovations are the same, to eliminate the part of the channel father away from the gate, with UTB SOI technology being a planar gate structure, while FinFET a 3D tri-gate configuration. Material-wise, III-Vs are the major group of semiconductors explored to potentially replace Si for high performance/low power MOSFETs. Key transport metrics such as carrier mobilities and saturation velocities are investigated and integrating these materials with Si platform are studied in parallel.

Recently, the epitaxial layer transfer (ELT) of ultrathin (thickness, h_{InAs}=8-48 nm) InAs layers on Si/SiO_2 substrates was demonstrated by our group, which realized heterogeneous integration of ultra-thin III-V semiconductors on Si substrates bypassing complex heteroepitaxial growth processes. This essentially combines the materials and device innovation and presents a promising route for future scaling. In this chapter, strain engineering within the III-V on insulator (XOI) platform will be first presented, then the XOI concept is extended $InAs_xSb_{1-x}$ as a demonstration of even higher mobility III-V FETs, especially for ultrathin body thicknesses of <10 nm which are required for scaled transistors.

2.2 Strain engineering of epitaxially transferred, ultrathin layers of III-V semiconductor on insulator*

III-V compound semiconductors have been extensively explored in the recent years for energy-efficient and high-speed electronics due to their high electron mobility and saturation drift velocity[1-6]. In this aspect, ultrathin, fully-depleted layers are desired to reduce device leakage (i.e., OFF-state) currents, especially since many high mobility III-V semiconductors exhibit small bandgaps. Recently, the epitaxial transfer[6-10] of ultrathin (thickness, h_{InAs}=8-48 nm) InAs layers on Si/SiO_2 substrates was demonstrated by our group with the subsequently fabricated field-effect transistors (FETs) exhibiting excellent electrical properties[6]. This compound semiconductor on insulator (termed XOI) technology presents a viable route towards the heterogeneous integration of III-V semiconductors on Si substrates without the use of complex heteroepitaxial growth processes which often result in high defect densities due to the large lattice mismatch of the associated materials[11]. Of particular importance for device optimization is to explore the strain state of the XOI layers, and more crucially, to control it since strain plays a critical role in the electronic properties of materials[12]. Specifically, strain directly tailors the band offsets and carrier mobility by lifting the degeneracy in the bands which have been thoroughly investigated for heteroepitaxially grown multilayers[12-14]. In this paper, we investigate the strain state of ultrathin InAs XOI layers and demonstrate strain engineering by the use of a ZrO_x capping layer during the epitaxial transfer process.

The fabrication process for the InAs XOI substrates is shown schematically in Fig. 2.1(a) as previously reported in ref. 6. Briefly, InAs thin films (h_{InAs}=10-20 nm) were grown epitaxially on a 60 nm thick $Al_xGa_{1-x}Sb$ (x=0.2-1) sacrificial layer on GaSb (001) substrates. The ultrathin InAs layers were lithographically patterned (width of 350 nm to 5 μm) and wet etched using a mixture of citric acid (1 g/ml in DI H_2O) and hydrogen peroxide (30%) at 1:20 volume ratio. Subsequently, the AlGaSb sacrificial layer was selectively etched in ammonium hydroxide (1.5%, in deionized H_2O) solution with a measured etch rate of 40-60 nm/min depending on the Al composition of the sacrificial layer. The partially released InAs micro- or nano-ribbons (Fig. 2.1(b)) were transferred onto Si/SiO_2 receiver substrates using an elastomeric polydimethylsiloxane (PDMS) substrate (~2 mm thick). In order to engineer the strain of transferred InAs layers, a ZrO_x (or SiO_x) capping layer was deposited by electron-beam evaporation on top of the source wafer prior to the epitaxial transfer process (Fig. 2.1(a)). ZrO_x was chosen as the cap material because 1) ZrO_x is known to have a good interface with InAs (ref. 6) which is beneficial for the eventual device fabrication and 2) ZrO_x has a large Young's modulus (130-250 GPa)[15]. The cap prevents the relaxation of strain in InAs during the XOI fabrication process as shown later in detail in this paper. Figures 2.1 (c) and (d) show the transmission electron microscopy (TEM) images of a fabricated InAs XOI substrate, clearly depicting the single-crystalline structure of the InAs layer (~17 nm thick) on an amorphous SiO_2 layer. No clear voids are evident at the InAs interfaces, although it should be warned that TEM analyzes only a small cross-sectional area.

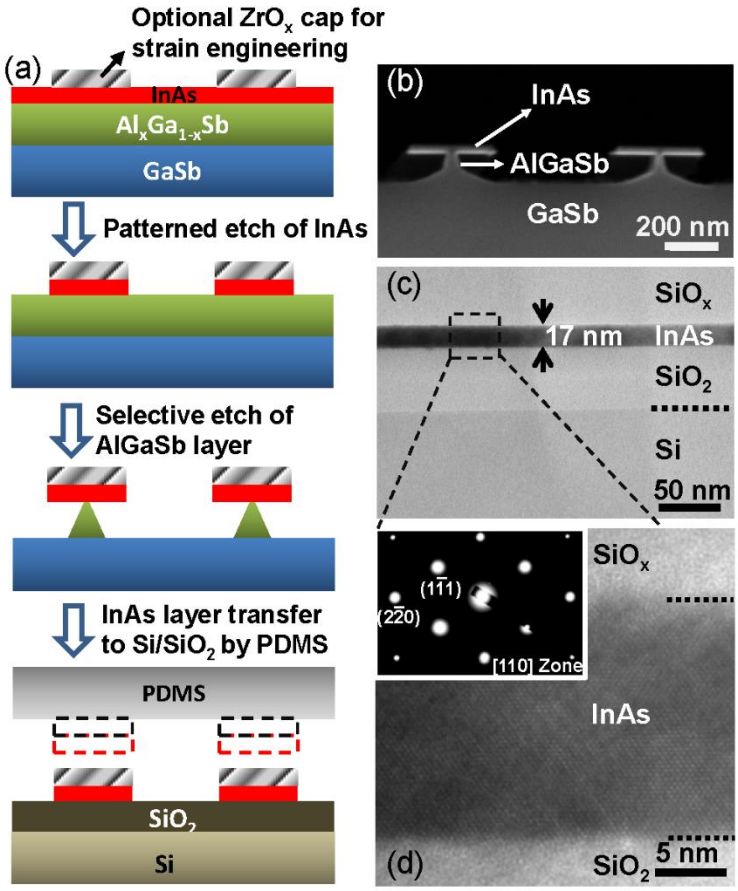

Figure 2.1. (a) The process schematics for epitaxial layer transfer of InAs thin films to Si/SiO_2 substrates. (b) Cross-sectional SEM image of InAs ribbons on the source wafer after the partial etch of the AlGaSb sacrificial layer and prior to the transfer. (c) and (d) Cross-sectional TEM images of a fabricated InAs XOI substrate. In this case, the InAs layer transfer was performed without the ZrO_x cap.

The structure of the source wafer is shown schematically in Figure 2.2(a), with both InAs and AlGaSb layers coherently strained to the GaSb (001) substrate as confirmed by high resolution X-ray diffraction (HRXRD). Specifically, we used Ω-2θ coupled scan, where Ω is the incident angle between the X-ray source and the sample and 2θ is the diffraction angle between the incident beam and detector, to resolve the (004) peaks from InAs, AlGaSb and GaSb and extract the out-of-plane (i.e., perpendicular) lattice parameters, $a_{\perp}$. Figure 2.2(b) shows the diffraction spectra taken from GaSb/$Al_{0.2}Ga_{0.8}Sb$/InAs source wafers with h_{InAs}=10, 15, and 20 nm, referenced to the peak of GaSb substrate, which has a (004) Bragg angle at 30.3±0.1°. Using Bragg's law $2d\sin\theta=n\lambda$, where d is the distance between the (004) crystal plane ($d=a_{\perp}/4$), n=1 and λ is the X-ray wavelength (Cu's Kα), one obtains $a_{\perp}$ ~6.02 and 6.11 Å for InAs and $Al_{0.2}Ga_{0.8}Sb$, respectively (Note that $a_{\perp,GaSb}$ ~6.10 Å, which is the bulk GaSb lattice parameter). From the equation $a_{\parallel}=C_{11}(a_0-a_{\perp})/2C_{12}+a_0$, where C_{11} and C_{12} are the elastic compliance constants[16] and a_0 is the bulk lattice parameter ($a_{0,AlxGa1-xSb}$=(6.0959+0.0396x) Å, $a_{0,InAs}$=6.0584 Å)[17], the in-plane lattice parameter $a_{\parallel}$ for both InAs and $Al_{0.2}Ga_{0.8}Sb$ layers is found to be ~6.10 Å, which is the same as that of GaSb (001). The experimental spectra also precisely match the simulation data (Fig. 2.2(b)), which assumes that both $Al_{0.2}Ga_{0.8}Sb$ and InAs layers are biaxially strained such that their in-plane lattice parameters are the same as that of the GaSb substrate (i.e. coherently). The result is consistent with the fact that the thicknesses of the AlGaSb sacrificial layer and the InAs layer are within their theoretical critical thicknesses for heteroepitaxy of h_c ~10.2 μm and 240 nm for $Al_{0.2}Ga_{0.8}Sb$ and InAs, respectively, which can be calculated from the empirical equation $h_c=(A/(\Delta a/a_0))^n$, where A=16 and n=2.4 for III-Vs[18], and Δa is the difference between $a_{0,AlxGa1-xSb}$ or $a_{0,InAs}$ and $a_{0,GaSb}$. The results are found to be generally true, regardless of the thickness of InAs and the Al content of the sacrificial layer used in this work. The amount of tensile strain inside the ultrathin InAs layer on the source wafers can be calculated by $\varepsilon_0=(a_{0,GaSb}-a_{0,InAs})/a_{0,InAs}$ ~0.62 %.

To visualize the strain state of the InAs layer in the XOI system (i.e., after transfer on Si/SiO_2 substrate), micro-Raman spectroscopy was employed. Note that the Raman spectroscopy could not be used for the analysis of the source wafer since InAs, AlGaSb, and GaSb have overlapping peaks. Figure 2.3(a) shows the Raman spectra of InAs XOI (h_{InAs}=20 nm) obtained from source wafers with different composition of $Al_xGa_{1-x}Sb$ sacrificial layers (x=0.2, 0.4 and 0.6) along with the [001] bulk InAs data from literature[19]. Here, no capping layer was used during the epitaxial transfer process. The spectra distinctly depict the first order transverse optic (TO) mode (~217 cm^{-1}), longitudinal optic (LO) mode (~239 cm^{-1}), and the low frequency branch of coupled LO-phonon-plasmon mode (L-) (~230-235 cm^{-1}) phonon peaks[19-21] of InAs XOI. Clearly, InAs XOI layers obtained from sacrificial layers with different compositions exhibit near identical Raman spectra, with the LO peak position at ~239 cm^{-1} which is the same as that for the InAs bulk substrate (Fig. 2.3(a)). Furthermore, the position of the LO peak is identical for InAs with thicknesses h_{InAs}=10-20 nm (Fig. 3(b)). The results suggest that in the absence of a ZrO_x capping layer, the strain is fully released during the epitaxial transfer process of InAs ultrathin layers for

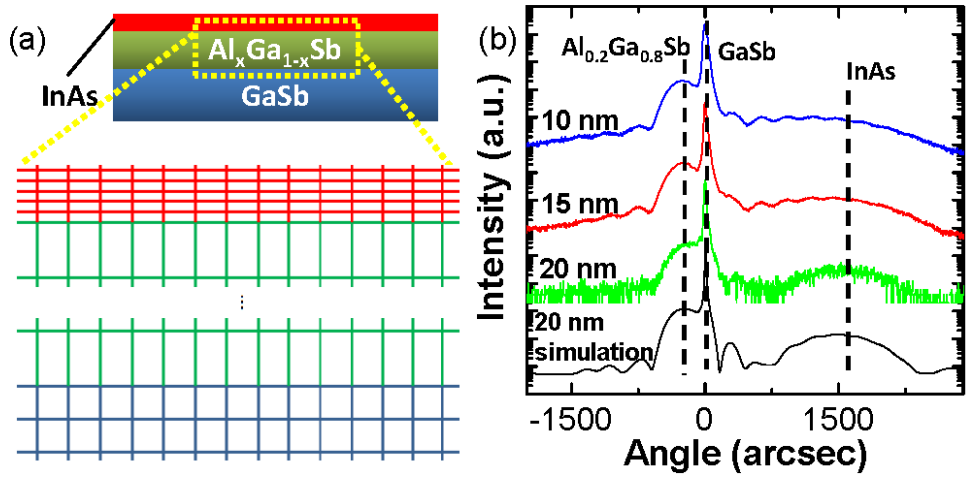

Figure 2.2. Analysis of the source wafers. (a) The structure of GaSb/AlGaSb/InAs source wafer with an assumed strain state for each layer. (b) HRXRD spectra and simulation spectrum of GaSb/$Al_{0.2}Ga_{0.8}Sb$/InAs source wafer with different InAs thicknesses.

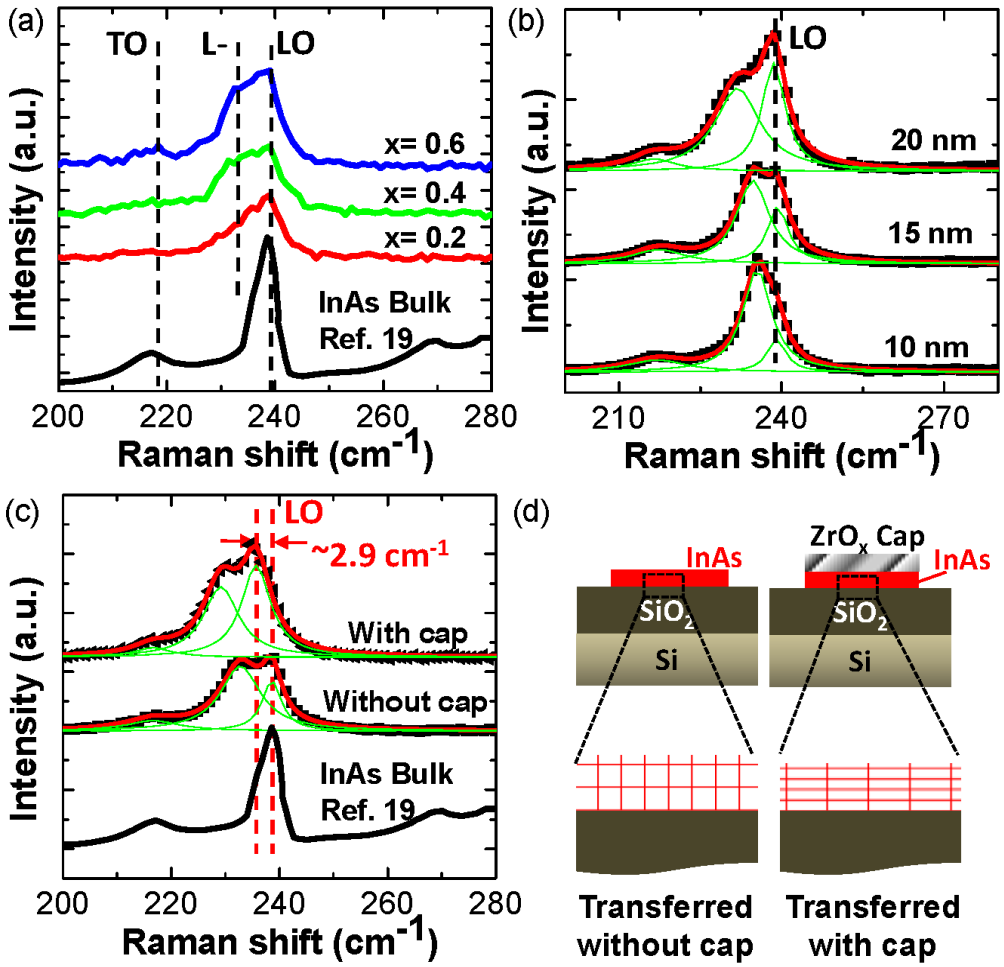

Figure 2.3. Analysis of epitaxial transferred InAs XOI substrates. (a) Raman spectra of XOI samples (h_{InAs}=20 nm) obtained from GaSb/$Al_xGa_{1-x}Sb$/InAs source wafers with different sacrificial layer Al content (x=0.2, 0.4 and 0.6). The Raman spectrum of a bulk InAs sample is replotted from reference 19. (b) Raman spectra of XOI samples with different InAs thicknesses. (c) Raman spectra of relaxed and strained InAs XOI samples when transferred with and without the use of a ZrO_x capping layer. Lorentzian fitting was performed to extract the exact peak locations of TO, L- and LO. (d) Schematic illustrations showing the lattices of relaxed and strained InAs XOI (not drawn to scale).

the explored thickness range and sacrificial layer composition. We hypothesize that the strain is released upon the partial etch of the AlGaSb layer, which results in nearly free-standing InAs layers (Fig. 2.1(b)). The L- peak, which is due to the surface plasmon-LO phonon coupling[21], however, exhibits a h_{InAs} dependence (Fig. 2.3(b)). One possible reason for the increasing L-/LO intensity ratio with reducing InAs thickness is due to the enhancement of the surface area to volume ratio. Note that the L- peak locations show some uncertainty because of different surface properties and scattering within the skin depth[21]. For all measurements, the intensity of the Raman laser power was decreased until the peak positions did not show any dependence on the laser intensity. This insured a more accurate estimation of the phonon peak locations, without laser-induced heating.

Strain engineering of InAs XOI layers was achieved by the use of a 70 nm thick ZrO_x cap layer during the transfer process (Fig. 2.1(b)). A red shift of 2.9±1.1 cm^{-1} in the LO peak position is clearly evident for InAs XOI layers transferred with a cap as compared to those without a cap (Fig. 2.3(c)). The amount of tensile strain inside the InAs XOI layer transferred with a cap was extracted from $\Delta\omega/\omega=(K_{11}/2)\varepsilon_{zz}+(K_{12}/2)(\varepsilon_{xx}+\varepsilon_{yy})$, where ω is the LO peak location (238.6 cm^{-1}), $\Delta\omega$ is the LO peak shift, K_{11} (-1.753×10^{11} dyn/cm^2) and K_{12} (-2.323×10^{11} dyn/cm^2) are the anharmonic spring constants for InAs LO phonon, and $\varepsilon_{xx}=\varepsilon_{yy}$, $\varepsilon_{zz}=-2C_{12}/C_{11}\varepsilon_{xx}$ are components of strain tensor inside InAs, with C_{11} (8.329×10^{11} dyn/cm^2) and C_{12} (4.526×10^{11} dyn/cm^2) as the elastic compliance constants of InAs[16,22]. From this analysis, we obtain an in-plane strain $\varepsilon_{xx}=\varepsilon_{yy}=0.8\pm0.3$ %, which is within the expected range of the ~0.62 % initial strain of the as-grown InAs layer. We note that besides preserving the initial strain of the transferred InAs layer, the ZrO_x cap may also induce additional strain depending on its initial stress level upon evaporation. Clearly, the presented approach shows, for the first time, a versatile route towards strain engineering of epitaxial transferred ultrathin layers of semiconductors.

To relate the amount of strain remaining in the InAs XOI layer to the ZrO_x cap thickness, analytical modeling was performed as shown in Fig. 2.4. For simplicity, it was assumed that the InAs and ZrO_x layers deform equally after release from the sacrificial layer and that the relationship between strain and stress is linear, given by Young's modulus E. Figure 2.4 (a) schematically illustrates the stress distribution across a cross-section of the ZrO_x cap and InAs layer. The stress in each layer can be found by setting a common absolute deformation value, and the relationship between these two stresses can be set by zeroing the net moment caused by them. The remaining strain inside InAs is then determined by the following equation: $\varepsilon=mn(n+2)\varepsilon_0/[1+mn(n+2)]$, where $m=E_{ZrOx}/E_{InAs}$ ~2.63 is the ratio of Young's moduli of ZrO_x and InAs, $n=h_{ZrOx}/h_{InAs}$ is the ratio of the thicknesses of ZrO_x and InAs, $\varepsilon_0=0.62\%$ is the as-grown InAs strain. The dependence of the strain (ε) in a 20 nm InAs layer on the cap thickness (h_{ZrOx}) is plotted in Fig. 2.4 (b). The modeling indicates that the initial InAs strain is nearly fully maintained (by up to ~98 %) by a 70 nm ZrO_x cap, which is consistent with the experimental observations.

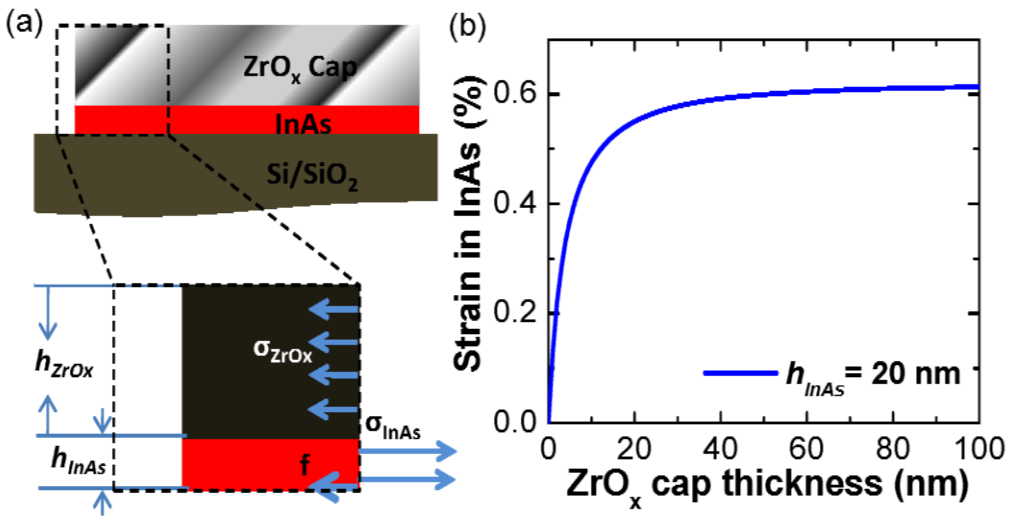

Figure 2.4. (a) Schematic of the stress distribution (σ_{ZrOx}, σ_{InAs} are the normal stresses in ZrO_x and InAs, respectively, f is the force applied to the InAs layer from the substrate to neutralize the total force) across a cross-section of ZrO_x cap and InAs layer. (b) The dependence of the strain (ε) in the transferred InAs layer (XOI configuration, h_{InAs}=20 nm) on the ZrO_x cap thickness (h_{ZrOx}).

In conclusion, the strain state of InAs layers within the XOI platform was studied. The strain is shown to fully relax during the epitaxial transfer process. However, if desired, a simple ZrO_x cap layer can be used to successfully preserve the strain of the epilayer transferred InAs. The results highlight that the strain of the X layer in XOI can be tuned by choosing different cap layers (with different Young's moduli), cap thicknesses and the initial stress inside the cap, to obtain the optimal strain level for the desired device application. The presented approach adds yet another degree of versatility to the use of epitaxial layer transfer technique of ultrathin semiconductors for practical applications.

References:

1. P. H.-S Wong. Solid-State Electron. **49**, 755 (2005).
2. R. Chau, B. Doyle, S. Datta, J. Kavalieros and K. Zhang. Nature Mater. **6**, 810 (2007).
3. M. Heyns and W. Tsai, Mater. Res. Soc. Bull. **34**, 485 (2009).
4. D-H. Kim and J. A. del Alamo. IEEE Trans. Electron. Dev. **57**, 1504 (2010).
5. M. Radosavljevic, B. Chu-Kung, S. Corcoran, M. K. Hudait, J. M. Fastenau, J. Kavalieros, W. K. Liu, D. Lubyshev, M. Metz, K. Millard, W. Rachmady, U. Shah and R. Chau, IEEE IEDM Tech. Digest 2009, 319 (2009)
6. H. Ko, K. Takei, R. Kapakia, S. Chuang, H. Fang, P. W. Leu, K. Ganapathi, E. Plis, H. S. Kim, S.-Y. Chen, M. Madsen, A. C. Ford, Y.-L. Chueh, S. Krishna, S. Salahuddin and A. Javey. Nature **468**, 286, (2010).
7. E. Yablonovitch, D. M. Hwang, T. J. Gmitter, L. T. Florez and J. P. Harbison, Appl. Phys. Lett. **56**, 2419 (1990).
8. D.-H. Kim, Y.-S. Kim, J. Wu, Z. Liu, J. Song, H.-S. Kim, Y. Y. Huang, K.-C. Hwang and J. A. Rogers. Adv. Mater. **21**, 3703 (2009).
9. N. A. Melosh, A. Boukai, F. Diana, B. Gerardot, A. Badolato, P. M. Petroff and J. R. Heath. Science **300**, 112 (2003).
10. M. Yokoyama, T. Yasuda, H. Takagi, N. Miyata, Y. Urabe, H. Ishii, H. Yamada, N. Fukuhara, M. Hata, M. Sugiyama, Y. Nakano, M. Takenaka, and S. Takagi. Appl. Phys. Lett. **96**, 142106 (2010).
11. H. Yonezu, Semicond. Sci. Technol. **17**, 762 (2002).
12. M. Chu, Y. Sun, U. Aghoram and S. E. Thompson. Annu. Rev. Mater. Res. **39**, 203 (2009).
13. M. M. Roberts, L. J. Klein, D. E. Savage, K. A. Slinker, M. Friesen, G. Celler, M. A. Eriksson and M. G. Lagally. Nature Mater. **5**, 388 (2006).
14. S. Suthram, Y. Sun, P. Majhi, I. Ok, H. Kim, H. R. Harris, N. Goel, S. Parthasarathy, A. Koehler, T. Acosta, T. Nishida, H.-H. Tseng, W. Tsai, J. Lee, R. Jammy and S. E. Thompson. VLSI Technology, IEEE Symposium on. pp. 182 (2002).
15. Materials Science and Engineering Handbook, Third Edition, pp.511 (CRC Press, 2001).
16. T. Mozume, Mat. Res. Soc. Symp. Proc. **324**, 285 (1994).
17. P. V. Neklyudov, S. V. Ivanov, B. Y. Mel'tser and P. S. Kop'ev, Semiconductors. **31**, 10 (1997).
18. S. Adachi, Properties of Semiconductor Alloys: Group IV, III-V and II-VI Semiconductors, pp. 39 (Wiley, 2009).
19. R. Carles, N. Saint-Cricq, J. B. Renucci, M. A.Renucci and A. Zwick, Phys. Rev. B. **22**, 10, (1980).
20. N. Begum, M. Piccin, F. Jabeen, G. Bais, S. Rubini, F. Martelli and A. S. Bhatti, J. of Appl. Phys.**104**, 104311 (2008).
21. S. Buchner and E. Burstein, Phys. Rev. Lett., **33**, 908 (1974).
22. J. Groenen, A. Mlayah, R. Carles, A. Ponchet, A. Le Corre and S. Salaun, Appl. Phys. Lett. **69**, 7 (1996).

2.3 Ultrathin-body, high-mobility InAsSb-on-insulator field-effect transistors*

High mobility semiconductors show great promise as the channel material of ultra-fast, low-power field-effect transistors (FETs) and have been actively explored in the past few decade[1-4]. Among them, mixed anion $InAs_xSb_{1-x}$ has one of the highest electron mobilities and saturation velocities of all known semiconductors[5]. However, it also has one of the smallest bandgaps[5-6]. For such devices, ultrathin body (UTB) architectures are essential to enable acceptable leakage currents. Conventionally, $InAs_xSb_{1-x}$ devices have been fabricated as complex quantum well structures on III-V or Si substrates. While the devices exhibited promising initial results, due to leakage from gate and/or not fully depleted body, they suffered from high I_{OFF}[7-10]. In consideration of supporting substrates, Si is a well-established material and is highly preferred over III-V semiconductors. However, using direct MBE growth to integrate both n and p channel materials onto Si for CMOS will be very challenging due to the large lattice mismatch between different desired materials and Si/SiO_2. Previously, we demonstrated the transfer of InAs ultra-thin membranes onto Si/SiO_2 substrates to form high performance n-FETs, termed "XOI" in analogy to the well-established Silicon-on-Insulator (SOI) field. The mobility of InAs XOI devices was found to be as high as ~5000 cm^2/Vs for body thicknesses of ~>20 nm and decreases to ~1600 cm^2/V-s when scaled down to 8 nm in thickness[11]. Here, we extend the XOI concept to $InAs_xSb_{1-x}$ as a demonstration of even higher mobility III-V FETs, especially for ultrathin body thicknesses of <10 nm which are required for scaled transistors based on small bandgap semiconductors.

Firstly, ultrathin $InAs_{0.7}Sb_{0.3}$ layers of different thicknesses (T_{InAsSb}=7 and 17 nm) were transferred onto Si/SiO_2 substrates following the epitaxial layer transfer (ELT) technique described previously[11]. $InAs_{0.7}Sb_{0.3}$ was grown on a 60 nm $Al_{0.4}Ga_{0.6}Sb$ sacrificial layer on GaSb substrate by molecular beam epitaxy. The InAsSb layer was then pattern etched by using a mixture of citric acid (1 g/ml of water) and hydrogen peroxide (30%) at 1:20 volume ratio (etch rate, ~0.7 nm/sec), and the AlGaSb layer was selectively etched by ammonium hydroxide (1.5%, in water). Ni (T_{Ni} = 40 nm) source (S) and drain (D) electrodes were fabricated using lithography and metallization. For top gated FETs, a 10 nm-thick ZrO_2 gate dielectric was deposited by atomic layer deposition (ALD) at 115 ºC, followed by a forming gas anneal at 150 ºC for 10 min. Subsequently, Ni top-gate (G) electrodes, overlapping the S/D, were fabricated. Fig. 2.5(a) shows a TEM image of the 7 nm InAsSb layer on Si/SiO_2 with a Ni/ZrO_2 high-κ stack, while the HRTEM image in Fig. 2.5(b) illustrates the single-crystallinity of the InAsSb channel, exhibiting highly abrupt interfaces between InAsSb and Si/SiO_2 without any visible voids.

In order to probe the electrical properties of InAsSb XOI FETs, back- and top-gated devices with varied gate lengths (L_G) were fabricated and characterized. For back-gated FETs, a 50 nm thick thermally grown SiO_2 was used as the gate dielectric. Fig. 2.6(a) shows the transfer characteristics of 7 nm and 17 nm thick InAsSb XOI FETs at V_{DS}=0.5 V, for L_G=2.7 μm and 3.4 μm, respectively. The back-gated 7 nm thick device exhibits an I_{ON}/I_{OFF} ratio of ~10^4, more than 2 orders of magnitude greater than the 17 nm device. This significant improvement in OFF current can be attributed to better electrostatic control from gating a thinner body[12]. The raising

* Reproduced with permission from Hui Fang *et al.,* IEEE Electron Device Letters, 33(4), 504-506, 2012.

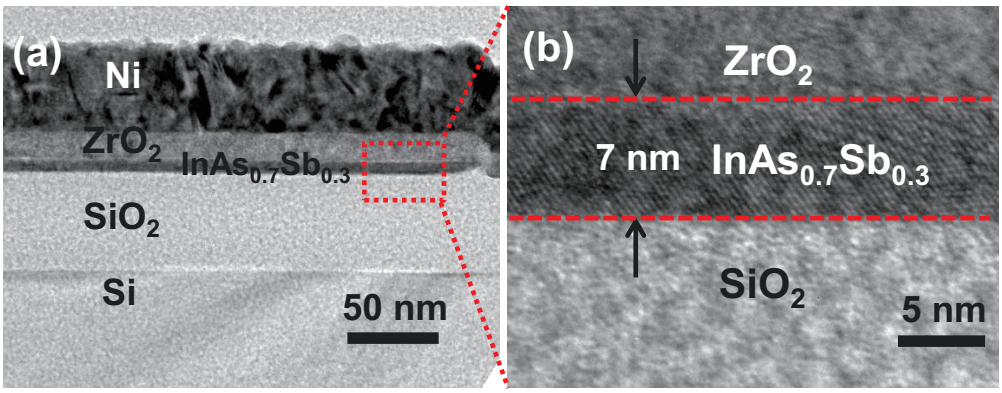

Figure 2.5. (a) TEM image of a ~7 nm thick $InAs_{0.7}Sb_{0.3}$ XOI (body oxide thickness, 50 nm) substrate. The nanoribbon is coated with a ZrO_2/Ni bilayer (~25 and ~50 nm, respectively). (b) HRTEM image showing the single-crystal structure of an $InAs_{0.7}Sb_{0.3}$ nanoribbon with atomicly abrupt interfaces with ZrO_2 and SiO_2 layers on the top and bottom surfaces, respectively

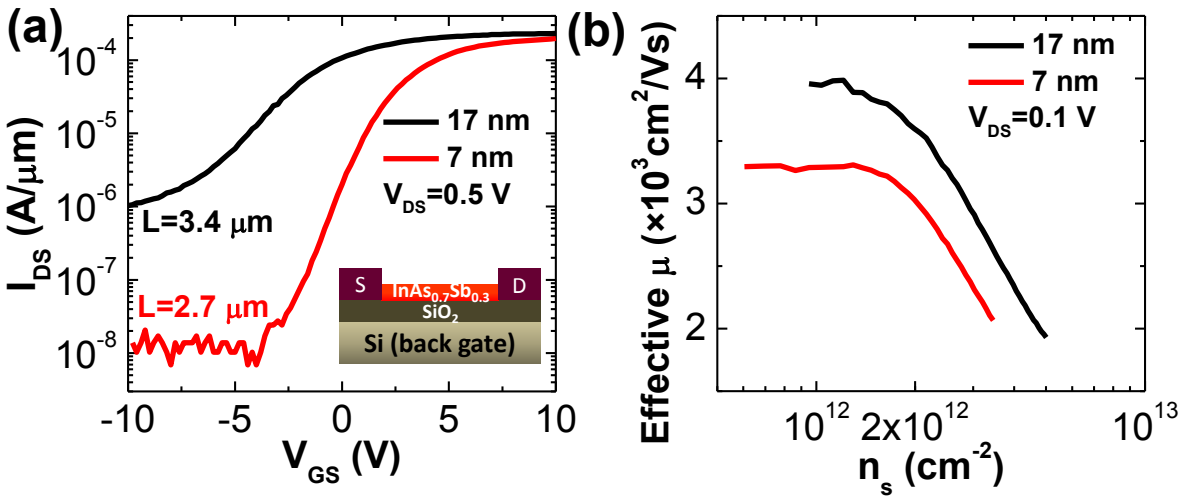

Figure 2.6. (a) Typical back gate I_{DS}-V_{GS} for 7 nm and 17 nm thick $InAs_{0.7}Sb_{0.3}$ XOI n-FET on 50 nm SiO_2 at V_{DS}= 0.5 V. The inset shows the schematic of the back gated devices. (b) Effective mobility extracted from I_{DS}-V_{GS} characteristics at V_{DS}= 0.1 V.

of bandgap by confinement will also contribute to a lower OFF current, since the barrier for thermionic emission of carriers would be higher. Specifically, since InAsSb has a large Bohr radius (between 34 nm and 65 nm, which are for bulk InAs and InSb, respectively[13]), heavy quantum confinement is expected in ultra-thin body membranes. An approximate expression for the ground state energy of electrons and holes can be derived by solving the 1-D Schrodinger Equation for a finite potential well. The effective bandgap would be 0.6 eV and 0.32 eV for 7 nm and 17 nm $InAs_{0.7}Sb_{0.3}$, respectively. Fig. 2.6(b) shows the extracted effective mobilities (μ_{eff}) as a function of the 2D carrier density at V_{DS}= 0.1 V for the long-channel, back-gated FETs (with T_{ox}=50 nm) shown in Fig. 2.6(a). The mobility was obtained from the expression,

$$\mu_{eff} = \frac{\partial I_{DS}}{\partial V_{DS}} \frac{L_G}{C_{ox}(V_G - V_T - 0.5V_{DS})}$$

where V_T is the threshold voltage extracted from the linear I_{DS}-V_{GS} curve, $C_{ox} = \varepsilon_{ox}\varepsilon_0 / T_{ox}$ is the gate oxide capacitance per unit area (ε_{ox} ~3.9 is the dielectric constant of SiO_2, ε_0 is the vacuum permittivity, and T_{ox}=50 nm is the SiO_2 thickness). Here, we utilized the simple parallel plate model and the effects of quantum capacitance and fringe field are ignored, which is a valid assumption given the thick gate oxide (i.e., small oxide capacitance) of the back-gated devices and the channel width>>thickness.

The effective mobility histograms extracted for long-channel $InAs_{0.7}Sb_{0.3}$ (thickness, 7 nm and 17 nm) and InAs (thickness, 8 nm, and 18 nm) XOI FETs are shown in Fig. 2.7. Note that the dimensions (including channel width, W, typically ~320-380 nm) of each device was directly measured by SEM and used to normalize the current and extract mobilities. InAsSb devices exhibit average effective mobilities of ~3400 cm^2/V-s and ~4100 cm^2/V-s at n_s= 2×10^{12} cm^{-2} for 7 nm and 17 nm thicknesses, respectively. Note that the mobility degradation with thickness is mainly due to enhancement of surface roughness and surface polar phonon scattering[14]. These mobility values present ~2× enhancement over InAs XOI FETs with similar thicknesses (Fig. 2.7). The variation of the mobility may be caused by the different amount of interface trap states (D_{it}) introduced during processing. This mobility improvement coincides with the previously reported Hall mobility difference between $InAs_{0.7}Sb_{0.3}$ (μ_{Hall}~42,000 cm^2/V-s) and InAs (μ_{Hall}~22,000 cm^2/V-s)[15] at a doping concentration of 5×10^{16}-3×10^{17} cm^{-3}, which is around the electron density in our unintentionally doped samples. Hence it is promising to further enhance the mobility by increasing the Sb content of the channel, although this comes at the cost of a lower band-gap.

Next, the electrical properties of top-gated InAsSb XOI FETs are explored. As shown in Fig. 2.8(a) and (b), a 7 nm thick InAsSb FET (L_G=500 nm) exhibits I_{ON}/I_{OFF} ~2×10^2 when defining I_{OFF} at V_T-1/3V_{DD} and I_{ON} at V_T+2/3V_{DD} at room temperature (V_T is taken at I =10^{-6} A/μm), and exhibits an I_{ON} of ~0.38 mA/μm at V_{DS}=V_{GS}=0.6 V. A subthreshold swing of SS ~178 mV/dec is obtained, which is larger than that of InAs FETs (SS ~125 mV/dec)[16]. This suggests that the InAsSb interfaces exhibit a higher density of trap states than InAs. The source contact resistance, R_S, of the 7 nm thick InAsSb was extracted using the Transmission Line Method. The extracted R_S is ~200 Ω.μm, which is close to that of 8 nm InAs FETs' (~230 Ω.μm)[16].

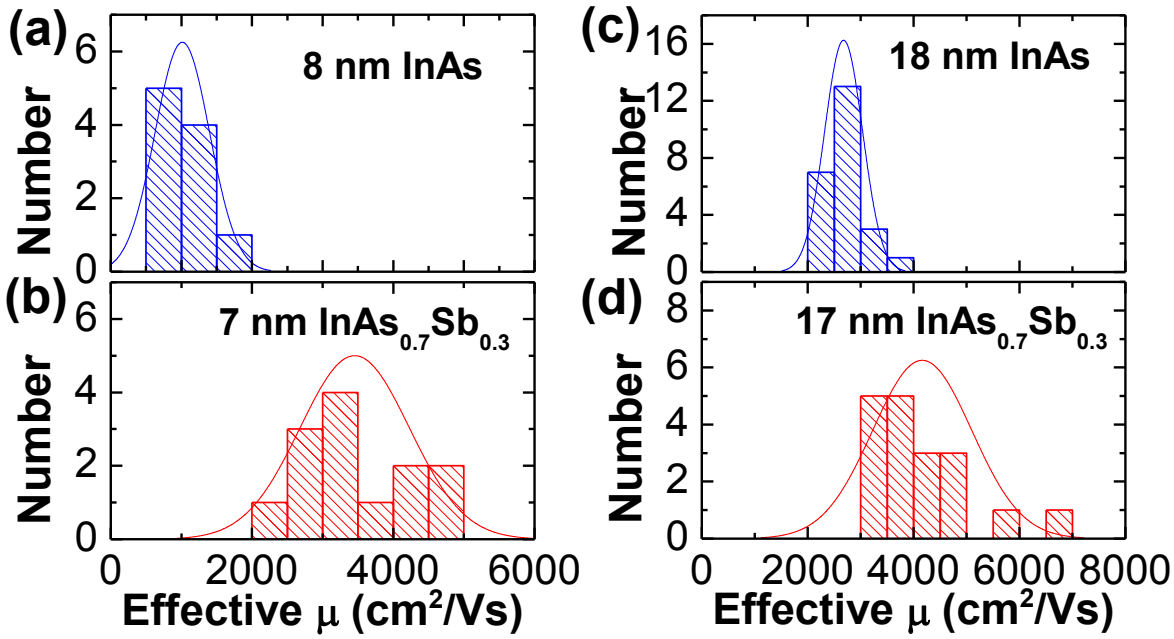

Figure 2.7. Histogram plots of effective mobility (at $n_s = 2\times10^{12}$ cm^{-2}) in InAs and InAsSb XOI n-FETs of (a) T_{InAs}=8 nm, (b) $T_{InAs0.7Sb0.3}$=7 nm (c) T_{InAs}=18 nm, and (d) $T_{InAs0.7Sb0.3}$=17 nm.

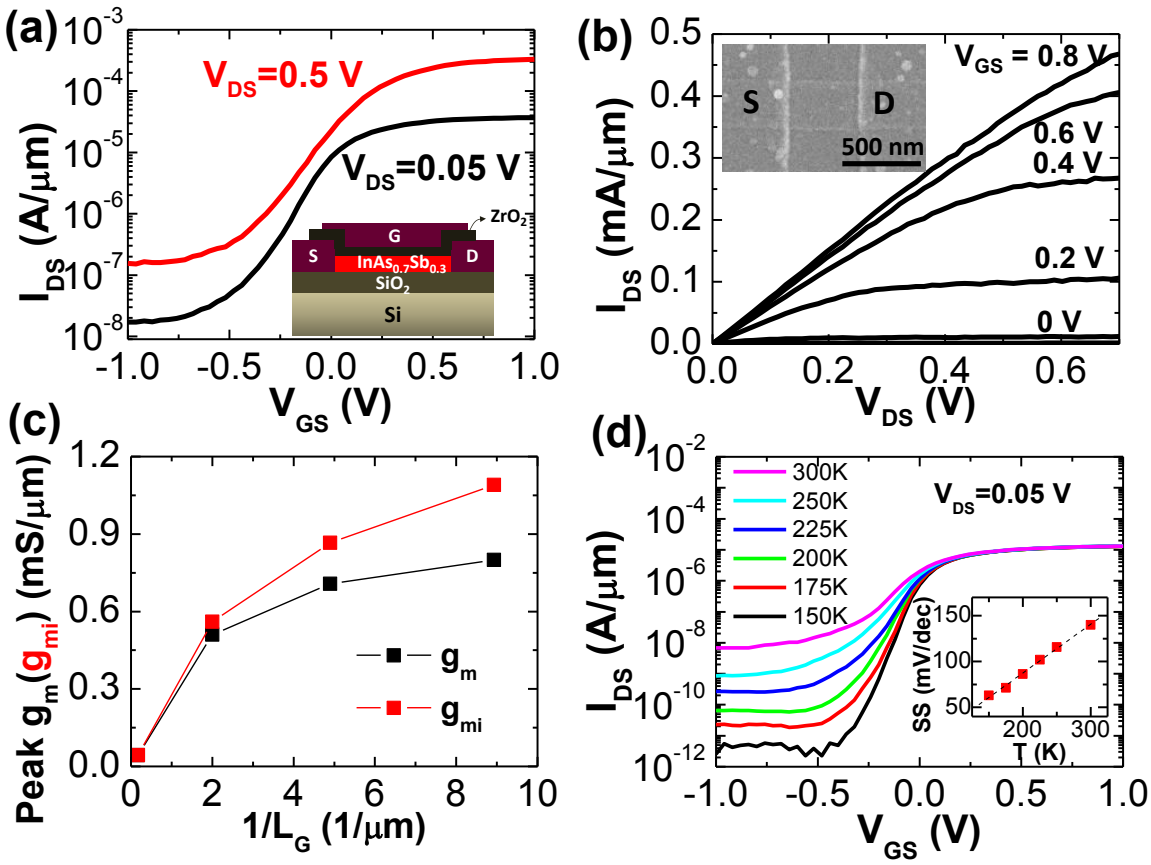

Figure 2.8. (a) Top gate I_{DS}-V_{GS} for a 7 nm thick $InAs_{0.7}Sb_{0.3}$ XOI n-FET at V_{DS}= 0.05 and 0.5 V. The gate length is ~500 nm. Inset is schematic of top gated InAsSb XOI FETs. (b) I_{DS}-V_{DS} curve of the same device in (a). Inset shows the top view SEM image (false-color) of a representative device. (c) g_m and g_{mi} as a function of the gate length. (d) Top gate I_{DS}-V_{GS} as a function of temperature at V_{DS}=0.05 V. Inset shows SS as a function of T, with linear fitting.

The extrinsic transconductance g_m of the top-gated FET (L_G~500 nm) at V_{DS}=0.5 V, peaked at ~0.51 mS/μm. The intrinsic transconductance,

$$g_{mi} = g_m/(1 - g_m R_S - g_d R_{SD})$$

was extracted to exclude the contact resistance effects ($R_{SD}=R_S+R_D=2R_S$). The peak intrinsic transconductance of the device is ~0.56 mS/μm. Fig. 2.8(c) shows g_m and g_{mi} as a function of inverse gate length, which exhibits non-linearity for shorter channel lengths, possibly arising from quasi-ballistic transport. Further study need to be done to improve the I_{OFF} and SS of sub-500nm channel length devices. Compared to previously reported $InAs_{0.8}Sb_{0.2}$ QWFETs (L_G=1 μm, g_{mi}=0.50 mS/μm) on GaAs substrates and InSb QWFETs (L_G=85 nm, g_{mi}=0.71 mS/ μm) on Si, our InAsSb XOI FETs show a peak g_{mi} of ~0.56 mS/μm for L_G~500 nm (Fig. 2.8(c)) while eliminating the complexity from growing thick buffer and δ doping layers[9-10]. And it has higher I_{ON}/I_{OFF} at room temperature.

Fig. 2.8(d) shows the temperature dependent transfer characteristics. The interface trap density (D_{it}) was extracted from $D_{it} = C_{it}/q^2$, with C_{it} from,

$$\frac{dSS}{dT} = \frac{2.3k}{q}\left(1 + \frac{C_{it}}{C_{ox1}} + \frac{C_{InAsSb}}{C_{ox1}} - \frac{\frac{C_{InAsSb}^2}{C_{ox1}C_{ox2}}}{1 + \frac{C_{it}}{C_{ox2}} + \frac{C_{InAsSb}}{C_{ox2}}}\right)$$

With ε_{ox1}= 16, t_{ox1}= 10 nm, ε_{ox2}= 3.9, t_{ox2}= 1200 nm, ε_{InAsSb}= 15.7, and t_{InAsSb}= 7 nm, D_{it} is determined to be ~1×10^{13} cm^{-2} eV^{-1}, which is slightly higher than that of InAs XOI FETs' (~3×10^{12} cm^{-2} eV^{-1})[16]. Note that this D_{it} value presents only a rough estimate of the order of magnitude for the average trap density within the bandgap. The traps close or beyond the conduction band edge are not extracted using this analysis technique, but they can also alter the charge carrier density and transport properties. Detailed capacitance-voltage characterization in the future is needed to better understand and optimize the surface/interface properties.

In conclusion, high electron mobility $InAs_{0.7}Sb_{0.3}$ transistors have been fabricated on Si substrates using the XOI configuration. The devices exhibit excellent electrical properties, while future work on improving the InAsSb/high K interface need to be done. In the future, even higher Sb content and thinner body InAsSb XOI n-FETs, together with InGaSb XOI p-FETs are promising to be integrated for high speed and low power complementary MOSFET circuits.

References:

1. R. Chau, S. Datta, M. Doczy, B. Doyle, B. Jin, J. Kavalieros, A. Majumdar, M. Metz, and M. Radosavljevic, "Benchmarking Nanotechnology for High-Performance and Low-Power Logic Transistor Applications," IEEE Trans. Nanotech. Vol. 4, 2005, pp. 153-158.
2. D. A. Antoniadis, and A. Khakifirooz, "MOSFET Performance Scaling: Limitations and Future Options," IEEE IEDM Tech. Dig., 2008, pp. 1-4.
3. D.-H. Kim, and J. A. del Alamo, "Scalability of Sub-100 nm InAs HEMTs on InP Substrate for Future Logic Applications," IEEE Trans. Electron Devices Vol. 57, 2010, pp. 1504-1511.
4. Y. Xuan, Y. Q. Wu, T. Shen, T. Yang, and P. D. Ye, "High performance submicron inversion-type enhancement-mode InGaAs MOSFETs with ALD Al_2O_3, HfO_2 and HfAlO as gate dielectrics," IEEE IEDM Tech. Dig., 2007, pp. 637-640.
5. B. R. Bennett, R. Magno, J. B. Boos, W. Kruppa, and M. G. Ancona, "Antimonide-based compound semiconductors for electronic devices: A review," Solid State Electron. Vol. 49, 2005, pp. 1875-1884.
6. A. Ali, H. Madan, R. Misra, A. Agrawal, P. Schiffer, J. B. Boos, B. R. Bennett, and S. Datta, "Experimental Determination of Quantum and Centroid Capacitance in Arsenide–Antimonide Quantum-Well MOSFETs Incorporating Nonparabolicity Effect," IEEE Trans. Electron Devices Vol. 58, 2011, pp. 1397-1403.
7. B.-R. Wu, C. Liao, and K. Y. Cheng, "High quality InAsSb grown on InP substrates using AlSb/AlAsSb buffer layers," Appl. Phys. Lett. Vol. 92, 2008, pp. 062111-1–062111-3.
8. S. Datta, T. Ashley, J. Brask, L. Buckle, M. Doczy, M. Emeny, D. Hayes, K. Hilton, R. Jefferies, T.Martin, T. J. Phillips, D. Wallis, P. Wilding and R. Chau, "85nm Gate Length Enhancement and Depletion mode InSb Quantum Well Transistors for Ultra High Speed and Very Low Power Digital Logic Applications," IEEE IEDM Tech. Dig., 2005, Vol. 763.
9. A. Ali, H. Madan, R. Misra, E. Hwang, A. Agrawal, I. Ramirez, P. Schiffer, T. N. Jackson, S. E. Mohney, J. B. Boos, B. R. Bennett, I. Geppert, M. Eizenberg and S. Datta, "Advanced Composite High-κ Gate Stack for Mixed Anion Arsenide-Antimonide Quantum Well Transistors," IEEE IEDM Tech. Dig., 2010, pp.134-137.
10. T. Ashley, L. Buckle, S. Datta, M.T. Emeny, D.G. Hayes, K.P. Hilton, R. Jefferies, T. Martin, T.J. Phillips, D.J. Wallis, P.J. Wilding and R. Chau, "Heterogeneous InSb quantum well transistors on silicon for ultra-high speed, low power logic applications," Elec. Lett. Vol. 43, 2007.
11. H. Ko, K. Takei, R. Kapadia, S. Chuang, H. Fang, P. W. Leu, K. Ganapathi, E. Plis, H. S. Kim, S.-Y. Chen, M. Madsen, A. C. Ford, Y.-L. Chueh, S. Krishna, S. Salahuddin, and A. Javey, "Ultrathin compound semiconductor on insulator layers for high-performance nanoscale transistors," Nature Vol. 468, 2010, pp. 286-289.
12. Y.-k. Choi, K. Asano, N. Lindert, V. Subramanian, T.-j. King, J. Bokor and C. Hu, "Ultra-thin Body SO1 MOSFET for Deep-sub-tenth Micron Era," IEEE IEDM Tech. Dig., 1999, pp. 919-921.
13. H. T. Grahn, Introduction to Semiconductor Physics, Singapore: World Scientific, 1999, p. 121.
14. K. Takei, H. Fang, S. B. Kumar, R. Kapadia, Q. Gao, M. Madsen, H. S. Kim, C.-H. Liu, Y.-L. Chueh, E. Plis, S. Krishna, H. A. Bechtel, J. Guo, A. Javey. "Quantum Confinement

Effects in Nanoscale-Thickness InAs Membranes", Nano Letters, 2011, ASAP, doi: 10.1021/nl2030322.
15. D. Chattopadhyay, S. K. Sutradhar and B. R. Nag, “Electron transport in direct-gap III-V ternary alloys,” J. Phys. C: Solid State Phys., Vol. 14, 1981, pp. 891-908.
16. K. Takei, S. Chuang, H. Fang, R. Kapadia, C.-H. Liu, J. Nah, H. S. Kim, E. Plis, S Krishna, Y.-L. Chueh, and A. Javey, “Benchmarking the performance of ultrathin body InAs-on-insulator transistors as a function of body thickness,” Appl. Phys. Lett. Vol. 99, 2011, pp. 103507-1–1035073.

Chapter 3 Light Absorption Quantum in 2-D Materials

3.1 Introduction

As the material dimensions scale, especially when the material enters nanometer regime, there is often strong quantum confinement for electrons. The electronic states are therefore quantized, and these new discontinuous electronic states can be solved from the Schrodinger's equation with applicable boundary conditions. Electronic subbands therefore form along the none-quantized reciprocal direction.

The quantization effects have been observed in a lot of reduced dimensional materials, including 0-D quantum dots, 1-D quantum wires, and few-layer graphite previously, and they have remarkable influence upon nearly all of the material's properties, from physical to chemical. For example, it has been found that the fluorescence of 0D quantum dots can be tuned from infrared to ultraviolet just by changing the diameter of the dots only.

Previous work has shown that graphene, a 2-D semimetal, has a universal value of light absorption, namely $\pi\alpha$, where α is the fine structure constant. Here, we use free-standing InAs membranes with exceptionally small thickness as a model material system in order to accurately probe the absorption properties of 2-D semiconductors as a function of thickness. We demonstrate that the magnitude of the light absorption for all 2-D materials is an integer product of a quantum of absorptance, irrelevant of most material dependent parameters.

3.2 The quantum of optical absorption in two-dimensional semiconductors*

The optical properties of heterostructure quantum wells (QWs) have been extensively studied since the 1970's, in GaAs/AlGaAs (ref. 1), GaInAs/AlInAs (ref. 2, 3), InGaAs/InP (ref. 4) and HgCdTe/CdTe (ref. 5). Here we do a careful quantitative examination of the intrinsic absorption properties of free-standing 2-D semiconductor thin-films, which has previously been done only for layered structures, such as MoS_2 (ref. 6). (The criterion of real two dimensionality is that the material thickness be smaller than the electron Bohr radius.)

Previous work has shown that graphene, a 2-D semimetal, has a universal value of light absorption, namely $\pi\alpha$, where α is the fine structure constant[7]. Here, we use free-standing InAs membranes with exceptionally small thickness as a model material system in order to accurately probe the absorption properties of 2-D semiconductors as a function of thickness. We demonstrate that the magnitude of the light absorption is an integer product of a quantum of absorptance. Specifically, each set of interband transitions between the 2-D sub-bands results in a quantum unit of absorptance of $A_Q \approx \pi\alpha/n_c$, where n_c is the optical local field correction factor. The total absorptance for the first several sets of interband transitions is simply given as $A = MA_Q$, where M is the integer number of allowed transitions for a given photon energy. The result here appears to be universal, except for small correction factors associated with higher bands.

Recently, there has been a high level of interest in exploring the fundamental science[6-10] and associated devices[11-20] of free-standing (i.e., attached to a substrate by van der Waals or other weak forces) 2-D semiconductors. 2-D layered semiconductors, {e.g., MoS_2 (ref. 11), WSe_2 (ref. 15), GaSe (ref. 16), $Bi_2Sr_2CaCu_2O_x$ (ref. 17), Bi_2Se_3 (ref. 18) and Bi_2Te_3 (ref. 19); or diamond/zinc-blende structures InAs (ref. 12), and InGaSb (ref. 20)} can be readily mounted on virtually any support substrate, thereby enabling a wide range of novel device concepts and practical applications. In one example system, InAs quantum membranes (QMs) with adjustable thicknesses down to a few atomic layers have been realized by a layer transfer process onto a user-defined substrate[12]. The approach enables the direct optical absorption studies of fully-relaxed (i.e., unstrained)[21] 2-D III-V semiconductors by using transparent substrates, without the constraints of the original growth substrate[10]. Here, we utilize InAs membranes of thickness $L_z \sim$ 3nm-19nm on CaF_2 support substrates as a model material system for examining the absorption properties of 2-D semiconductors. Given the large Bohr radius of ~ 34nm[22] in bulk InAs, strong quantum confinement of carriers is readily obtained for sub-20 nm Quantum Membrane thicknesses. Note that there are only ~5 unit cells in a 3nm thick InAs QM, given its lattice constant of ~0.6nm (ref. 23). In such a quantum mechanically confined 2-D system, there is electronic band dispersion in the 2 unconfined directions, with discrete energy sub-band edges at values determined by quantum confinement[24] in the 3rd direction. In our case, the InAs QMs can be effectively treated as infinitely deep potential wells, since they are confined by air on one side and by a wide bandgap[25] CaF_2 substrate on the other side. Figure 3.1A shows the optical microscope image of a periodic array of ~5μm wide InAs strips (of ~3nm thickness), on a CaF_2

* Reproduced with permission from Hui Fang *et al.,* Proceedings of the National Academy of Sciences (PNAS), 110, 11688-11691, 2013. Copyright © [2013] NAS.

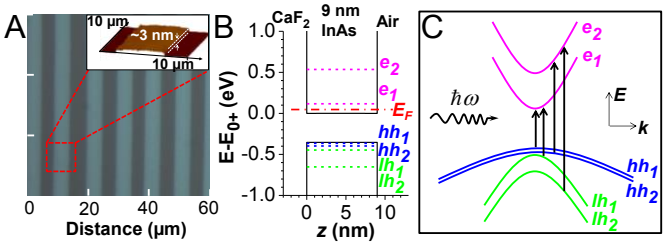

Figure 3.1. (A) Optical microscope image of InAs 2-D strips (~3nm thick) on a CaF_2 substrate. Inset shows the atomic force microscope image of a single InAs strip. (B) CaF_2/InAs (9nm)/Air quantum well band diagram with energy referring to $E(z=0^+)$. E_F shows the quasi Fermi level, while e_1, e_2, hh_1, hh_2, lh_1 and lh_2 are the indices for the conduction and valence subbands. Note that only the first two conduction/valence subband edges are shown. (C) Qualitative band structure schematic of a 2-D InAs QM, with arrows indicating the allowed optical interband transitions between valence and conduction sub-bands.

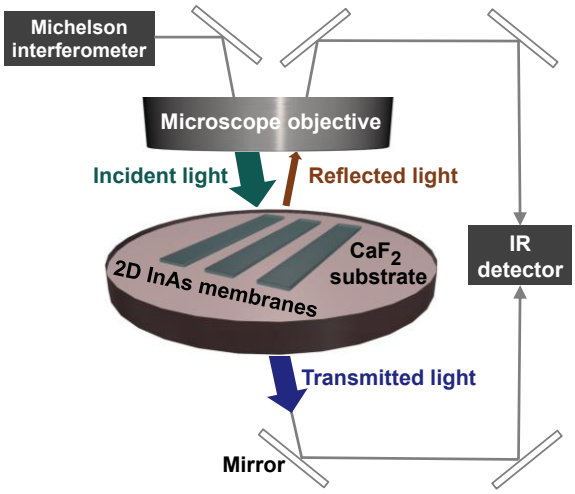

Figure 3.2. Schematic illustration of the FTIR micro-spectroscopy set-up used for the absorption measurements. The absorption spectrum is obtained from the measured transmission and reflection spectra. The incident light angle was actually perpendicular to the membrane.

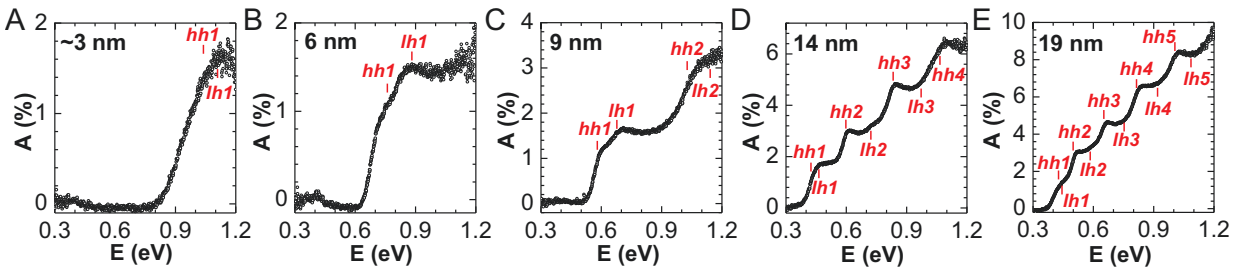

Figure 3.3. Absorptance for (A) 3nm, (B) 6nm, (C) 9nm, (D) 14nm, and (E) 19nm InAs quantum membranes. The absorptance spectra are corrected by dividing by the surface area fill factor of InAs.

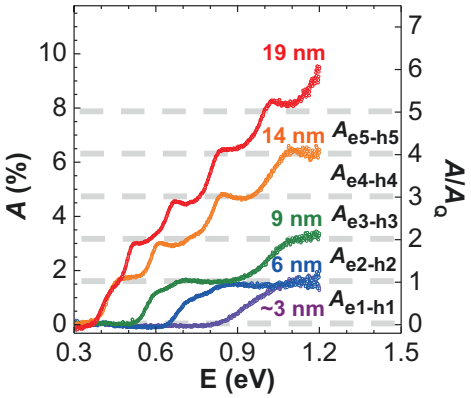

Figure 3.4. Absorptance spectra of InAs QMs with thickness of L_z ~ 3nm, 6nm, 9nm, 14nm, and 19nm at room temperature, showing universal absorptance steps of A_Q~1.6% in magnitude. Dash lines indicate each 1.6% of absorptance. The $A_{en\text{-}hn}$ represent the absorptance from the corresponding interband transitions, e_n-hh_n and e_n-lh_n.

crystal substrate produced by the layer transfer process[26]. CaF_2 was chosen as the support substrate as it is optically transparent for the wavelength range of interest. From visual appearance (Fig. 3.1A), it is evident that ultrathin InAs QMs exhibit strong optical contrast; thereby allowing for the detailed optical characterization even for the films consisting of a few atomic layers in thickness.

Fig. 3.1B shows the calculated energy levels of a 3nm InAs quantum membrane (QM) with CaF_2 and air boundaries. The MBE-grown InAs samples are not intentionally doped, eliminating band-filling[27]. Here, the effect of surface accumulation layers due to surface defects are ignored (see supplementary Fig. S1 for surface accumulation layer effects). Figure 3.1C depicts the qualitative band structure of a 2-D InAs QM, with vertical arrows indicating the interband transitions from the n^{th} heavy hole (hh)/light hole (lh) sub-band to the n^{th} electron (e) sub-band. Here we define e_n-hh_n and e_n-lh_n as the n^{th} set of interband transitions. Due to spatial matching of electron/hole wave-functions in different energy sub-bands, interband transitions in quantum wells are favored when $\Delta n=n'-n=0$, where n' and n are the sub-band indices for electrons and holes, respectively[28]. Consequently, there are two allowed transitions to each electron sub-band; one from the corresponding hh sub-band, and the other from lh sub-band.

We utilize Fourier Transform Infrared (FTIR) micro-spectroscopy (Fig. 3.2) to probe optical interband transitions (in the range $0.3eV< h\nu <1.2eV$) in InAs QMs at room temperature[26]. Transmittance and reflectance spectra were collected in the range of 2414-9656 cm^{-1} (0.30eV-1.20eV) over an aperture size of $\sim 50\times 50\mu m^2$, with $8cm^{-1}$ (1meV) resolution and 512 averages for all samples with different thicknesses. Atmospheric H_2O and CO_2 effects were removed using OMNIC 8.2 software (Thermo Scientific). The absorption spectra of InAs QMs for each thickness was obtained by subtracting the transmittance and reflectance from a normalized 100% spectrum yielding Fig. 3.3. The final spectra were generated by dividing the measured spectra by the fractional area fill factor of the InAs strips. Fig. 3.4 shows the overlayed absorptance (A) spectra of InAs QMs with $L_z \sim$ 3nm, 6nm, 9nm, 14nm and 19nm. Clear step-like features are observed in the absorptance spectra arising from the quantized interband transitions between the 2-D sub-bands[10]. The spacing between the measured absorptance steps are in quantitative agreement with the calculated interband energy spacings (see supplementary Fig. S2 for the detailed analysis). Note that intersubband transitions are negligible due to our TE polarization. The experimental finding here is that the individual absorptance steps plateau at ~1.6±0.2% (standard deviation) for all samples, regardless of the QM thickness. The result was reproducible for multiple samples and measurements.

To shed light on this observed absorption behavior, the electron-photon interaction in a semiconductor material is theoretically evaluated from Fermi's golden rule. If a light wave with electric field E, polarization vector $\hat{e}$ and frequency ω is incident perpendicular to a direct band-gap semiconductor membrane with a thickness L_z, in an infinitely deep potential well model[29], the optical absorption coefficient is:

$$\alpha'(\omega) = \frac{e^2}{n_r c \varepsilon_o m_o^2 \omega L_z \hbar^2} \frac{1}{1/m_{en}^* + 1/m_{hn}^*} \left|\hat{e}\cdot\vec{p}_{cv}\right|^2 \qquad \text{.....(1)}$$

which is a step function for each interband transition, where e is the electron charge, n_r is the real part of surrounding refractive index, c is the speed of light, ε_o is the vacuum permittivity, m_o is

the free electron mass, $\hbar$ is Planck's constant, m_{en}^* and m_{hn}^* are the effective mass for electrons and holes of the n^{th} conduction and valence sub-bands present from the 2-D density-of-states, and $\left|\hat{e}\cdot\vec{p}_{cv}\right|^2$ is the momentum matrix element describing the electron-photon interaction. Equation (1) arises from Fermi's Golden Rule, with optical perturbation $\left|e\vec{A}\cdot\vec{p}_{cv}/m_o\right|$, where $\vec{A}$ is the vector potential related to the optical electric field as E=jωA.

The reciprocal effective masses $1/m_c$, and $1/m_h$, arise in k·p perturbation theory[30] from a similar perturbation $\left|\hbar\vec{k}\cdot\vec{p}_{cv}/m_o\right|$. The reduced effective mass produced by this repulsion of conduction and valence bands in 2nd order k·p perturbation theory is:
$1/m_{en}^* + 1/m_{hn}^* = 4|p_{cv}/m_o|^2/E_{cv}$, where $E_{cv}=\hbar\omega$ is the interband transition energy.

Thus k·p perturbation theory puts $|p_{cv}|^2$ in the denominator of eq'n. (1), while the optical perturbation puts $|p_{cv}|^2$ in the numerator of Eq'n. (1). Thus the momentum matrix element $|p_{cv}|^2$ cancels. Many of the other terms in Eq'n. (1) cancel as well, leaving behind the dimensionless absorptance $\alpha' L_z=\pi(e^2/4\pi\varepsilon_o\hbar c)/n_r$. Aside from π, and a correction for the surrounding refractive index n_r, the absorptance per 2-D sublevel is $(e^2/4\pi\varepsilon_o\hbar c)$, a group of fundamental constants known as the Fine Structure Constant $(e^2/4\pi\varepsilon_o\hbar c)=\alpha=1/137$.

The prime on the absorption co-efficient α' is meant to distinguish it from the Fine Structure Constant α. Since $\alpha' L_z$ is dimensionless, it is somewhat inevitable that it would be related to α, the dimensionless parameter in opto-electronics and quantum physics. Indeed optical absorption depends on electric charge, and α is actually electric charge squared, (in fundamental units where $\hbar=1$, c=1, $4\pi\varepsilon_o=1$).

The simplified calculation above, is vindicated by Szkopek's detailed calculations[31-32], which multiply the step-function by a Sommerfeld Coulomb correction factor:

$$S(\omega)=\frac{2}{1+\exp\{-2\pi\sqrt{Ry/(\hbar\omega-E_{cv})}\}}$$

where Ry is the electron-hole Rydberg binding energy. This puts a sharp, narrow, double-height spike, right at the step function, whose width is related to the typical millivolt Hydrogenic binding energy. In the experiment, Fig. 3.4, the double-height spikes are washed out, and hardly seen, leaving only small vestigial peaks at each step.

There is an additional correction. The dimensionless absorption steps that we observe ~1.6% are actually smaller than πα=2.3%. This is due to a local optical electric field correction factor, which we call n_c. In a surrounding refractive index n_r, $n_c=n_r$, as clear from Eq'n. (1). When the quantum membrane film is mounted on a substrate of refractive index n, it experiences both the incident electric field, E_o, and the Fresnel reflected electric field $\{(1-n)/(1+n)\}E_o$. Superposing the incident and reflected fields, that local optical electric field at the quantum membrane is weaker by $\{2/(1+n)\}E_o$ which reduces the optical absorption by $\{2/(1+n)\}^2$.and the local field correction factor becomes $n_c=\{(n+1)/2\}^2$ yielding the corrected step absorption A_Q:

$$A_Q \equiv \alpha_n'(\omega) L_z = \frac{\pi\alpha}{n_c} = \pi\alpha\left(\frac{2}{1+n}\right)^2$$

In our case the refractive index of CaF_2 is n=1.43, changing the optical local field correction factor n_c to $\{(1+n)/2\}^2$=1.48 reducing the absorption step height to ~1.58%, in close agreement with our observed step height in Fig. 3.4.

Thus we have shown experimentally and theoretically that light absorption in 2-D semiconductors is independent of specific material parameters, such as bandgap, effective mass and thickness. The simplification of $A=M\cdot A_Q$ holds true over a broad range of photon energy, given that the considerable confinement energy shifts with M.

The measured absorptance values for previously reported III-V and II-VI heterostructure QWs are in the range of 0.6-1.1% per QW for the first step[1-5], slightly smaller than the A_Q value presented in this work. This is expected due to an optical local field correction factor n_c~3.5 appropriate to a quantum well grown and embedded in high-index material, rather than our case of free-standing quantum membrane on a low index substrate. On the other hand, the result here is also consistent with the reported absorptance for graphene[7], A~πα which is for a totally suspended membrane with vacuum on either side.

In summary, light absorption in near-ideal 2-D semiconductors is experimentally examined by using free-standing InAs QMs as a model material system. The absorptance of 2-D InAs is found to be an integer multiple of the quantum absorptance, A_Q, governed only by the fundamental physical constant α. Besides its significance in the basic understanding of electron-photon interactions in quantum confined semiconductors, this result provides a new insight toward the use of 2-D semiconductors for novel photonic and optoelectronic devices. Future work should focus on the experimental studies of the absorptance magnitude of other 2-D material systems.

References:

1. Dingle R, Wiegmann W, Henry, CH (1974) Quantum States of Confined Carriers in Very Thin $Al_xGa_{1-x}As$-GaAs-$Al_xGa_{1-x}As$ Heterostructures. Phys Rev Lett 33: 827-830.
2. Masumoto Y, Matsuura M (1985) Direct experimental observation of two-dimensional shrinkage of the exciton wave function in quantum wells. Phys Rev B 32:4275-4278.
3. Stolz W, Maan JC, Altarelli M, Tapfer L, PLoog K (1987) Absorption spectroscopy on $Ga_{0.47}In_{0.53}As/Al_{0.48}In_{0.52}As$ multi-quantum-well heterostructures. II. Subband structure. Phys Rev B 36:4310-4315.
4. Skolnick MS et al. (1987) InGaAs-lnP multiple quantum wens grown by atmospheric pressure metaiorganic chemical vapor deposition. Appl Phys Lett 51:24-26.
5. Cesar CL et al. (1990) Detailed characterization of HgCdTe/CdTe multiple quantum wells. Appl Phys Lett 56:283-285.
6. Mak K, Lee C, Hone J, Shan J, Heinz T (2010) Atomically Thin MoS_2: A New Direct-Gap Semiconductor. Phys Rev Lett 105:136805.
7. Nair RR et al. (2008) Fine structure constant defines visual transparency of graphene. Science 320:1308.
8. Splendiani A et al. (2010) Emerging photoluminescence in monolayer MoS_2. Nano Lett 10:1271-1275.
9. Najmaei S, Liu Z, Ajayan PM, Lou J (2012) Thermal effects on the characteristic Raman spectrum of molybdenum disulfide (MoS_2) of varying thicknesses. Appl Phys Lett 100:013106.
10. Takei K et al. (2011) Quantum confinement effects in nanoscale-thickness InAs membranes. Nano Lett 11:5008-5012.
11. Radisavljevic B, Radenovic A, Brivio J, Giacometti V, Kis A (2011) Single-layer MoS_2 transistors. Nat Nanotech 6:147-150.
12. Ko H et al. (2010) Ultrathin compound semiconductor on insulator layers for high-performance nanoscale transistors. Nature 468:286-289.
13. Li H et al. (2012) Fabrication of single- and multilayer MoS_2 film-based field-effect transistors for sensing NO at room temperature. Small 8:63-67.
14. Liu H, Ye PD (2012) MoS_2 dual-gate MOSFET with atomic-layer-deposited Al_2O_3 as top-gate dielectric. IEEE Elec. Dev. Lett 33:546-548.
15. Fang H et al. (2012) High-performance single layered WSe_2 p-FETs with chemically doped contacts. Nano Lett 12:3788-3792.
16. Hu P, Wen Z, Wang L, Tan P, Xiao K (2012) Synthesis of few-layer GaSe nanosheets for high performance photodetectors. ACS nano 6:5988-5994.
17. Novoselov KS et al. (2005) Two-dimensional atomic crystals. Proc Natl Acad Sci 102:10451-10453.
18. Cho S, Butch NP, Paglione J, Fuhrer MS (2011) Insulating behavior in ultrathin bismuth selenide field effect transistors. Nano Lett 11:1925-1927.
19. Teweldebrhan D, Goyal V, Balandin AA (2010) Exfoliation and characterization of bismuth telluride atomic quintuples and quasi-two-dimensional crystals. Nano Lett 10:1209-1218.
20. Takei K et al. (2012) Nanoscale InGaSb heterostructure membranes on Si substrates for high hole mobility transistors. Nano Lett 12:2060-2066.
21. Fang H et al. (2011) Strain engineering of epitaxially transferred, ultrathin layers of III-V semiconductor on insulator. Appl Phys Lett 98:012111.

22. Efros AL, Rosen M (2000) The electronic structure of semiconductor nanocrystals. Annu Rev Mater Sci 30:475-521.
23. Mikhailova MP (1996) Handbook Series on Semiconductor Parameters (World Scientific, London), vol.1.
24. Ando T, Fowler B, Stern F (1982) Electronic properties of two-dimensional systems. Rev Mod Phys 54:437-672.
25. Poole RT et al. (1975) Electronegativity as a unifying concept in the determination of fermi energies and photoelectric thresholds. Chem Phys Lett 36: 401-403.
26. See supporting information.
27. The Fermi level was calculated from an estimated bulk electron density of $2\times10^{16}/cm^3$. Noguchi M, Hirakawa K, Ikoma T (1991) Intrinsic electron accumulation layers on reconstructed clean InAs((100) surfaces. Phys Rev Lett 66:2243-2246.
28. Fox M (2001) Optical Properties of Solids (Oxford University Press, New York).
29. Chuang SL (2009) Physics of Photonic Devices (John Wiley & Sons, Inc., Hoboken, New Jersey) 2nd ed.
30. Davies JH (1997) The Physics of Low-Dimensional Semiconductors: An Introduction (Cambridge Univ. Press) 1st edition.
31. Szkopek T (2011) Optical Frequency Conductance, Susceptance and Admittance of Quantum Wells. IEEE J. Quantum Electron. 47:500–509
32. Yoshita M, Kamide K, Suzuura H, Akiyama H (2012) Applicability of continuum absorption in semiconductor quantum wells to absolute absorption-strength standards. Appl. Phys. Lett. 101:032108

Chapter 4 Contact Engineering in Single Layered Chalcogenides

4.1 Introduction

Two dimensional systems from layered structure semiconductors are greatly promising for future electronics for their extremely thin body and exceptional electronic properties. Especially when transistors are scaled below 5 nm gate length, single layered semiconductors would be excellent candidates for the channel material due to their minimum surface roughness, absence of surface dangling bonds and/or defect states, if a channel thickness of at most 1/3 of gate length is present for effective gate control. Among various layered materials, graphene, a single sheet of carbon, has gained world-wide interests and explorations, and achieved numerous successful applications. The unique band dispersion of graphene gives rise to its extremely high carrier mobility, however in the other way, its zero bandgap, limits its potential in serving as MOSFETs channels, where bandgap of at least a few kT is needed. Recent advances in atomically single layered MoS_2, a semiconductor with bandgap of 1.8 eV, shows very encouraging results of using it as a channel material in MOSFETs, in particular for n-type conduction, and opens up a new research trend of studying MoS_2's materials properties and improving its device performances.

In this chapter, the first high mobility monolayer chalcogenide p-FETs with high I_{ON}/I_{OFF} is reported. Then by controllable doping of chalcogenide layered semiconductors at the source/drain (S/D) contacts, low contact resistance can be achieved for both n- and p- FETs with monolayer chalcogenides such as WSe_2, and MoS_2.

4.2 High performance single layered WSe_2 p-FETs with chemically doped contacts*

Exploratory research is needed to develop materials, structures, and device technologies for future sub-5 nm gate length field-effect transistors (FETs). At such small scales, severe short channel effects limit the performance and operation of electronic devices[1]. Theoretical studies have shown that the use of large band gap semiconductors with ultrathin bodies and/or gate-all around structures are essential to minimize the short channel effects at extreme scaling limits[1]. Specifically, for ultrathin body devices, a general guideline dictates a body thickness of < 1/3 of the gate length for effective electrostatic control of the channel by the gate electrode[3]. For sub-5 nm gate lengths, this corresponds to channel materials with only 1-2 atomic layers in thickness. In this regard, single layered semiconductors are excellent candidates for the channel material of future monolayer-FETs (ML-FETs). As compared to materials with diamond/zinc-blende structure, layered semiconductors exhibit advantageous surfaces with minimal roughness, dangling bonds, defect states and native oxides. Among various layered materials, graphene has achieved worldwide interest and numerous interesting applications have been proposed[4,5,6,7]. However, graphene does not have an intrinsic band gap, which severely limits its digital logic applications. Meanwhile, the band gap of graphene nanoribbons shown to date is still too small for ultrashort channel FETs[8]. Recent advances in monolayer and few layered MoS_2, a chalcogenide semiconductor with a large band gap of E_g~1.8 eV, has shown the potential use of layered semiconductors for high performance n-type FETs (n-FETs)[9]. To date, however, high mobility monolayer p-FETs with high I_{ON}/I_{OFF} have not been reported, and more importantly routes for controllable doping of chalcogenide layered semiconductors at the source/drain (S/D) contacts for low parasitic resistances have not been explored. In this report, by developing a surface dopant-profiling technique, we demonstrate the first high hole mobility WSe_2 ML-FETs (body thickness of ~0.7 nm) with degenerately doped contacts. The use of heavily p-doped contacts is essential in lowering the metal contact resistances to WSe_2 by orders of magnitude, and enabling the demonstration of p-FETs with peak effective mobility of ~250 cm^2/Vs, near ideal subthreshold swing (SS) of ~60 mV/decade, and high I_{ON}/I_{OFF} of $>10^6$.

WSe_2 is a layered semiconductor with a bulk indirect bandgap of ~1.2 eV (ref. 10-11). A recent study of bulk WSe_2 FETs revealed an intrinsic hole mobility of up to 500 cm^2/Vs (ref. 12). However, the bulk devices exhibited poor I_{ON}/I_{OFF} ratio of less than 10 at room temperature, along with ambipolar behavior, both of which are highly undesirable for digital logic applications. This is presumably due to the use of a bulk (i.e., thick) body which results in large OFF state leakage currents. Here we applied the well-known mechanical exfoliation method to obtain a single layer of WSe_2 from a bulk crystal (Nanoscience Instruments, Inc) on Si/SiO_2 substrates for ML-FET fabrication and characterization. Fig. 4.1a shows an optical microscope image of a single layer WSe_2 flake (light orange) transferred on top of a Si/SiO_2 (thickness, 270 nm) substrate. This thickness of SiO_2 is optimized to optically visualize the contrast of single layer and few layer WSe_2, similar to the cases of graphene and MoS_2 (ref. 9). Fig. 4.1b depicts the atomic force microscope (AFM) image of a single layered WSe_2 flake, with Fig. 4.1c

* Reproduced with permission from Hui Fang *et al.,* Nano Letters, 12, 3788-3792, 2012. Copyright © [2012] ACS.

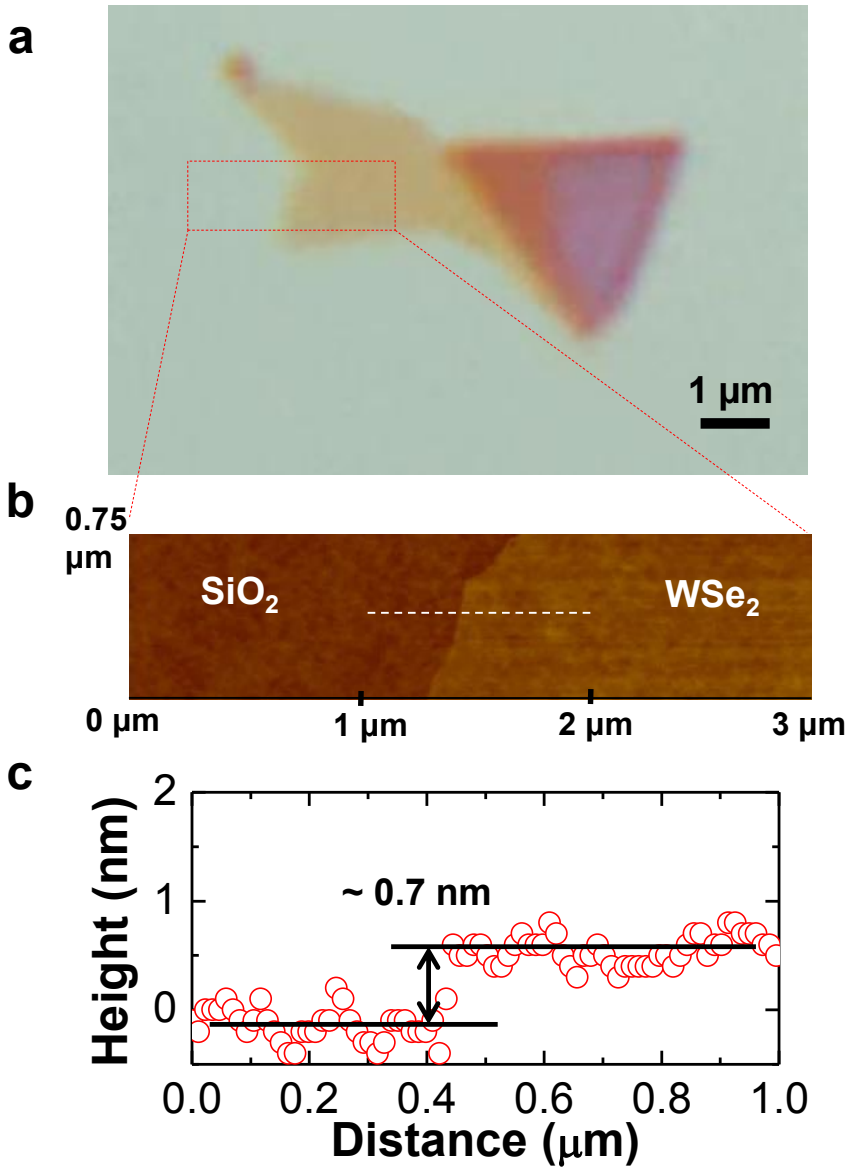

Figure 4.1. Single layered WSe_2 on a Si/SiO_2 substrate. a, Optical microscope image of a single layered WSe_2 (light orange flake) on a Si substrate with 270 nm SiO_2. **b**, AFM image of a single layered WSe_2 on Si/SiO_2. **c**, Height profile of a line scan (as indicated by the dashed line in Fig. 4.1b) across the single layered WSe_2-SiO_2 boundary.

showing the lateral height profile at the edge of the flake. From AFM measurements, the thickness of the single layer is determined to be ~0.7 nm, which agrees with the crystallography data of WSe_2 in literature[13]. Note that the surface roughness of WSe_2 is similar to the Si/SiO_2 background, indicating that the layer is uniform and the surface roughness is minimal, which is essential for obtaining high carrier mobilities with low surface roughness scattering rates.

Large E_g semiconductors such as WSe_2 are notoriously known for their difficulty in forming ohmic metal contacts. Therefore, it is important to shed light on the metal-WSe_2 Schottky barriers (SBs), and explore routes towards minimizing the contact resistances to enable exploration of intrinsic material and device properties. In this regard, we have explored different metal source/drain (S/D) contacts, including Pd, Ag, Ni, Au, Ti and Gd for back-gated WSe_2 FETs. The fabrication process involves the transfer of WSe_2 layers onto a Si/SiO_2 substrate, followed by a 1hr acetone bath to remove the tape residues, S/D metal contact patterning by lithography, evaporation and lift off processes. Here the S/D length is fixed at L~8 μm. Based on the various metal contacts explored, high work function Pd was found to form the lowest resistance contact to the valence band of WSe_2 for hole transport, with devices exhibiting the highest unit-width normalized ON currents. As depicted in the back-gated transfer characteristics (Fig. 4.2a), Pd contacted FETs exhibit clear p-type conduction, without ambipolar transport. In contrast, lower work function metal contacts resulted in FETs that conduct in both n and p regimes with low current levels, reflecting high SB heights to both conduction and valence bands of WSe_2. Specifically, Ti forms near mid-gap SBs to WSe_2 with low-current ambipolar characteristics (Fig. 4.2a-b). The results here highlight the importance of selecting high work function metals with good interfaces to WSe_2 in order to lower the SB height at the contacts for hole transport. Clearly, Fermi level pinning is weak or non-existent at metal-WSe_2 interfaces. Further investigation of the exact effect of the metal work function and interface chemistry on the barrier height is needed in the future.

Although Pd was found to form the best contact for hole transport among the various metals explored, a small SB may still exist at the Pd-WSe_2 interface given the large E_g of WSe_2. To shed light on the contact properties of Pd, surface hole doping of WSe_2 was explored. By heavily p-doping WSe_2, the width of any barriers at the metal interfaces can be drastically reduced, resulting in more efficient tunneling of the carriers and lower resistance contacts. Inspired by the surface doping approach in carbon nanotubes and graphene[14,15,16], here we utilized NO_2 molecules as a p-type surface dopant. NO_2 molecules are expected to be absorbed both physically and chemically on top of the WSe_2 surface as illustrated in Fig. 4.3a. Due to the strong oxidizing property of NO_2, the molecules act as "electron pumps" when chemisorbed to WSe_2. Fig. 4.3b shows the transfer characteristics of a back-gated WSe_2 ML-FET before and after NO_2 exposure. The device was exposed to 0.05% NO_2 in N_2 gas for 10 min, beyond which the doping effect was found to saturate presumably due to the NO_2 saturation coverage on the surface[14]. Here, the entire channel is exposed to NO_2, resulting in blanked (i.e., unpatterned) doping of WSe_2. The weak gate-voltage dependence of current after NO_2 exposure clearly reflects that WSe_2 is heavily doped (Fig. 4.3b). Moreover, the current at high negative V_{GS} (ON state) is enhanced by >1000x after NO_2 doping, which can be attributed to the lowering of contact resistance by thinning the Pd-WSe_2 SB width for hole injection. In addition, NO_2 may increase the work function of Pd, thereby lowering the SB height at the interface. This work function

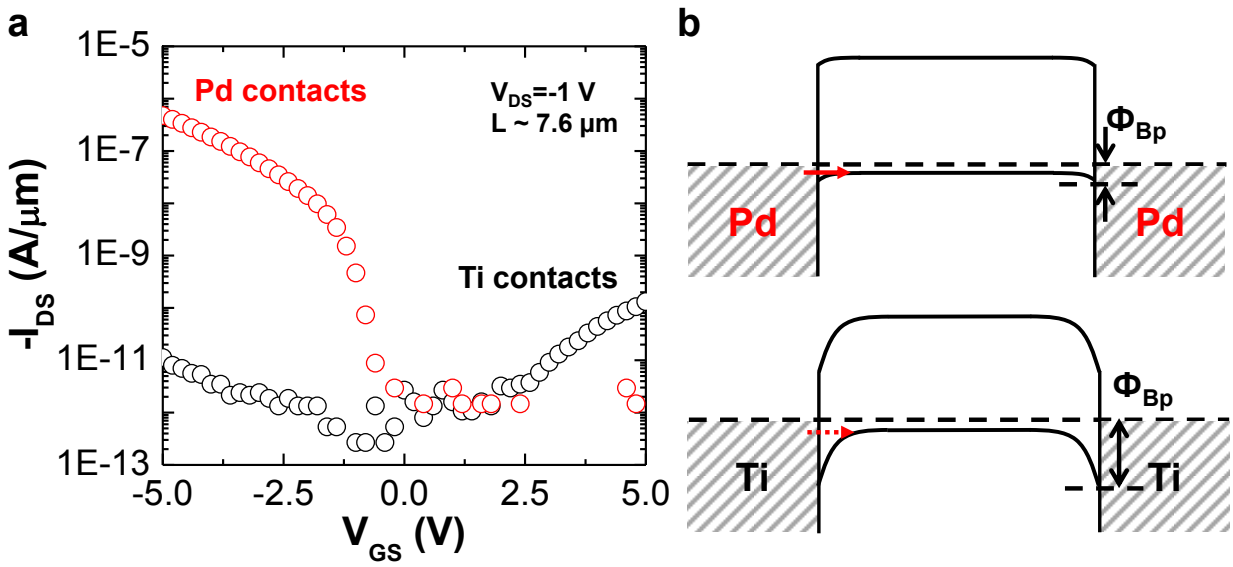

Figure 4.2. Back-gated WSe_2 FETs with different metal contacts. a, I_{DS}-V_{GS} characteristics of Pd (red curve) and Ti (black curve) contacted WSe_2 FETs on a Si substrate with 50 nm SiO_2 as the back-gate dielectric. Here WSe_2 is few layered (thickness, ~5 nm). **b**, Qualitative energy band diagrams for Pd (top) and Ti (bottom) contacted WSe_2 FETs in the ON-state, depicting the height of the SBs for hole injection (Φ_{Bp}) at the metal-WSe_2 interfaces.

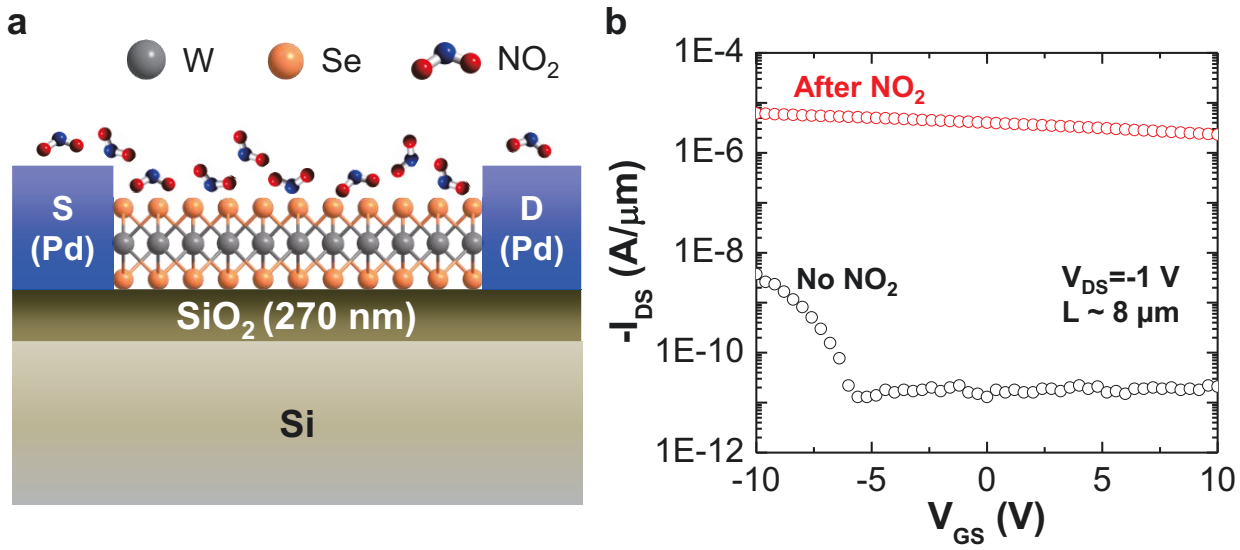

Figure 4.3. Chemical p-doping of single layered WSe_2 by NO_2. a, Cross-sectional schematic of a back-gated WSe_2 ML-FET on Si/SiO_2, with NO_2 molecules being absorbed on both the channel and contacts. **b**, I_{DS}-V_{GS} characteristics of Pd contacted WSe_2 ML-FET before (black curve) and after (red curve) exposure to NO_2.

increase is possibly due to the formation of surface/subsurface metastable palladium oxides when NO_2 is absorbed on Pd as previously reported in literature[17,18].

To estimate the 2-D sheet carrier density (n_{2D}) of WSe_2 after NO_2 doping, the source/drain current (I_{DS}) at zero gate voltage was modeled as $I_{DS} = q \cdot n_{2D} \cdot W \cdot \mu \cdot V_{DS} / L$, where q is the electron charge, W and L are the width and length of channel, respectively, μ is the field-effect mobility (~140 cm^2/Vs as extracted from the I_{DS}-V_{GS} transfer characteristic), and V_{DS} is the source/drain voltage. Since the channel shape is often irregular, the width is defined as the total channel area divided by the length. We note that the field-effect mobility from back-gated WSe_2 ML-FETs doped with NO_2 is 1-2 orders of magnitude higher than MoS_2 ML-FETs without the high-κ dielectric mobility booster[9]. This could be either due to the different surface characteristics of WSe_2 as compared to MoS_2 and/or due to the lower contact resistance observed here by doping the contacts. n_{2D} is extracted to be ~2.2×10^{12} cm^{-2}, which corresponds to a doping concentration of ~3.1×10^{19} cm^{-3}. At this doping concentration, Fermi level lies at ~16 meV below the valence band edge (E_V), as calculated from the Joyce-Dixon Approximation[19] and an effective hole density of state of $N_V=2.54\times10^{19}$ cm^{-3} (ref. 20). Therefore, NO_2 exposed WSe_2 layers are degenerately doped. This doping level, however, is lower than the NO_2 surface monolayer density of ~1.4×10^{15} cm^{-2} (assuming a perfect monolayer coverage)[17], suggesting that on average ~0.001 electron is transferred per NO_2 molecule. It should be noted that NO_2 doping is reversible due to the gradual desorption of NO_2 molecules from the WSe_2 surface once exposed to ambient air (Fig. S1). In the future, other dopant species and/or process schemes should be explored for permanent doping.

Next, we explored patterned p-doping of WSe_2 for the fabrication of top-gated ML-FETs with self-aligned, chemically doped S/D contacts. Pd/Au (30/20 nm) metal contacts were first defined by lithography and metallization. Gate electrodes, underlapping the S/D by a distance of 300 - 500 nm were then patterned by e-beam lithography and using PMMA as resist, followed by atomic layer deposition (ALD, at 120ºC) of 17.5 nm ZrO_2 as the gate dielectric, the deposition of Pd metal gate, and finally lift-off of the entire gate stack in acetone. While it has been reported that direct ALD on pristine graphene is not possible due to the lack of dangling bonds, uniform ALD of Al_2O_3 and HfO_2 on MoS_2 at the optimized temperature window has been previously demonstrated and attributed to the physical absorption of precursors on the basal plane[21,22], which we assume also applies to WSe_2. The devices are then exposed to a NO_2 environment and measured. Fig. 4.4a shows the schematic illustration of a top-gated ML-FET after NO_2 S/D doping. The exposed (underlapped) regions are p-doped heavily, while the gated region remains near intrinsic due to the protection of the active channel by the gate stack. This p+/i/p+ device structure is similar to conventional ultra-thin body Si MOSFETs. Fig. 4.4b shows the transfer characteristics of a ~9.4 μm channel length WSe_2 ML-FET (see Fig. S2 for the device optical images) before and after NO_2 contact doping. Here the back-gate voltage is fixed at -40 V to electrostatically dope the underlapped regions for both before and after NO_2 exposure. As a result, the difference in the current-voltage characteristics for the two measurements purely arises from the change of the metal-WSe_2 contact resistance, rather than the resistance of the underlapped regions. As depicted in Fig. 4.4b, a drastic enhancement of ~1000x improvement in the ON current is observed in the device after surface doping of the contacts by NO_2, without a change in I_{OFF}. A small shift in the threshold voltage to the positive direction is observed after NO_2 contact doping, which could be due to the increase of the Pd metal gate work function by

NO_2. The ML-FET with doped contacts exhibits an impressive I_{ON}/I_{OFF} of $>10^6$ arising from the large band-gap of WSe_2 combined with the monolayer-thick body which minimizes OFF state leakage currents.

Importantly, the transfer characteristics at room temperature shows a perfect subthreshold swing (SS), reaching the theoretical limit of $\ln(10)\times kT/q$ =60 mV/dec for a MOSFET, which originates from the thermionic emission of the source holes with density of states (DOS) tailed by the Fermi-Dirac distribution. For an experimental (i.e., non-ideal) MOSFET, SS is given as η×60 mV/decade, where $\eta \approx 1+\frac{C_{it}}{C_{ox}}$ is the body factor, and C_{it} is the capacitance caused by the interface traps ($C_{it} = D_{it} \cdot q^2$, with D_{it} being the interface trap density) and $C_{ox} = \varepsilon_{ox}\varepsilon_0 / T_{ox}$ is the top gate oxide capacitance per unit area (ε_{ox} ~12.5 is the dielectric constant of ZrO_2, ε_0 is the vacuum permittivity, and T_{ox}= 17.5 nm is the ZrO_2 thickness). The experimental SS~60 mV/decade for WSe_2 ML-FETs suggests the near unity η caused by $C_{it} << C_{ox}$. The low C_{it} is attributed to the lack of surface dangling bonds for layered semiconductors. Notably our measured SS outperforms all Ge and III-V MOSFETs, firmly indicating that WSe_2 has optimal switching characteristics for low power and high speed electronics.

Next the effective hole mobility, μ_{eff}, of top-gated WSe_2 ML-FETs with doped contacts was extracted from the I-V characteristics by using the relation, $\mu_{eff} = \frac{\partial I_{DS}}{\partial V_{DS}} \frac{L_G}{C_{ox}(V_{GS} - V_T - 0.5V_{DS})}$, where V_T is the threshold voltage and L_G is the gate length. The long-channel device exhibits a peak hole effective mobility of ~250 cm^2/Vs (Fig. 4.4c). The mobility does not degrade severely at high fields (Fig. 4.4c), which should be attributed to the fact that the carriers are already close to the gate in a single layered channel, and that surface roughness is minimal. Therefore, the gate oxide thickness can be further scaled without severe mobility degradation, again indicating that WSe_2 is a promising candidate for future scaled electronics. It must be noted that the channel is one monolayer thick (~ 0.7 nm), significantly thinner than the previously reported high hole mobility III-V or Ge MOSFETs, even in ultrathin body (UTB) configuration. For conventional diamond/zinc-blende structured material channels, severe mobility degradation occurs when reducing the channel thickness due to the enhanced scattering from both surface roughness and dangling bonds. For example, the peak effective hole mobility of strained-InGaSb based UTB-FETs drops from ~820 to 480 cm^2/Vs when the body thickness is reduced from 15 nm to 7 nm[23]. Therefore, the measured mobility of 250 cm^2/Vs for our monolayer-thick WSe_2 FETs is impressive.

The output characteristic of the same top gated WSe_2 ML-FET with doped contacts is shown in Fig. 4.4d. The long-channel device exhibits clear current saturation at high V_{DS} due to pinch-off, similar to the conventional MOSFETs. In the low V_{DS} regime, the I-V curves are linear, depicting the ohmic metal contacts. Overall, the results here demonstrate the potential of WSe_2 monolayers along with the essential patterned doping of the contacts for high performance p-FETs.

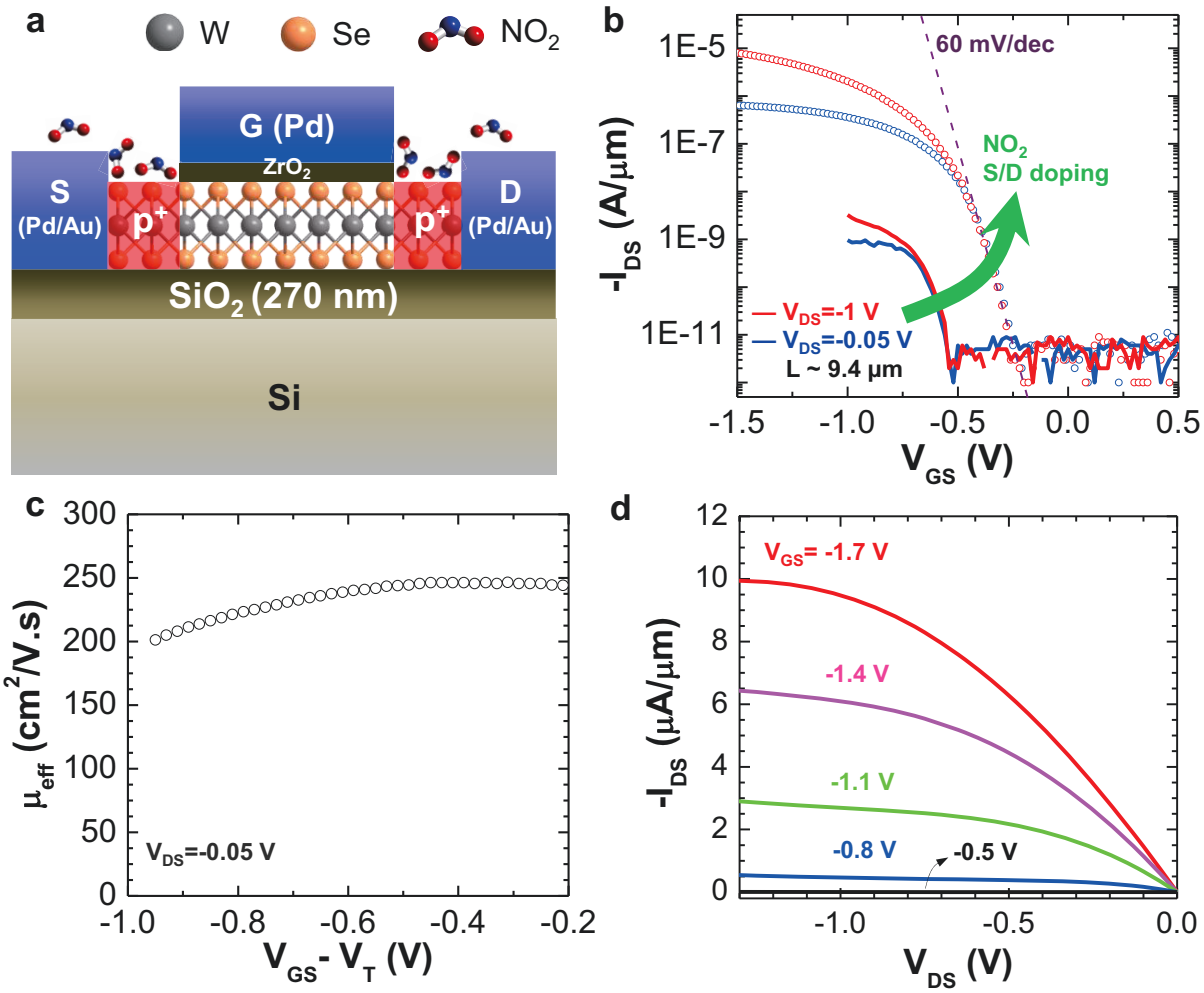

Figure 4.4. Top-gated WSe_2 ML-FETs with chemically doped contacts. a, Schematic of a top-gated WSe_2 ML-FET, with chemically p-doped S/D contacts by NO_2 exposure. Here the top-gate acts as the mask for protecting the active channel from NO_2 doping. **b**, Transfer characteristics of a device with L~9.4 μm, before and after NO_2 patterned doping of the S/D contacts. **c**, Extracted effective hole mobility as a function of gate overdrive of the device shown in b at V_{DS}= -0.05 V. **d**, Output characteristics of the same device shown in b.

In conclusion, the layered semiconductor WSe_2, has been thinned down to a single layer through mechanical exfoliation and fabricated into p-FETs with promising hole mobility and perfect subthreshold characteristics. A NO_2 surface doping strategy is introduced to degenerately dope the S/D regions of the FETs and drastically reduce the metal contact resistance, meanwhile revealing intrinsic transport properties of the channel. Along with the previously demonstrated MoS_2 single layer transistor, the results encourage further investigation of layered semiconductors, especially the transition metal dichalcogenide family, for future high performance electronics. As emphasized in this work, surface doping is a necessity for obtaining high performance ML-FETs, and in this regard exploration of other dopant species for both n- and p-doping in needed in the future.

References:

1. Taur, Y. IBM J. Rev & Dev. **2002**, 46, 213-222.
2. Luisier, M.; Lundstrom, M.; Antoniadis, D. A.; Bokor, J. IEDM Tech. Dig. **2011**, 251-254.
3. Chau, R.; Kavalieros, J.; Doyle, B.; Paulsen, N.; Lionberger, D.; Barlage, D.; Arghavani, R.; Roberds, B.; Doczy, M. IEDM Tech. Dig. **2001**, 621-624.
4. Liu, M.; Yin, X.; Ulin-Avila, E.; Geng, B.; Zentgraf, T.; Ju, L.; Wang, F.; Zhang, X. Nature **2011**, 474, 64-67.
5. Schedin, F.; Geim, a K.; Morozov, S. V.; Hill, E. W.; Blake, P.; Katsnelson, M. I.; Novoselov, K. S. Nat. Mater. **2007**, 6, 652-655.
6. Frank, O.; Tsoukleri, G.; Riaz, I.; Papagelis, K.; Parthenios, J.; Ferrari, A. C.; Geim, A. K.; Novoselov, K. S.; Galiotis, C. Nat. Commun. **2011**, 2, 255.
7. Britnell, L.; Gorbachev, R. V.; Jalil, R.; Belle, B. D.; Schedin, F.; Mishchenko, A.; Georgiou, T.; Katsnelson, M. I.; Eaves, L.; Morozov, S. V.; Peres, N. M. R.; Leist, J.; Geim, A. K.; Novoselov, K. S.; Ponomarenko, L. A. Science **2012**, 335, 947-950.
8. Wang, X.; Ouyang, Y.; Jiao, L.; Wang, H.; Xie, L.; Wu, J.; Guo, J.; Dai, H. Nat. Nanotech. **2011**, 6, 563-567.
9. Radisavljevic, B.; Radenovic, A; Brivio, J.; Giacometti, V.; Kis, A. Nat. Nanotech. **2011**, 6, 147-150.
10. Upadhyayula, L. C.; Lorerski, J. J.; Wold, A.; Giriat, W.; Kershaw, R. J. Appl. Phys. **1968**, 39, 4736-4740.
11. Yousefi, G. H. Mater. Lett. **1989**, 9, 38-40.
12. Podzorov, V.; Gershenson, M. E.; Kloc, C.; Zeis, R.; Bucher, E. Appl. Phys. Lett. **2004**, 84, 3301-3303.
13. Kalikhman, V. L.; Umanskii, Y. S. Sov. Phys. Usp. **1973**, 15, 728-740.
14. Kong, J.; Franklin, N. R.; Zhou, C.; Chapline, M. G.; Peng, S.; Cho, K.; Dai, H. Science **2000**, 287, 622-625.
15. Chen, W.; Chen, S.; Qi, D. C.; Gao, X. Y.; Wee, A. T. S. J. Am. Chem. Soc. **2007**, 129, 10418-10422.
16. Wehling, T. O.; Novoselov, K. S.; Morozov, S. V.; Vdovin, E. E.; Katsnelson, M. I.; Geim, A. K.; Lichtenstein, A. I. Nano Lett. **2008**, 8, 173-177.
17. Bartram, M. E.; Windham, R. G.; Koel, B. E. Surf. Sci. **1987**, 184, 57-74.
18. He, J.-W.; Memmert, U.; Norton, P. R. J. Chem. Phys. **1989**, 90, 5088-5093.
19. Joyce, W. B.; Dixon, R. W. Appl. Phys. Lett. **1977**, 31, 354-356.
20. Spah, R.; Lux-steiner, M.; Obergfell, M.; Ucher, E.; Wagner, S. Appl. Phys. Lett. **1985**, 47, 871-873.
21. Liu, H.; Ye, P. D. IEEE Electron Device Lett. **2012**, 33, 546-548.
22. Liu, H.; Xu, K.; Zhang, X.; Ye, P. D. Appl. Phys. Lett. **2012**, 100, 152115.
23. Takei, K.; Madsen, M.; Fang, H.; Kapadia, R.; Chuang, S.; Kim, H. S.; Liu, C.-H.; Plis, E.; Nah, J.; Krishna, S.; Chueh, Y.-L.; Guo, J.; Javey, A. Nano Lett. **2012**, 12, 2060-2066.

4.3 Degenerate n-doping of few-layer transition metal dichalcogenides by potassium*

The desire for enhanced computation power has been the driving force for the aggressive scaling of electronic devices over the past several decades. However, at the extreme channel length miniaturization, poor gate control impairs the scaling benefits of conventional transistors.[1,2] In this regard, various new classes of materials and device structures have been proposed to continue the scaling trend.[3-10] Recently two dimensional (2-D) Layered Transition Metal Dichalcogenides (TMDCs), e.g., MoS_2 and WSe_2, have gained tremendous interest due to their body thickness scalability down to a monolayer (ML), without surface dangling bonds or native oxides, and with promising carrier transport properties.[8,10] Field-effect transistors (FETs) fabricated from exfoliated TMDC crystals exhibit outstanding device performances such as an ideal subthreshold swing of ~60 mV/dec, I_{ON}/I_{OFF} ratio of 10^8, and high field effect mobility for both electrons and holes.[8-11] Transistors fabricated on 5-nm-thick MoS_2 flakes show no short channel effects down to a channel length of ~100 nm, without aggressive gate oxide scaling.[12] Shortly after the first successful demonstration of MoS_2 monolayer FETs;[8] building blocks of digital circuits such as logic gates, static random access memory devices and ring oscillators have been realized.[13,14]

Controlled doping of few-layer TMDCs, which is of fundamental material and device importance, has not yet been well explored in the community. This is particularly important given that TMDC FETs reported so far are often limited by Schottky barriers (SBs) at the metal/semiconductor interfaces.[10,12,15,16] Therefore electrical properties are hindered by the contact resistances rather than intrinsic material properties. To be able to push TMDC FETs to their performance limits and also reveal their intrinsic electronic transport properties, recently we reported the use of NO_2 molecules as effective p-dopants for monolayer and few-layer WSe_2.[10] In this doping scheme, NO_2 molecules are absorbed on the surface of WSe_2, resulting in surface electron transfer from WSe_2 to NO_2 given the strong oxidizing nature of NO_2 molecules. Building on this concept, here we report the first degenerate n-doping of MoS_2 and WSe_2. Specifically, we use potassium as an efficient surface n-dopant and achieve a high electron sheet density of $\sim 1.0\times10^{13}$ cm^{-2} in MoS_2 and 2.5×10^{12} cm^{-2} for WSe_2. We also for the first time demonstrate few-layer WSe_2 n-FETs with electron mobility of ~110 $cm^2/V.s$ by selectively n-doping the metal contact regions with K.

Electron doping by K vapor has been previously applied to carbon nanotubes and graphene.[17-19] Due to the small electron affinity of K, it is a strong electron donor to most surfaces. Here, to study the doping effects of K on the transport properties of TMDCs, back gated devices made of few-layer MoS_2 and WSe_2 with channel lengths of 0.5-10 μm were first fabricated and systematically studied as a function of doping. The fabrication process starts with the transfer of MoS_2 or WSe_2 layers on a Si/SiO_2 substrate (oxide thickness, t_{ox}=270 nm) using an adhesive tape[8], followed by a acetone wash for 1hr to remove the tape residues. Subsequently source/drain (S/D) metal contacts were formed by lithography, metal evaporation and lift off processes. The contacts were annealed at 200 ºC for 5 min in Ar. The K doping of few-layer

* Reproduced with permission from Hui Fang *et al.,* Nano Letters, 13, 1991-1995, 2013. Copyright © [2013] ACS.

chalcogenides was carried out in a sealed chamber, where the samples/devices were placed ~2-3 cm in distance under the K dispenser (SAES Getters, USA). The chamber was then pumped and maintained at ~3.5×10^{-5} torr by a turbo pump and a current of 5 amperes was applied to the K dispenser to initiate the doping process. The dose was controlled by monitoring the device performance in-situ as a function of exposure time to the K vapor. For MoS_2, Ni and Au metal contacts were found to give good n-type conduction, which is consistent with literature.[12] Here we choose Ni for simplicity. Figure 4.5(a) and (c) show the device schematics of few-layer MoS_2 and WSe_2 back gated FETs blank-doped with K. Figure 4.5(b) shows the transfer characteristics of a 3-monolayer MoS_2 back gated device before and after K doping, measured in vacuum. The as-made device exhibits a typical switching behavior with large I_{ON}/I_{OFF} ($> 10^5$). After doping by exposing the entire channel to K vapor, the current I_{DS} becomes weakly dependent on the gate voltage, which clearly indicates that MoS_2 is heavily n-doped (current at positive bias side still slight higher than negative side). The current level also increases with doping mainly due to two effects: 1) higher tunneling probability through SBs due to barrier thinning by strong doping and, 2) higher channel conductance arising from the higher electron concentration. The first effect results in a lower contact resistance and is a more prominent factor given that for as-made devices, the current nearly saturates at very high gate fields (Fig. 4.5b), suggesting that the current is limited by the injection of carriers from the source contact. For few-layer WSe_2, here we use Au as the contact metal since it results in higher electron conductance (i.e., lower SB height to the conduction band) as compared to the other metal contacts that we explored, including Pd and Ni. Specifically ambipolar device characteristics with both electron (positive V_{GS}) and hole (negative V_{GS}) conduction (Fig. 4.5d) due to the mid-gap SBs are observed for Au contacted WSe_2 FETs. This is in contrast to Pd contacted FETs which exhibit only p-channel conduction due to lower SBs for holes as compared to electrons.[10] After K doping, WSe_2 FETs also exhibit weak gate dependence in I_{DS}, which coincides with the result from MoS_2, indicating a high electron doping level.

To approximate the sheet electron concentration after K doping, here we assume that K doping results in SB width thinning such that the tunneling probability is near unity. Therefore, the contact resistance after doping can be ignored. The 2-D sheet doping concentration ($n_{2\text{-}D}$) is then extracted from $n_{2D} = \frac{I_{DS} \cdot L}{\mathrm{q} \cdot W \cdot V_{DS} \cdot \mu}$, where q is the electron charge, W and L are the width and length of channel, respectively, I_{DS} is the source/drain current at zero gate voltage, V_{DS} is the source/drain voltage, and μ is the field-effect mobility. The mobility was extracted from the I_{DS}-V_{GS} transfer characteristic after doping using parallel plate capacitor model ($C_{ox} = \varepsilon_{ox}\varepsilon_0 / T_{ox}$ is the gate oxide capacitance per unit area, where ε_{ox} ~3.9 is the dielectric constant of SiO_2, ε_0 is the vacuum permittivity, and T_{ox}= 270 nm is the SiO_2 thickness) to estimate the channel charge modulation. We extract an electron concentration $n_{2\text{-}D}$ ~1.0×10^{13} cm^{-2} for K doped MoS_2 and 2.5×10^{12} cm^{-2} for WSe_2. The difference in the extracted electron concentrations could arise from difference in the K surface coverage for the two samples.

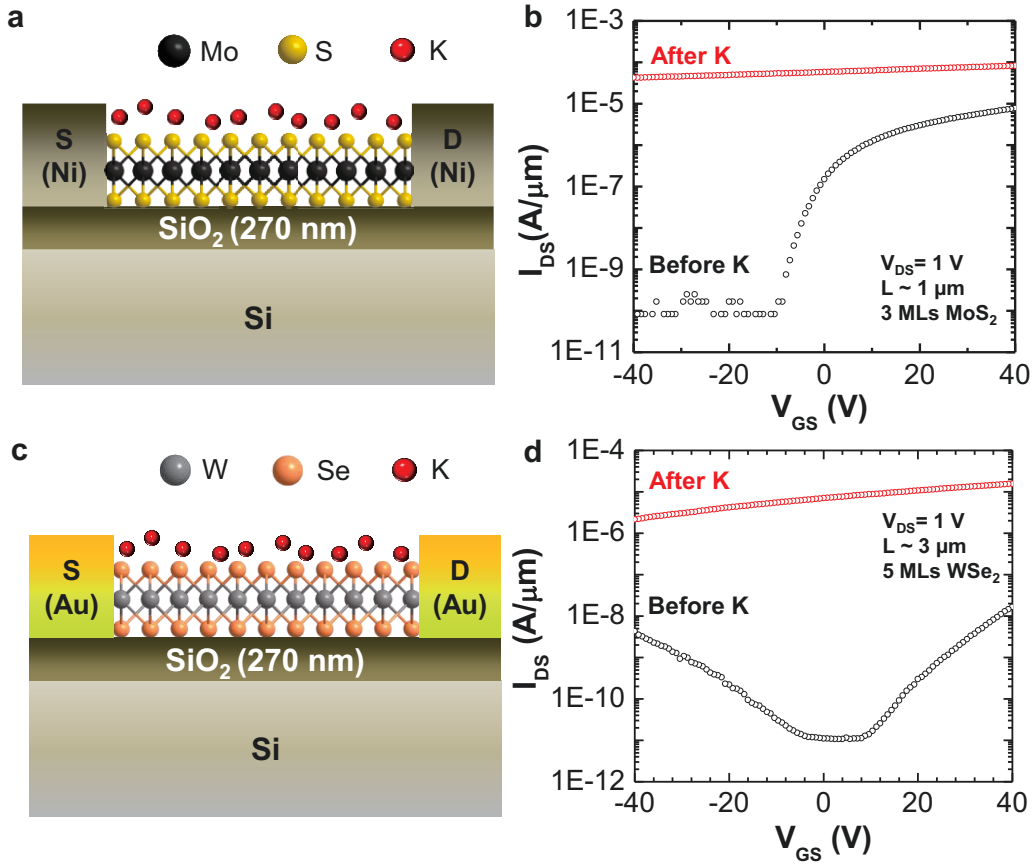

Figure 4.5. "Blanked" (i.e., unpatterned) n-doping of few-layer MoS_2 and WSe_2 by K. (a, c) shows the schematic of K doping of the entire channel for MoS_2 and WSe_2 devices respectively, with (b, d) showing the corresponding transfer characteristics before (black symbols) and after (red symbols) doping.

Patterned n-doping of few-layer TMDCs was explored next by fabrication of top-gated few-ML TMDC FETs with self-aligned, K-doped S/D contacts. Specifically, a 3-ML WSe_2 top-gated FET with L~6.2 μm is shown here as a proof of concept. Au (40 nm) was used as the S/D contacts. ZrO_2/Ni (17.5/30 nm) gate stack (underlapping the S/D metal contacts by a distance of 300 - 500 nm) was formed by electron beam lithography, metal deposition and lift-off. To be able to lift off the gate stack, ZrO_2 was deposited by atomic layer deposition (ALD) at a low temperature of ~120 ºC. Figure 4.6(a) depicts the 3-ML WSe_2 top gated FET after K doping of the exposed S/D. The exposed (underlapped) regions are n-doped heavily, while the gated region remains near intrinsic due to the protection of the active channel by the gate stack. The resulting structure is n+/i/n+, similar to the conventional n-MOSFETs. Figure 4.6(b) shows the transfer characteristics of the device in vacuum with increasing doping time. Here the back-gate voltage is fixed at 40 V to electrostatically dope the underlapped regions. As a result, the difference in the I_{DS}-V_{GS} characteristics mainly arises from the change of the metal-WSe_2 contact resistance, rather than the resistance of the underlapped regions. The device before doping shows a low current of <10 pA/μm at V_{DS} =0.05 V. The electron conduction at the positive gate voltage increases drastically by orders of magnitude after K vapor exposure, which clearly depicts the lowering of the contact resistance. Specifically, the current value after 120 min of doping using the specified condition is ~10^5 × higher than the device with undoped contacts. Note that a small threshold voltage shift towards the more negative voltage is observed with K doping. This is attributed to the diffusion of a small fraction of the K atoms through the top-gate stack, especially given the small size of K ions.

Figure 4.6(c) shows the transfer characteristics of a top-gated WSe_2 FET after 120 min of K doping at both high (V_{DS}= 1 V) and low (V_{DS}= 0.05 V) fields. The device exhibits > 10^4 of I_{ON}/I_{OFF}, and over 110 cm^2/V.s peak effective electron mobility, which was extracted from the I-V characteristics by using the relation $\mu_{eff} = \frac{\partial I_{DS}}{\partial V_{DS}} \frac{L}{C_{ox}(V_{GS} - V_T - 0.5V_{DS})}$. Here, V_T =-0.46 V is the threshold voltage, V_{GS} is the gate bias and $C_{ox} = \varepsilon_{ox}\varepsilon_0 / T_{ox}$ is the top gate oxide capacitance per unit area (ε_{ox}~12.5 is the dielectric constant of ZrO_2, ε_0 is the vacuum permittivity, and T_{ox}= 17.5 nm is the ZrO_2 thickness). The I_{DS}-V_{DS} output characteristic of this device is shown in Figure 4.6(d). The I-V behavior at low V_{DS} region clearly depicts the ohmic contacts, while at high V_{DS} current saturates by pinch-off, similar to the conventional long-channel MOSFETs.

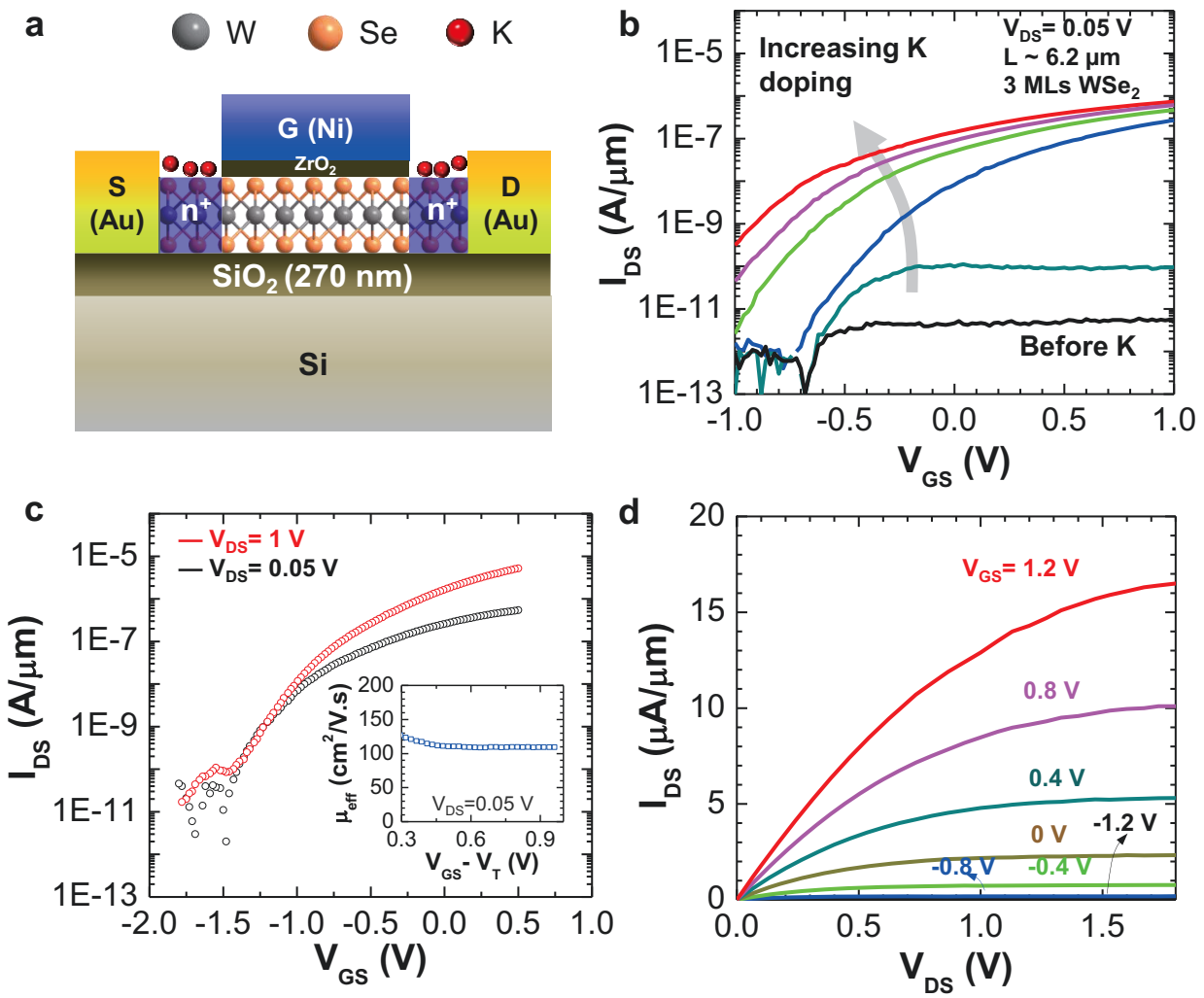

Figure 4.6. Top-gated few-layer WSe_2 n-FETs with chemically doped contacts. (a) Schematic of a top-gated few-layer WSe_2 n-FET, with chemically n-doped S/D contacts by K exposure. (b) Transfer characteristics of a 3-layer WSe_2 device (L~6.2 µm) as a function of K exposure time. The black curve is before doping, while the other curves from bottom to top are after 1, 20, 40, 70, and 120 min doping. (c) Transfer characteristics of the device in b after 120 min doping. Inset shows extracted effective electron mobility as a function of the gate overdrive of the device at V_{DS}= 0.05 V. (d) Output characteristics of the same device shown in b.

A similar top-gate device structure was explored for few-layer MoS_2 (Fig. 4.7a). Figures 4.7(b) and (c) show the I_{DS}-V_{DS} output characteristics of a 3-ML MoS_2 top-gated FET with L ~1 μm at two difference back gate bias V_{BG}, 0 V and 40 V respectively. The I_{DS}-V_{DS} curves reflect a clear Schottky contact behavior at low V_{DS} regime, even with a back-gate voltage of V_{BG}=40 V where the underlapped regions are electrostatically doped by the back gate. After K surface charge transfer doping of the underlapped regions, the current goes up by more than one order of magnitude at the same V_{BG} (0 V) and top gate bias V_{TG}. Moreover, the Schottky behavior disappears and the low-field regime exhibits an ohmic behavior. The peak effective mobility of this device after K doping of the contacts was extracted to be ~25 cm^2/V.s. Note that this mobility values is lower than the highest values previously reported in literature, which may be due to the fact that the top gate dielectric layer was deposited at a low temperature to enable the lift-off process with PMMA resist and the "dielectric boosting" effect[8] was not seen for ZrO_2 deposited at this low temperature.

To shed light on the charge transfer between K and TMDCs, X-ray Photoelectron Spectroscopy (XPS) surface analysis was performed. Figure 4.8(a) and (b) show the Mo 3d and S 2p peaks, before and after sample exposure to K. After K exposure, the Mo 3d and S 2p peaks broaden while the positions of their maxima shift toward higher values. Specifically, Mo $3d_{3/2}$ shifts from 232.0 eV to 232.7 eV, Mo $3d_{5/2}$ shifts from 228.8 eV to 229.5 eV, S $2p_{1/2}$ shifts from 162.7 eV to 163.3 eV, and $2p_{3/2}$ shifts from 161.6 eV to 162.2 eV. The upshift of the peaks is directly attributed to the n-doping process, since it causes a Fermi level shift towards the conduction band edge and the Fermi level is where the zero energy lies. This upshift is also consistent with previous studies of doped graphite and molecular films.[20,21] Similarly, the peaks of W $4f_{5/2}$ and $4f_{7/2}$, as well as Se $3d_{3/2}$ and Se $3d_{5/2}$ upshift (by ~0.4 eV) after K exposure, as depicted in Figures 4.8(c) and (d). The blue shift of the elemental electron binding energy is a direct indication of the surface charge transfer doping.

Ab initio simulations were performed to further understand the charge transfer and doping mechanism. The simulation was conducted by density-functional theory (DFT) with Vienna ab-initio simulation package (VASP) codes[22], and Bader analysis[23-25] was used calculate the charge contribution from the potassium dopant.[26] Figure 4.9(a) and (b) depict the top and side view schematics of K-doped MoS_2 and graphene monolayers, respectively, with one-side covered with K at a density of 1/4 K atom per unit cell (i.e., one K atom per 4 unit cells). Similar to graphene, the K dopant is located above the centers of the hexagons in MoS_2. Despite of S being a larger atom than C, the distance between the K dopant and the S plane in MoS_2 (2.60Å) is shorter than that of K and C plane in graphene (2.89Å). The bond length of K-S is 3.06Å in MoS_2, compared to the K-C bond length of 3.24 Å in graphene. The shorter bond length indicates a stronger binding of K to MoS_2, which is consistent with a larger binding energy in K-doped MoS_2 and more stable doping as shown in Fig. 4.9(c). The simulation results indicate that the bond length decreases and the binding energy increases as the doping density decreases, but the qualitative difference between K-doped MoS_2 and K-doped graphene remains unchanged (Fig. 4.9(c)). We also performed similar simulations of K-WSe_2. The distance between the K dopant and the Se plane is 2.76 Å and the K-Se bond length is 3.36 Å. Because WSe_2 have larger atoms than MoS_2, the bond length is larger and the binding energy is smaller, but the K-WSe_2 binding energy is still larger than that of K-graphene. To examine charge transfer between the K dopant and ML 2-D materials, we performed Bader analysis of charge transfer as shown in Fig. 4.9(d), with a K

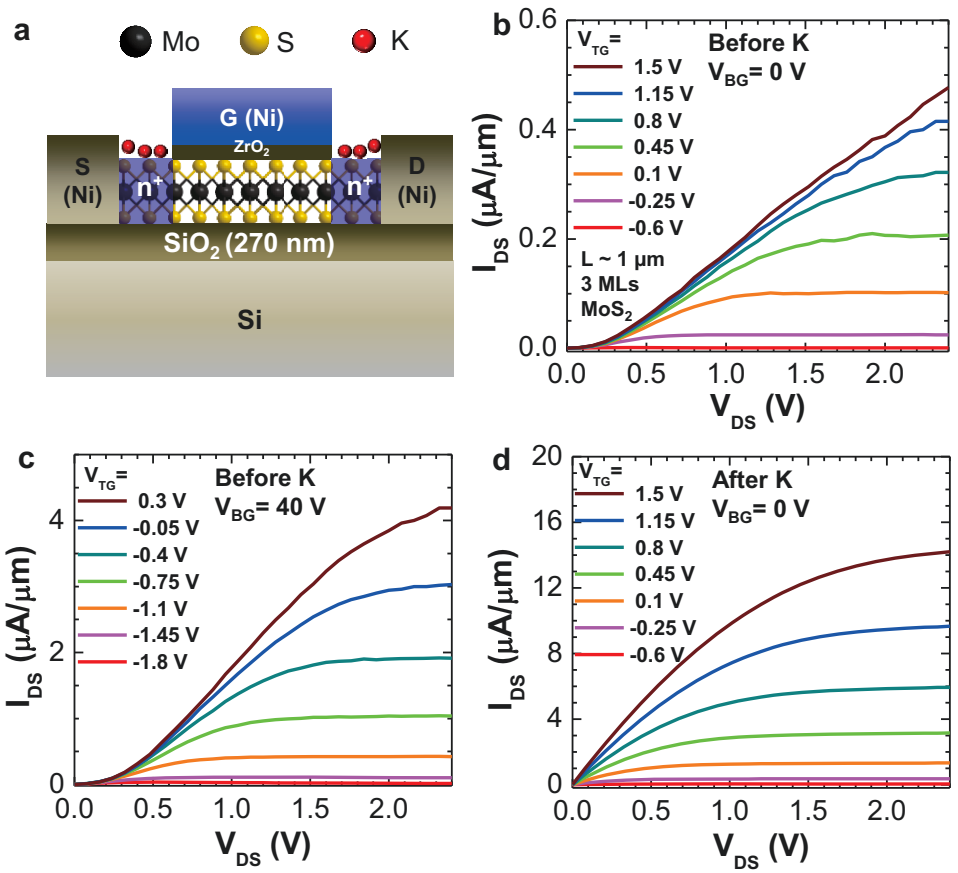

Figure 4.7. Top-gated few-layer MoS_2 n-FETs with chemically doped contacts. (a) Schematic of a top-gated few-layer MoS_2 n-FET, with chemically n-doped S/D contacts by K exposure. (b, c) shows output characteristics of a device (thickness of 3-layers, L~1 μm) before K doping at a back gate voltage of 0 V and 40 V respectively. (d) Output characteristics of the same device shown in (b, c) after 120 min of K doping and with 40 V back gate bias.

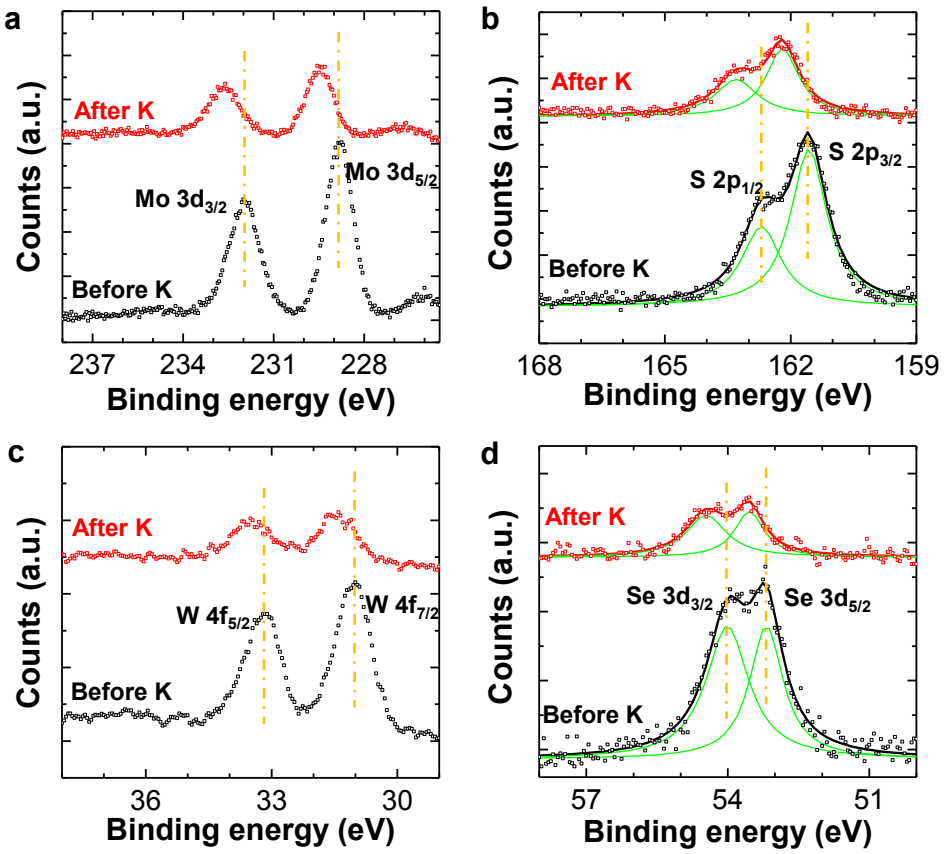

Figure 4.8. XPS surface analysis of MoS_2 and WSe_2 before and after K doping, with binding energy peaks of (a) Mo $3d_{3/2}$ and $3d_{5/2}$, (b) S $2p_{1/2}$ and $2p_{3/2}$, (c) W $4f_{5/2}$ and $4f_{7/2}$ and (d) Se $3d_{3/2}$ and $3d_{5/2}$ electrons. The binding energies at each XPS peak maximum before doping are indicated by the yellow dash lines.

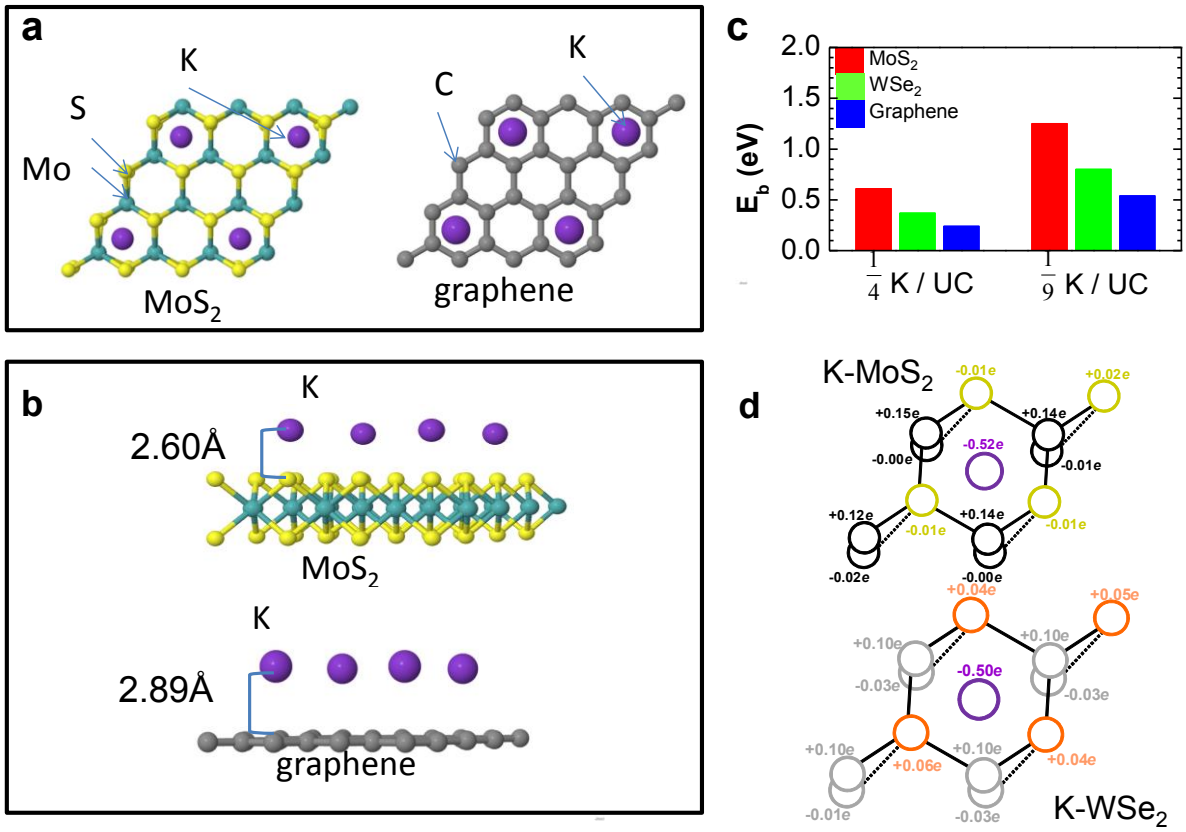

Figure 4.9. Ab initio simulation of MoS_2 and WSe_2 with binding of K atoms, compared to graphene. (a) the top view and (b) side view schematics of the K doped MoS_2 and graphene with a doping coverage of 1/4 K atom per unit cell. The distances between K atoms and S or C planes are denoted. The K-doped WSe_2 has a similar structure to that of MoS_2 but with different bond lengths as explained in the text. (c) Binding energy comparison of K- MoS_2, WSe_2 and graphene, with a dopant coverage of 1/4 and 1/9 K atom per unit cell. (d) The change of elemental valence electron distribution of ML MoS_2 (top) and WSe_2 (bottom) after K doping with a coverage of 1/4 K atom per unit cell comparing to before doping.

concentration of one atom per four MoS_2 unit cells (as one super cell). After placing one K atom in the center of the super cell, there is 0.52e of charge transferred from the K atom to MoS_2, with the top S atoms sharing the charge, while in ML WSe_2, 0.5 of the K charge is transferred, slightly lower than that of K-MoS_2's. The extracted K doping concentration difference between MoS_2 and WSe_2 from the experimental results in Fig 4.5(b) and (d) is ~4 X, larger than the simulation result here. This may be attributed to a number of factors, including difference in the number of K atoms binding to the surfaces for the two materials. Also, it should be noted that the transferred electrons in bonds can be different from the mobile charge carriers due to doping, and the Bader analysis has an uncertainty in determining charge associated with each atom. We also estimated doping density from the simulated density-of-states (DOS) and Fermi energy level. The amount of transferred charge is determined to be 0.55e for K-MoS_2 with a density of 1/4 K per unit cell from the DOS approach, which is consistent with the Bader analysis.

In conclusion, we have studied the surface charge transfer n-doping of few-layer chalcogenides by K. Degenerate doping levels in few-layer MoS_2 and WSe_2 have been achieved and reflected by electrical measurements and surface XPS analysis, and further understood by ab initio calculations. The results here demonstrate the need of degenerate doping of few-layer chalcogenides to improve the contact resistances, and further realize high performance TMDC channel electronics. Specifically, the work shows that n-type WSe_2 FETs can be obtained with high mobilities that complement those obtained for previously reported p-type WSe_2 FETs[10] by simply doping the contacts accordingly. This finding may enable the development of layered semiconductor CMOS devices in the future. While K is used as a model surface charge transfer dopant in this work, in the future, exploration of air-stable dopants is needed.

References:

1. Lundstrom, M. Science (New York, N.Y.) **2003**, 299, 210–211.
2. Taur, Y. IBM J. Rev & Dev. **2002**, 46, 213–222.
3. Choi, Y.; Asano, K.; Lindert, N.; Subramanian, V.; King, T.; Bokor, J.; Hu, C.; Sciences, C. IEDM Tech. Dig. **1999**, 919–921.
4. Huang, X.; Lee, W.-C.; Kuo, C.; Hisamoto, D.; Kedzierski, J.; Anderson, E.; Takeuchi, H.; Asano, K.; Subramanian, V.; Bokor, J. IEDM Tech. Dig. **1999**, 67–70.
5. Heyns, M.; Tsai, W. MRS Bull. **2009**, 34, 485–492.
6. Luisier, M.; Lundstrom, M.; Antoniadis, D. A.; Bokor, J. IEDM Tech. Dig. **2011**, 251–254.
7. Ko, H.; Takei, K.; Kapadia, R.; Chuang, S.; Fang, H.; Leu, P. W.; Ganapathi, K.; Plis, E.; Kim, H. S.; Chen, S.-Y.; Madsen, M.; Ford, A. C.; Chueh, Y.-L.; Krishna, S.; Salahuddin, S.; Javey, A. Nature **2010**, 468, 286–289.
8. Radisavljevic, B.; Radenovic, a; Brivio, J.; Giacometti, V.; Kis, A. Nat. Nanotechnol. **2011**, 6, 147–150.
9. Kim, S.; Konar, A.; Hwang, W-S.; Lee, J. H.; Lee, J.; Yang, J.; Jung, C.; Kim, H.; Yoo, J-B.; Choi, J-Y.; Jin, Y. W.; Lee, S. Y.; Jena, D.; Choi, W.; Kim, K. Nat. Commun. **2012**, 3, 1011.
10. Fang, H.; Chuang, S.; Chang, T. C.; Takei, K.; Takahashi, T.; Javey, A. Nano lett. **2012**, 12, 3788–92.
11. Lembke, D.; Kis, A. ACS nano **2012**, 6, 10070–10075.
12. Liu, H.; Neal, A. T.; Ye, P. D. ACS nano **2012**, 6, 8563–8569.
13. Wang, H.; Yu, L.; Lee, Y.-H.; Shi, Y.; Hsu, A.; Chin, M. L.; Li, L.-J.; Dubey, M.; Kong, J.; Palacios, T. Nano lett. **2012**, 12, 4674–4680.
14. Radisavljevic, B.; Whitwick, M. B.; Kis, A. ACS nano **2011**, 5, 9934–9938.
15. Qiu, H.; Pan, L.; Yao, Z.; Li, J.; Shi, Y.; Wang, X. Appl. Phys. Lett. **2012**, 100, 123104.
16. Kang, J.; Sarkar, D.; Liu, W.; Jena, D.; Banerjee, K. IEDM Tech. Dig. **2012**. ASAP
17. Kong, J.; Zhou, C.; Yenilmez, E.; Dai, H. Appl. Phys. Lett. **2000**, 77, 3977–3979.
18. Javey, A; Tu, R.; Farmer, D. B.; Guo, J.; Gordon, R. G.; Dai, H. Nano Lett. **2005**, 5, 345-348.
19. Ohta, T.; Bostwick, A.; Seyller, T.; Horn, K.; Rotenberg, E. Science (New York, N.Y.) **2006**, 313, 951–954.
20. Caballero, A.; Fernfindez, A.; Soriano, L.; Gonzalez-Elipe, A. Surf. Sci. **1996**, 364, 253–265.
21. Mahns, B.; Roth, F.; Knupfer, M. J. Chem. Phys. **2012**, 136, 134503.
22. Kresse, G.; Furthmuller, J. Phys. Rev. B, **1996**, 54, 16, 11169–11186.
23. Henkelman, G.; Arnaldsson, A.; Jónsson, H. Comp. Mater. Sci. **2006**, 36, 354–360.
24. Sanville, E.; Kenny, S. D.; Smith, R.; Henkelman, G. J. Comp. Chem. **2007**, 28, 899–908.
25. Tang, W.; Sanville, E.; Henkelman, G. J. Phys.: Condens. Matter **2009**, 21, 084204.
26. For the simulation, the double-ζ polarized (DZP) basis set was used employing the generalized gradient approximation (GGA) method. The Perdew-Burke-Ernzerhof (PBE) was used for the exchange-correlation potential. The cutoff energy for the wave-function expansion was set to 500 eV.

Chapter 5 Van der Waals Heterostructures Built from Single Layered Chalcogenides

5.1 Introduction

Since their invention, semiconductor heterostructures have been the fundamental platform for many important applications such as lasers, light-emitting diodes, solar cells, and low-noise, high-electron-mobility transistors. Conventional heterostructures are mainly based on III-V semiconductors with zinc blende structure. Strong chemical bonding exists between atoms at the hetero-interface.

In transition metal dichalcogenides on the other hand, individual layers are held together by weak van der Waals forces. However the bonding between the transition metal and chalcogenide atoms within a layer is strong rendering individual layers mechanically robust and highly immune to the creation of dangling bonds or to surface oxidation. This suggests that, analogously to the traditional III-V semiconductor heterostructures, complex transition metal chalcogenide heterostructures can be designed and built by assembling individual single-layers into functional multilayer structures.

In this chapter, the first experimental study is presented on the electronic interlayer interaction in a heterostructure built from two single-layer semiconductors, combining transmission electron microscopy, x-ray photoelectron microscopy, electron transport studies and optical spectroscopy.

5.2 Strong interlayer coupling in van der Waals heterostructures built from single-layer chalcogenides*

Semiconductor heterostructures are the fundamental platform for many important device applications such as lasers, light-emitting diodes, solar cells and high-electron-mobility transistors. Analogous to traditional heterostructures, layered transition metal dichalcogenide (TMDC) heterostructures can be designed and built by assembling individual single-layers into functional multilayer structures, but in principle with atomically sharp interfaces, no interdiffusion of atoms, digitally controlled layered components and no lattice parameter constraints. Nonetheless, the optoelectronic behavior of this new type of van der Waals (vdW) semiconductor heterostructure is unknown at the single-layer limit. Specifically, it is experimentally unknown whether the optical transitions will be spatially direct or indirect in such hetero-bilayers. Here, we investigate artificial semiconductor heterostructures built from single-layer WSe_2 and MoS_2 building blocks. We observe a large Stokes-like shift of ~100 meV between the photoluminescence peak and the lowest absorption peak that is consistent with a type II band alignment with spatially direct absorption but spatially indirect emission. Notably, the photoluminescence intensity of this spatially indirect transition is strong, suggesting strong interlayer coupling of charge carriers. The coupling at the hetero-interface can be readily tuned by inserting hexagonal BN (h-BN) dielectric layers into the vdW gap. The generic nature of this interlayer coupling consequently provides a new degree of freedom in band engineering and is expected to yield a new family of semiconductor heterostructures having tunable optoelectronic properties with customized composite layers.

Two-dimensional (2D) layered TMDC semiconductors such as MoS_2 and WSe_2 have established themselves as strong contenders for next generation electronics and optoelectronics[1-6] and are promising building blocks for novel semiconductor heterostructures[7-11]. Conventional heterostructures are mainly based on group IV, III-V or II-VI semiconductors with covalent bonding between atoms at the hetero-interface. Due to atomic interdiffusion during growth, the resulting atomic-scale interface roughness and composition variation at the hetero-interface inevitably smear the density of states profile and consequently compromise the performance of these heterostructures especially as the film thicknesses are reduced towards a single atomic layer. In addition, the choice of material components for conventional heterostructures is strongly dictated by lattice mismatch.

In TMDCs on the other hand, individual layers are held together by vdW forces, without surface dangling bonds[12]. Semiconductor heterostructures built from customized individual single layer TMDCs would in principle offer atomically regulated interfaces and sharp band edges. While previous efforts have focused on graphene based heterostructures[8-11, 13-21], we present here the first experimental study on the electronic interlayer interaction in a heterostructure built from two single-layer semiconductors. The hetero-bilayers are characterized by transmission electron microscopy, x-ray photoelectron microscopy, electron transport studies and optical spectroscopy, to elucidate the band alignments, optoelectronic properties and the degree of the electronic layer coupling in this novel material system.

* Reproduced with permission from Hui Fang *et al.,* Proceedings of the National Academy of Sciences (PNAS), in press, 2014. Copyright © 2014 NAS.

The fabrication of WSe_2/MoS_2 hetero-bilayers was realized by transferring individual single-layers on top of each other (see Methods in Supporting Information for details). Figure 5.1A shows an illustration of the hetero-bilayer, and Fig. 5.1B displays the corresponding optical microscope image of a WSe_2/MoS_2 hetero-bilayer on a Si substrate with 260 nm thermally grown SiO_2. Due to the 3.8% lattice mismatch, estimated from the bulk lattice constants[12], as well as the unregulated, but in principle controllable angular alignment (ϕ) between the constituent layers, the heterostructure lattice forms a moiré pattern, clearly visible in the high resolution transmission electron microscopy (HRTEM) image in Fig. 5.1C. The HRTEM image displays the boundary region between single-layer MoS_2 and the WSe_2/MoS_2 hetero-bilayer. While MoS_2 exhibits a simple hexagonal lattice, the heterostructure shows moiré fringes with a spatial envelope periodicity on the order of 4-6× the lattice constants of WSe_2 (or MoS_2). Inspection of the diffraction pattern in Fig. 5.1D along the [001] zone axis reveals that in this particular sample the two hexagonal reciprocal lattices are rotated by ϕ=12.5˚ with respect to each other and there is negligible strain in the two constituent layers (Supporting Information). The alignment of the two lattices can also be examined with a fast Fourier transform of the two zoomed-in TEM images in Fig. 5.1C (Supporting Fig. S3). The absence of strain in the constituent layers of the WSe_2/MoS_2 hetero-bilayer is also confirmed by Raman spectroscopy (Supporting Fig. S4), which show that the in plane vibration modes of both WSe_2 and MoS_2 maintain their corresponding positions before and after transfer.

To shed light on the electronic structure of the WSe_2/MoS_2 heterostack, we performed x-ray photoelectron spectroscopy (XPS). Specifically, we used a photoemission electron microscope (PEEM) with a high spatial resolution of 30 nm to discriminate between photoelectrons emitted from the WSe_2 single-layer, MoS_2 single-layer and the WSe_2/MoS_2 hetero-bilayer, as illustrated in Fig. 5.2A (see Supporting Fig. S5 for details). In addition, by looking at the core-level photoelectrons, we achieved elemental and electronic selectivity that allows us to probe photoelectrons originating from the top layer of the hetero-bilayer and to directly quantify the potential difference between the WSe_2 layer in the hetero-stack with respect to the WSe_2 single-layer reference on the substrate. As shown in Fig. 5.2B, a peak shift of about -220 mV in binding energy (or +220 mV in kinetic energy) is evident in the W 4f core levels of the hetero-bilayer as compared to WSe_2 single layer. The direction of the peak shift is consistent with a negative net charge on the WSe_2 in the WSe_2/MoS_2 hetero-bilayer. On the other hand, a shift of +190 mV is observed in the Mo 3d core levels of the WSe_2/MoS_2 in Fig. 5.2C. Our PEEM results therefore indicate that the WSe_2 layer has a negative net charge, while the MoS_2 layer has a positive net charge as a result of Contact Potential. The hetero-bilayer can essentially be interpreted as being a two-dimensional dipole, an atomically thin parallel plate capacitor with vdW gap with a built-in potential up to 400 mV, originating from the work function difference induced charge transfer between the two constituent single layers. The latter interpretation is also consistent with the p- and n-type character of WSe_2 and MoS_2, respectively (ref. 2, 3).

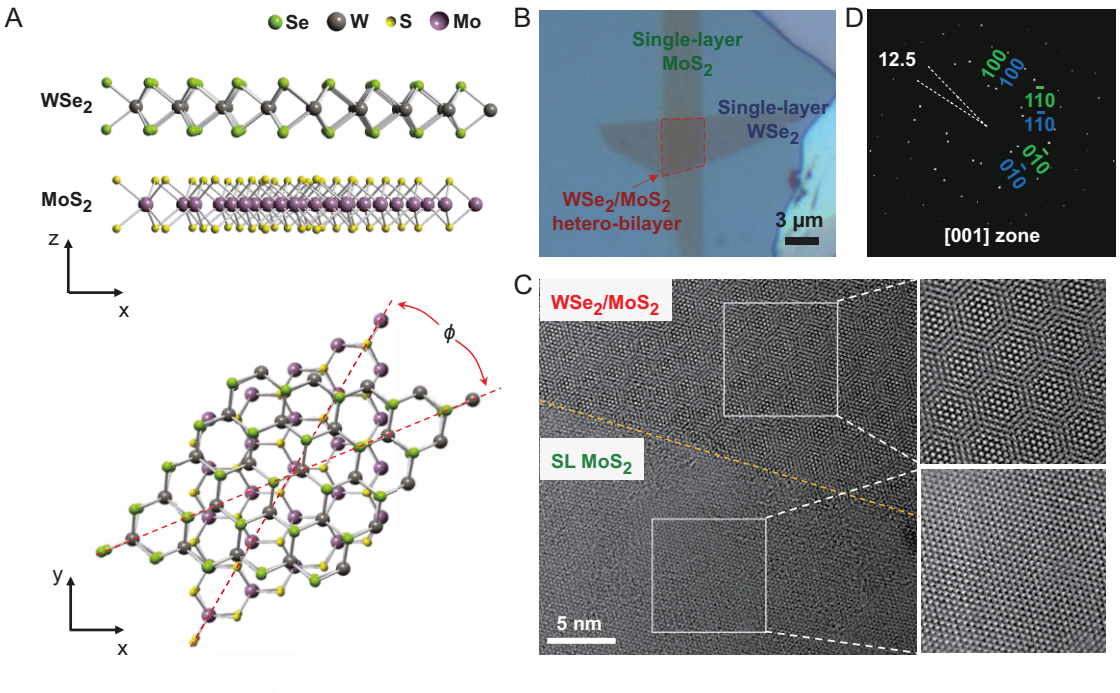

Figure 5.1. WSe_2/MoS_2 hetero-bilayer illustration, optical image, and TEM images. (A) Atomistic illustrations of the heterostructure of single-layer (SL) WSe_2 on single-layer MoS_2 with their respective lattice constants and a misalignment angle ϕ. (B) Optical microscope image of a WSe_2/MoS_2 hetero-bilayer on a Si/SiO_2 (260 nm) substrate. (C) High resolution TEM images of a boundary region of single-layer MoS_2 and the hetero-bilayer, showing the resulting Moiré pattern. (D) The electron diffraction pattern of the hetero-bilayer shown in (C), with the pattern of MoS_2 and WSe_2 indexed in green and blue colors, respectively.

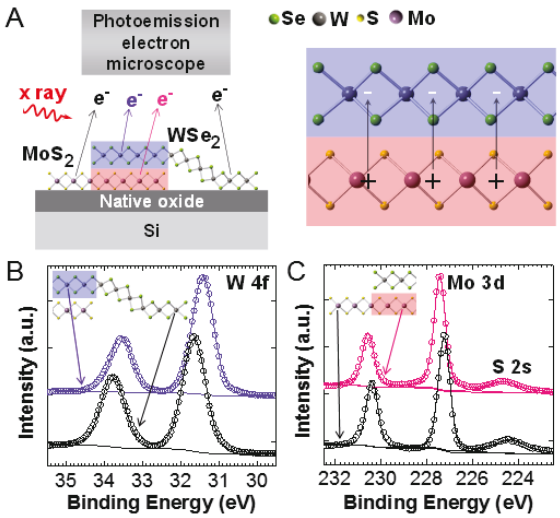

Figure 5.2. XPS core level shift analyses of WSe_2/MoS_2 heterostructures. (A) Sketch of the spatially-resolved photoelectron emission microscopy experiment. (B) Comparison of W 4f core level doublet from WSe_2 and WSe_2/MoS_2 indicating a shift of 220 mV to lower binding energy, corresponding to a negative net charge on the WSe_2 top layer. (C) Comparison of Mo 3d core level doublet and S 2s singlet from MoS_2 and WSe_2/MoS_2 indicating a shift of 190 mV to higher binding energy, corresponding to a positive net charge on MoS_2. The single peak at 224.4-224.6 eV is identified as S 2s, which shows the same shift as Mo 3d, as expected.

To investigate the optoelectronic properties of the WSe_2/MoS_2 hetero-bilayer, we used photoluminescence (PL) and absorption spectroscopy. It is known that both single-layer WSe_2 and MoS_2 exhibit direct band gaps, while their bulk and homo-bilayer counterparts are indirect[1, 22]. In agreement with previous work we observe strong excitonic PL peaks at 1.64 eV and 1.87 eV for single-layer WSe_2 and MoS_2 respectively (Fig. 5.3A). Note that single-layer WSe_2 shows a 10-20× higher PL intensity than single-layer MoS_2, a result consistent with ref. 23. For the WSe_2/MoS_2 hetero-bilayer, we observe a peak at 1.55 eV, lying interestingly at a lower energy than for the two constituent single layers, as shown in Fig. 5.3A, with intensity ~1.5× higher than for single-layer MoS_2. The appearance of a peak at such low energy was observed consistently for multiple (> 10) samples, with peak energies ranging from 1.50 to 1.56 eV (Supporting Fig. S6). This distribution is attributed to sample-to-sample variations in interface quality and/or alignment angle ϕ. Of value in optoelectronics, a tail inverse slope, corresponding to the band-edge sharpness of ~30 meV/dec is extracted from the PL spectra[24, 25] (Supporting Fig. S7). The steep tail slopes of our hetero-bilayer proves that high-quality heterostructures with sharp band edges can be built at the single-layer limit using TMDC building blocks which is a unique feature of this material system.

The nature of the photoluminescence of the WSe_2/MoS_2 hetero-bilayer is intriguing. To better understand the electronic structure of the hetero-bilayer, we performed absorption measurements in the near-infrared and visible part of the spectrum using synchrotron light shown as dashed lines in Fig. 5.3B. The WSe_2/MoS_2 hetero-bilayer shows a first absorption peak at 1.65 eV and a second peak at 1.91 eV. These peaks closely coincide with the absorption peaks of single-layer WSe_2 and MoS_2, respectively. Interestingly, comparing the absorption spectra with the normalized PL data shown in Fig. 5.3B, we note that the hetero-bilayer exhibits a striking ~100 meV shift between the PL and absorbance peaks. This large Stokes-like shift is indicative of a spatially indirect transition in a staggered gap (type II) heterostructure[26]. From this shift, a conduction band offset of ~100 meV between the two monolayer components is extracted (Fig. 5.3C). Our hetero-bilayers share certain similarities with organic semiconductor heterostructures in which donors and acceptors are also bound by weak intermolecular vdW forces[27]. Similar to the optical processes in organic heterostructures, photons are absorbed in single layer WSe_2 and single layer MoS_2, generating excitons in both layers. Photo-excited excitons then undergo dissociation and charge separation at the MoS_2/WSe_2 interface driven by the band-offset as shown in Fig. 5.3C. As a result, holes accumulate in the valence band of WSe_2 and electrons in the conduction band of MoS_2, which is also consistent with the measured built-in electric field from PEEM. Radiative recombination of the spatially separated carriers consequently leads to luminescence. Due to the energy lost by the photo-excited carriers by the band offset (Fig. 5.3C), the PL peak energy is lower than the excitonic band gaps of either material component, leading to the observed Stokes-like shift. Note that in the hetero-bilayer, we observe only a weak luminescence signal at the energies corresponding to the excitonic band gaps of single layer MoS_2 and WSe_2, suggesting that the large majority of the photo-excited carriers are spatially separated by the interface with the luminescence yield being the highest for the spatially indirect recombination process.

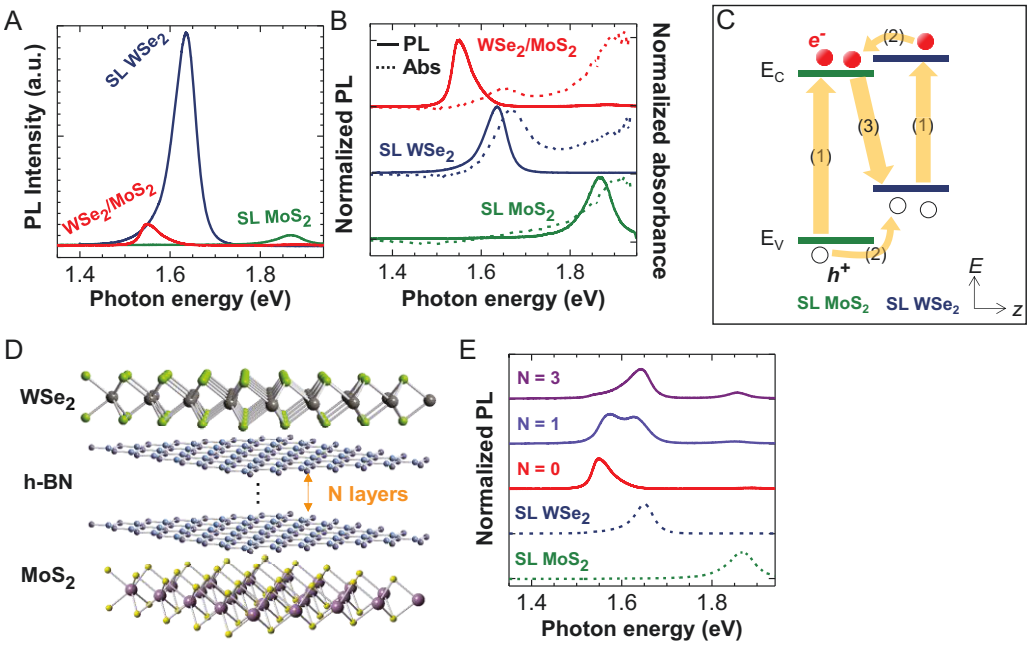

Figure 5.3. Photoluminescence and absorption from WSe_2/MoS_2 hetero-bilayers. (A) PL spectra of single-layer WSe_2, MoS_2, and the corresponding hetero-bilayer. (B) Normalized PL (solid lines) and absorbance (dashed lines) spectra of single-layer WSe_2, MoS_2, and the corresponding hetero-bilayer, where the spectra are normalized to the height of the strongest PL/absorbance peak. (C) band diagram of WSe_2/MoS_2 hetero-bilayer under laser excitation, depicting (1) photon absorption and exciton generation in WSe_2 and MoS_2 single layers, (2) Dissociation of photo-excited excitons and charge separation at the MoS_2/WSe_2 interface driven by the band-offset, resulting in holes accumulating in the valence band of WSe_2 and electrons in the conduction band of MoS_2, (3) Radiative recombination of the spatially separated carriers. E_C and E_V represent the conduction and valence band edges, respectively. (D) An atomistic illustration of the heterostructure of single-layer WSe_2/single-layer MoS_2 with few-layer h-BN spacer in the vdW gap. (E) Normalized PL spectra from single-layer WSe_2/single-layer MoS_2 heterostructure with N layers of h-BN (N=0, 1 and 3).

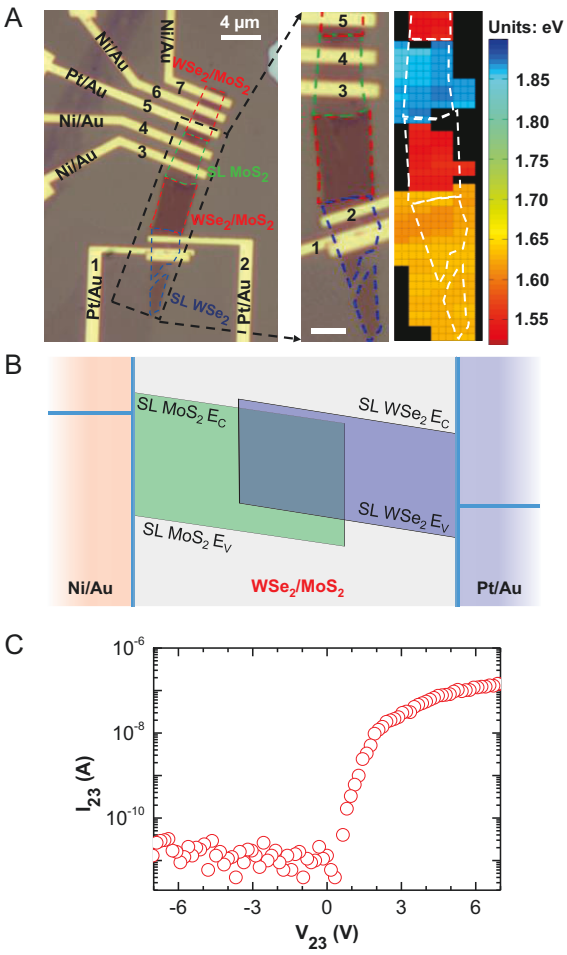

Figure 5.4. Electrical transport across the WSe_2/MoS_2 hetero-interface. (A) Optical microscope image of a device with connected regions of single-layer WSe_2, WSe_2/MoS_2 hetero-bilayer, and single-layer MoS_2 on a Si/SiO_2 substrate. Electrodes are numbered 1-7 from bottom to top. A zoomed-in part of the device was shown along with the corresponding PL peak energy map. The scale bar is 2 μm. (B) a qualitative band diagram of the single-layer WSe_2/hetero-bilayer/single-layer MoS_2 device, corresponding to the device between electrodes 2 and 3 in (A). (C) I-V characteristic when measuring between electrodes 2 and 3, with 2 grounded, 3 biased. A back gate voltage of 50 V was applied to reduce the contact/parasitic resistances to MoS_2 while patterned NO_2 doping was used near the WSe_2 contact for reducing the contact/parasitic resistances of WSe_2 (see SI for details).

To fine tune the interlayer interaction in the WSe_2/MoS_2 hetero-bilayer, single- and few-layer sheets of h-BN were inserted into the vdW gap (Fig. 5.3D) using the same transfer technique. Figure 5.3E shows the normalized PL of hetero-stacks with single- and tri-layer h-BN spacers. Interlayer coupling (i.e., spatial charge separation of the photo-generated carriers and subsequent spatial indirect recombination) becomes negligible for the sample with a tri-layer h-BN spacer, as indicated by both the position and the intensity of the peak at 1.64 eV (Fig. 5.3E and Supporting Fig. S8), which are nearly the same as single-layer WSe_2. On the other hand, a single layer of h-BN does not fully suppress the interlayer interaction between WSe_2 and MoS_2. The results demonstrate that the interlayer coupling can be readily tuned by intercalation of layered dielectric media, and provides yet another degree of control in the vdW heterostructure properties.

Finally, we explored the carrier transport along the hetero-bilayer interface. A single flake consisting of different regions corresponding to single-layer WSe_2 and MoS_2, and hetero-bilayer was made via the transfer process. The flake was dry etched into a long ribbon (Fig. 5.4A). A corresponding PL peak energy map is shown in Fig. 5.4A, further depicting the lateral structure of the ribbon used in this study. Multiple source/drain (S/D) metal electrodes were then fabricated by electron beam lithography and lift-off on each region of the ribbon (see Supporting Information for details). The Si/SiO_2 (260 nm in thickness) substrate serves as the global back gate. As expected single-layer MoS_2 and WSe_2 devices exhibit n- and p-type characteristics, respectively (Supporting Fig. S9), which is consistent with previous reports[2, 3]. On the other hand, the device consisting of one contact on single-layer WSe_2 and the other on single-layer MoS_2, with the two layers overlapping in the central region (Fig. 5.4B) exhibits a distinct rectifying behavior, consistent with type II band-alignment of the heterobilayer (Fig. 5.4C). The transport data provides additional direct evidence on the electrical coupling and the Contact Potential between the two constituent layers. Furthermore, the work highlights the ability to engineer a novel class of electronic and optoelectronic devices by vdW stacking of the desired layered chalcogenide components with molecular-scale control in thickness.

In summary, we have fabricated and characterized an artificial vdW heterostructure by stacking single-layer transition metal dichalcogenide building blocks and achieved strong interlayer coupling between the two 2D semiconductor constituents. Strong PL with a large Stokes-like shift was observed from the WSe_2/MoS_2 hetero-bilayer, consistent with spatially indirect luminescence from a type II heterostructure. We anticipate that our result will trigger subsequent studies focused on the bottom-up creation of new heterostructures by varying chemical composition, interlayer spacing and angular alignment. In addition the focus will be on the fabrication of vdW semiconductor heterostructure devices with tuned optoelectronic properties from customized single layer components

References:

1. Mak KF, Lee C, Hone J, Shan J, & Heinz TF (2010) Atomically Thin MoS_2: A New Direct-Gap Semiconductor. Phys Rev Lett 105(13):136805.
2. Radisavljevic B, Radenovic A, Brivio J, Giacometti V, & Kis A (2011) Single-layer MoS_2 transistors. Nat Nanotechnol 6(3):147-150.
3. Fang H, et al. (2012) High-Performance Single Layered WSe_2 p-FETs with Chemically Doped Contacts. Nano Lett 12(7):3788-3792.
4. Wang H, et al. (2012) Integrated circuits based on bilayer MoS_2 transistors. Nano Lett. 12(9):4674-4680.
5. Zeng H, Dai J, Yao W, Xiao D, & Cui X (2012) Valley polarization in MoS_2 monolayers by optical pumping. Nat Nanotechnol 7(8):490-493.
6. Jones AM, et al. (2013) Optical Generation of Excitonic Valley Coherence in Monolayer WSe_2. Nat Nanotechnol 8:634-638.
7. Geim A & Grigorieva I (2013) Van der Waals heterostructures. Nature 499(7459):419-425.
8. Yu WJ, et al. (2012) Vertically stacked multi-heterostructures of layered materials for logic transistors and complementary inverters. Nat Mater 12(3):246-252.
9. Georgiou T, et al. (2012) Vertical field-effect transistor based on graphene-WS_2 heterostructures for flexible and transparent electronics. Nat Nanotechnol 8(2):100-103.
10. Yu WJ, et al. (2013) Highly efficient gate-tunable photocurrent generation in vertical heterostructures of layered materials. Nat Nanotechnol 8(12):952-958.
11. Britnell L, et al. (2013) Strong light-matter interactions in heterostructures of atomically thin films. Science 340(6138):1311-1314.
12. Wilson J & Yoffe A (1969) The transition metal dichalcogenides discussion and interpretation of the observed optical, electrical and structural properties. Adv Phys 18(73):193-335.
13. Dean C, et al. (2010) Boron nitride substrates for high-quality graphene electronics. Nat Nanotechnol 5(10):722-726.
14. Ponomarenko L, et al. (2011) Tunable metal-insulator transition in double-layer graphene heterostructures. Nat Phys 7(12):958-961.
15. Haigh S, et al. (2012) Cross-sectional imaging of individual layers and buried interfaces of graphene-based heterostructures and superlattices. Nat Mater 11:764-767.
16. Britnell L, et al. (2012) Field-effect tunneling transistor based on vertical graphene heterostructures. Science 335(6071):947-950.
17. Gorbachev R, et al. (2012) Strong Coulomb drag and broken symmetry in double-layer graphene. Nat Phys 8:896-901.
18. Hunt B, et al. (2013) Massive Dirac fermions and Hofstadter butterfly in a van der Waals heterostructure. Science 340(6139):1427-1430.
19. Ponomarenko L, et al. (2013) Cloning of Dirac fermions in graphene superlattices. Nature 497(7451):594-597.
20. Dean C, et al. (2013) Hofstadter's butterfly and the fractal quantum Hall effect in moire superlattices. Nature 497(7451):598-602.
21. Yankowitz M, et al. (2012) Emergence of superlattice Dirac points in graphene on hexagonal boron nitride. Nat Phys 8(5):382-386.
22. Zeng H, et al. (2013) Optical signature of symmetry variations and spin-valley coupling in atomically thin tungsten dichalcogenides. Sci Rep 3:1608.
23. Zhao W, et al. (2012) Evolution of electronic structure in atomically thin sheets of WS_2 and WSe_2. ACS nano 7(1):791-797.
24. Van Roosbroeck W & Shockley W (1954) Photon-radiative recombination of electrons and holes in germanium. Phys Rev 94(6):1558.

25. Kost A, Lee H, Zou Y, Dapkus P, & Garmire E (1989) Band-edge absorption coefficients from photoluminescence in semiconductor multiple quantum wells. Appl Phys Lett 54(14):1356-1358.
26. Wilson BA (1988) Carrier dynamics and recombination mechanisms in staggered-alignment heterostructures. IEEE J Quant 24(8):1763-1777.
27. Li G, Zhu R, & Yang Y (2012) Polymer solar cells. Nat Photon 6(3):153-161.

5.3 Experimental and theoretical details*

5.3.1 Methods

Sample preparation:

Fabrication of the heterostructure started with the transfer of MoS_2, WSe_2 and h-BN single and few layers on separate Si/SiO_2 substrates (oxide thickness, t_{ox}=260 nm) using adhesive tapes by the mechanical exfoliation method (1). For h-BN, a 550 nm band pass filter (FWHM=40 nm) was used to further enhance the optical contrast for locating single- to few-layer flakes on Si/SiO_2. These mechanically exfoliated flakes were then annealed at 250 ˚C for 3 hr in a H_2 environment (3.3 torr, 200 sccm) to remove any surface organic residues. The heterostructures were realized by a dry transfer technique (2, 3) with a PMMA membrane as the transfer media. For the heterostructures with single- or few-layer h-BN, single-layer WSe_2 was first transferred onto h-BN, and then these two layers together were picked up by PMMA and transferred onto single-layer MoS_2.

Samples for TEM were prepared on Au TEM grids with holey carbon nets of 1.2 μm diameter orthogonal hole arrays (Ted Pella, Inc.). To remove the PMMA after transfer, the grids with the heterostructure/PMMA were immersed into dichloromethane (DCM) for 6 sec, taken out to allow to air dry for 3 min in fume hoods, and then annealed in H_2 with the same condition noted previously. The short time of immersion is to prevent the samples escaping from the carbon net, while no blow dry was involved to keep the mechanical integrity of the relatively fragile carbon net. Samples for PEEM were prepared on natively oxidized p+ Si substrate. A similar cleaning process was used to remove PMMA and its residue as described above.

TEM condition:

The HRTEM image displayed in Figure 5.1c was acquired on a FEI Titan microscope equipped with a field emission gun operating at accelerating voltage of 300 kV. The images were recorded on a 2048x2048 Gatan Ultrascan CCD camera using DigitalMicrograph software. The microscope was operated in low-dose mode to minimize electron beam-induced degradation as well as contamination of the sample. A Wiener-type filter was applied to the images to reduce the signal arising from the amorphous background. The electron diffraction pattern shown in Figure 5.1d was acquired on a Zeiss Libra 200MC equipped with a monochromator and omega-type in-column energy filter using a 2048x2048 Gatan Ultrascan CCD camera. The microscope was operated at 200 kV accelerating voltage in parallel illumination mode with a semi-convergence angle of 40 μrad. The illuminated area was limited to 0.13 μm^2 using a condenser aperture with a diameter of 37 μm. Energy-filtered diffraction patterns were acquired and analyzed quantitatively using the dedicated software DigitalMicrograph.

PEEM experiments:

The photoemission electron microscopy (PEEM) experiment was conducted at the soft x-ray undulator beamline UE49-PGM-a of the BESSY-II storage ring in Berlin, Germany using

elliptically polarized light at photon energies of 700 eV and 150 eV. The endstation was equipped with an Elmitec PEEM-II energy microscope/analyzer allowing energy and spatially resolved imaging. Depending on the measured sample area, fields of view between 10 and 70 μm were used resulting in a spatial resolution better than 30 and 120 nm, respectively. The total energy resolution of our measurements was 100 meV.

Optical measurements:

PL and Raman measurements were performed at room temperature under ambient conditions. The samples were excited with a continuous wave (cw), blue laser (473 nm) with a spot size of ~ 1 μm, unless mentioned otherwise. The original laser power was 5 mW and neutral density filters were used with optical densities of 3 and 4 (corresponding to 5 and 0.5 μW laser power on the sample). Near-IR/visible absorption measurements were performed at Beamline 1.4.3 at the Advanced Light Source using a Nicolet Magna 760 FTIR interferometer and a Nicolet Nic-Plan infrared microscope. In order to access the visible region, all measurements used a quartz beamsplitter and a silicon detector (Thorlabs, Inc.). The use of synchrotron radiation enabled a spot size of <2 μm.

Details of the hetero-bilayer device fabrication:

Following the fabrication of the WSe_2/MoS_2 hetero-bilayer, a single flake was dry etched into a long ribbon with different regions corresponding to single layer WSe_2, MoS_2, and hetero-bilayer. Pt/Au and Ni/Au metal contacts were then placed on single layer WSe_2 and single layer MoS_2 regions respectively. A ZrO_2 layer was deposited onto single layer MoS_2 region and partial hetero-bilayer region in the ribbon. The device was finally measured with NO_2 doping on the exposed WSe_2 region to minimize contact resistance at the Pt/WSe_2 contact, as shown in Fig. S1. Note that without NO_2 doping, the device still exhibits rectifying behavior with ~10x lower forward bias current density arising from the extra parasitic resistances (Fig. S2). The step-by-step fabrication process is as followed.

1. E-beam lithography was used to define etched regions in the hetero-bilayer flake. Briefly, samples were coated with PMMA (4% in chlorobenzene), baked at 180 ˚C for 5 min, and then exposed using an electron-beam lithography system.
2. The hetero-bilayer flakes were then patterned dry etched using XeF_2/N_2 gas (XeF_2 3 torr, N_2 1.5 torr). For 8 cycles of 30 seconds etching, the etch rate of chalcogenides is over 10 nm/min.
3. The PMMA mask was removed by a dichloromethane (DCM) wash for 10 min and the samples were then annealed in H_2 (3.3 torr, 200 sccm) for 3 hours to remove the PMMA residue.
4. Ni/Au (10 nm/30 nm) contacts were deposited on single layer MoS_2 region by an e-beam lithography, metal deposition and lift-off process. Ni/Au was chosen to contact MoS_2 as it is known to enable efficient injection of electrons (4, 5). A short Ni/Au "anchor" bar (~5 μm length) was also deposited at the end of WSe_2 side to prevent the flake detaching from the substrate during the lift-off process.
5. Pt/Au (10 nm/30 nm) contacts were deposited on single layer WSe_2 region by a similar e-beam lithography, metal deposition and lift-off process. Pt/Au was found to give better p-

type conduction in single layer WSe_2 than Pd, which was the best contact to the valence band of WSe_2 (ref. 6).

6. A ZrO_2 layer (20 nm) was then deposited onto single layer MoS_2 region and partial hetero-bilayer region in the ribbon as a NO_2 blocker by an e-beam lithography, atomic layer deposition and lift-off process.
7. The fully fabricated device was then exposed to 0.05% NO_2 in N_2 gas for 10 min and measured, as shown in Fig. S1. For the I-V characteristic shown in Fig. 5.4C in the main text, a back gate voltage of 50 V was applied to lower the parasitic resistance from MoS_2 while the parasitic WSe_2 was still degenerately p-doped (6).

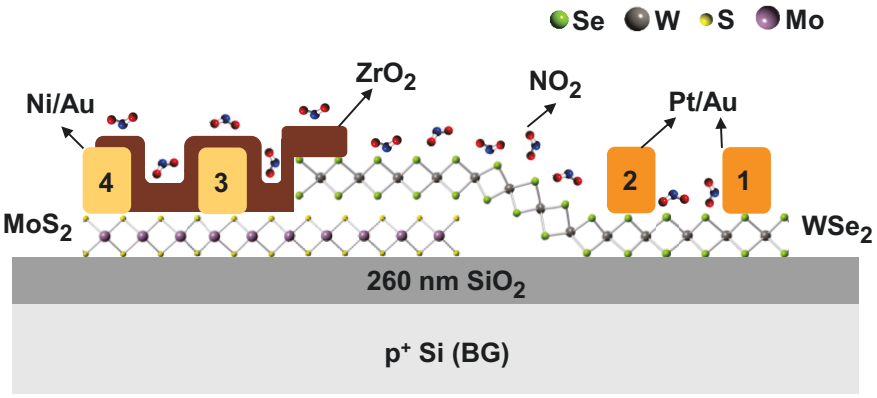

Figure S1. Schematic of fully fabricated WSe_2/MoS_2 hetero-bilayer device. NO_2 doping of exposed WSe_2 region was utilized to reduce the contact/parasitic resistances of WSe_2.

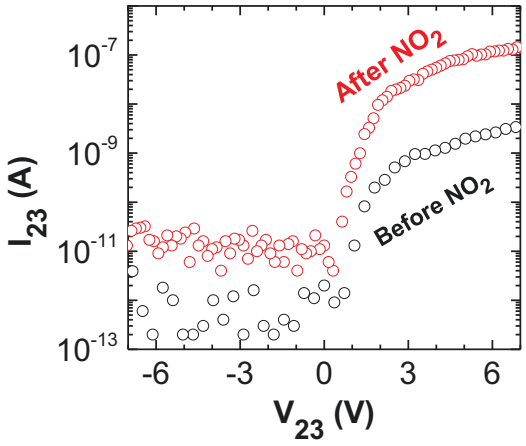

Figure S2. I-V characteristic when measuring between electrodes 2 and 3 (with 2 grounded, 3 biased) before and after NO_2 doping of the exposed WSe_2 region in the WSe_2/MoS_2 hetero-bilayer device. A back gate voltage of 50 V was applied.

5.3.2 TEM analysis

The lattice constants of the real lattices can be calculated from

$$\frac{1}{d^2} = \frac{4}{3}\frac{h^2 + k^2 + hk}{a^2},$$

where d is the length of the reciprocal lattice vector of the crystal lattice planes of (hk0) and a is the lattice constant of the chalcogenide crystal. This calculation yields a value of (4.4±0.1)% for the lattice mismatch between the WSe_2 single-layer and the underneath MoS_2 single-layer, which is nearly identical to their bulk value. The alignment of the two lattices can also be examined with a fast Fourier transform of the two zoomed-in TEM images in Fig. 5.1C in the main text, as shown in Fig. S3.

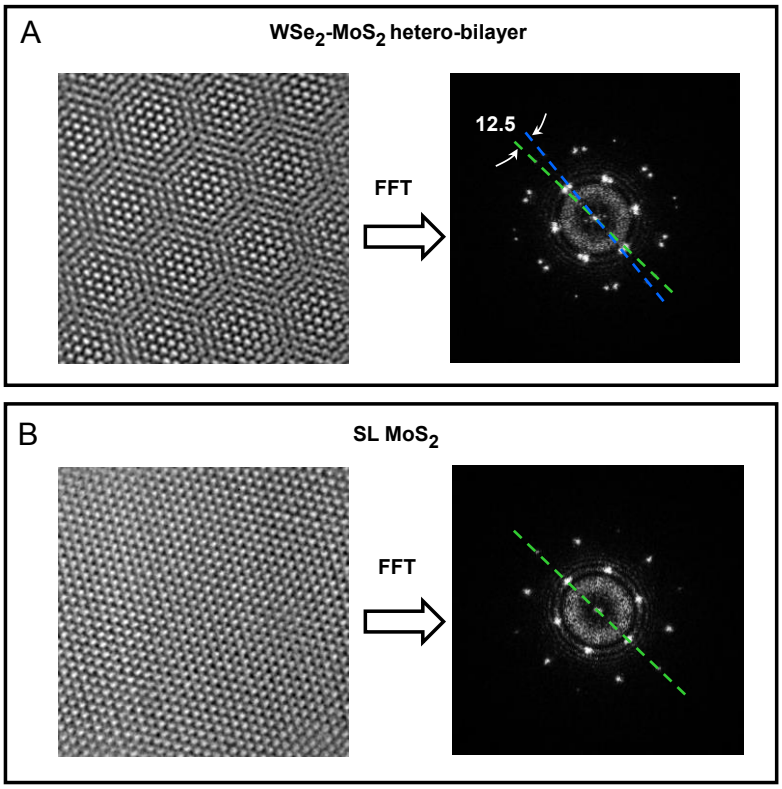

Figure S3. Fast Fourier transform of the HRTEM images shown in Fig. 5.1C in the main text for (A) WSe_2/MoS_2 hetero-bilayer. (B) single-layer MoS_2.

5.3.3 Raman characterization of the WSe_2/MoS_2 hetero-bilayer

There are four Raman-active modes for both WSe_2 and MoS_2, of which only A_{1g}, and E^1_{2g} modes were observed in our measurements due to the selection rule in the back-scattering configuration and the restricted rejection against Rayleigh scattering (7). As shown in Fig. S4, the in-plane E^1_{2g} mode peaks of WSe_2 and MoS_2 remained unchanged (within 0.5 cm^{-1}) comparing before and after transferring. This is a clear indication that there is no/negligible strain in either layer in the final hetero-bilayer, consistent with our TEM analysis. The out-of-plane A_{1g} mode peak red shifted by ~ 1 cm^{-1} (from 405.1 cm^{-1} to 404.1 cm^{-1}) for MoS_2, while for WSe_2 it's hard to detect as the A_{1g} peak is overlapping with the E^1_{2g} peak. This small red shift should be attributed to the interlayer coupling, which is also seen in bulk/few-layer WSe_2 and MoS_2 (ref. 7, 8).

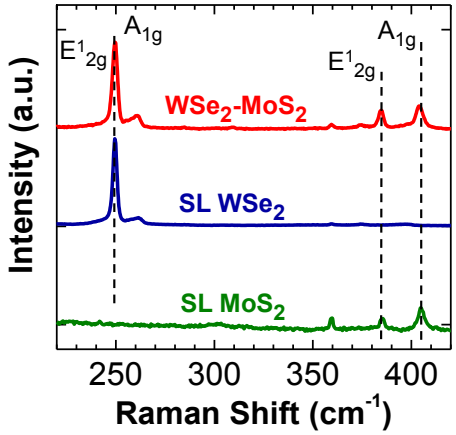

Figure S4. Raman spectra comparison for single-layer MoS_2 and WSe_2 and the WSe_2/MoS_2 hetero-bilayer. The excitation laser wavelength here is 532 nm.

5.3.4 PEEM experiment detail

As shown in Fig. S5A, a WSe_2/MoS_2 hetero-stack, which contained a single-layer WSe_2 on top of MoS_2 with thicknesses ranging from 1 single-layer (SL), 2 SLs and 4 SLs, was measured and analyzed by PEEM. Note that the thicknesses of the layers were determined by optical contrast, Atomic Force Microscope (AFM) in combination with PL. Figure S5B shows the W $4f_{7/2}$ binding energy position contour, where distinct boundaries between regions can be visualized and are consistent with our sample geometry. The binding energy map was obtained by a batch fitting of all spectra collected at different detector location, single peaks of W4f7/2 and Mo3d5/2 were simulated by a Gaussian profile. For more precise analysis, signal from homogeneous parts of the image were spatially integrated and more sophisticated fitting procedure (a combination of Shirley background and Doniach-Sunjic lineshape) was used (see Figure 5.2). For the single-layer WSe_2 in contact with the substrate, the W $4f_{7/2}$ binding energy is 33.78 eV, while for the single-layer WSe_2 on top of single-layer MoS_2, the W $4f_{7/2}$ binding energy is 33.56 eV. The W $4f_{7/2}$ core level binding energy decreased by ~ 220 meV when contacting to MoS_2, as noted in the text. The direction of the peak shift is consistent with a negative net charge on the WSe_2 in the WSe_2/MoS_2 hetero-bilayer as predicted by density functional theory (9). On the other hand, charge neutrality in the hetero-bilayer requires that a shift in the opposite direction is present on the MoS_2 component of WSe_2/MoS_2. As is shown in Fig. S5C, a shift of +190 meV with respect to stand-alone MoS_2 is observed indeed in the Mo 3d core levels of the WSe_2/MoS_2 (from 227.26 eV to 227.45 eV). The shifts in the W and Mo core levels are evidences that there exists charge transfer induced electric field between WSe_2 and MoS_2 layers. The hetero-bilayer can essentially be interpreted as being a two-dimensional dipole, an atomically thin parallel plate capacitor with van der Waals gap. One can also notice that the W $4f_{7/2}$ binding energy position shifted less when contacting to thicker MoS_2 layers by ~ 30 meV/layer. It is not clear at this stage which one of the three parameters, namely the charge transfer amount, layer distance or the dielectric constant in the van der Waals gap is playing a more important role in this slight decrease. Detailed density functional theory calculations are needed to further shed light on this issue.

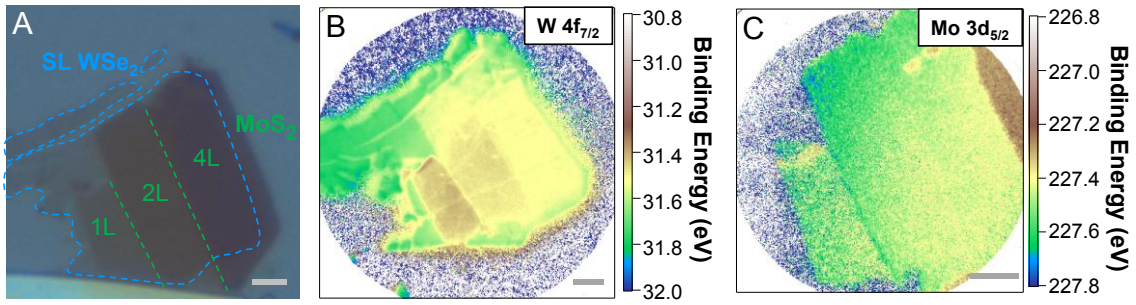

Figure S5. (A) The optical microscope image of the WSe_2/MoS_2 heterostructure for PEEM characterization. The PEEM sample was on a naturally (native) oxidized heavily p-doped Si substrate, while the image was taken when the sample was on Si/SiO_2 (260 nm) substrate. (B) W $4f_{7/2}$ binding energy position contour plot of the sample in (A). (C) Mo $3d_{5/2}$ binding energy position contour plot of the sample in (A). The scale bars are 2 μm.

5.3.5 Statistics of PL from different WSe_2-MoS_2 hetero-bilayer samples

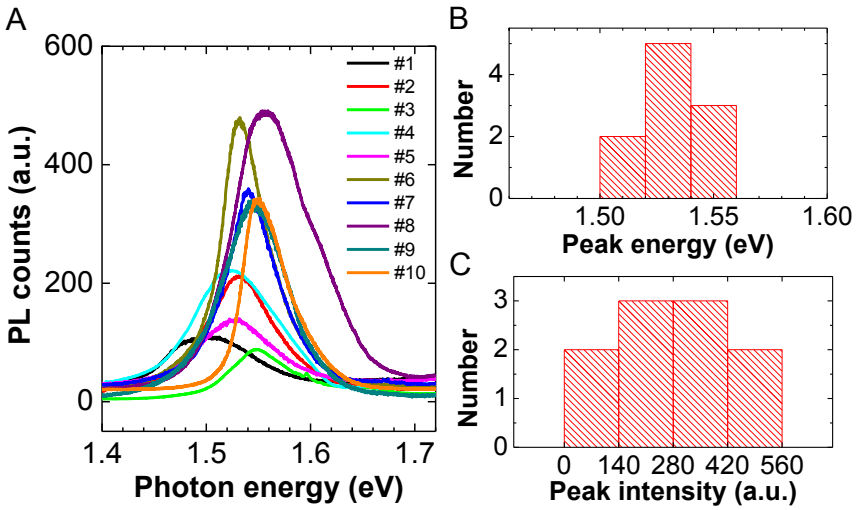

Figure S6. PL statistics of multiple WSe_2/MoS_2 hetero-bilayer samples. (A) PL spectra of 10 WSe_2/MoS_2 hetero-bilayers. (B) Histogram of the PL peak energies for these 10 samples. (C) Histogram of the PL peak intensities for these 10 samples.

5.3.6 Luminescence tail analysis

The band edge tail D(ν) as a function of frequency ν (also called the Urbach tail (10)), is related to the photon emission rate per unit energy by the van Roosbroeck-Shockley equation (11, 12). D(ν) can further be related to the photoluminescence spectrum I(ν) by,

$$D(\nu) \propto \frac{I(\nu)(e^{h\nu/kT} - 1)}{n_r^{\,2}\nu^2}$$

where h is Planck's constant, k is Boltzmann's constant, T is temperature and n_r is the real part of the refractive index. Figure S7 shows the shapes of the Urbach tails of single-layer WSe_2, single-layer MoS_2 as well as the WSe_2/MoS_2 hetero-bilayer. An optical semilog inverse slope of 30 meV/dec is extracted from all three tails, corresponding to the sharpness of the band edge. The nearly identical inverse slope of the hetero-bilayer proves that the band edge sharpness of the heterostructure can be as high as that of its constituent single layers.

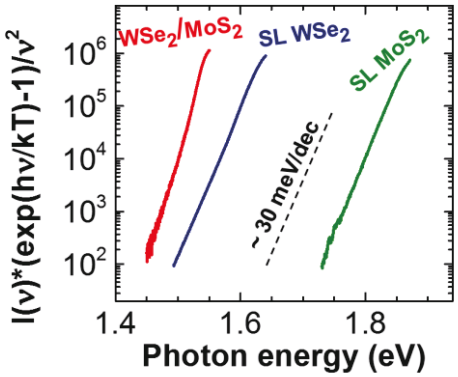

Figure S7. Band edge tails derived from the PL using the van Roosbroeck-Shockley equation, depicting the sharpness of the band edges. The spectra were normalized to peak magnitude.

5.3.7 Absolute PL spectra of WSe_2/MoS_2 heterostructure with h-BN

Figure S8 shows the absolute PL of WSe_2/MoS_2 hetero-stacks with single- and tri-layer h-BN spacers, along with the PL of single layer WSe_2. Interlayer coupling becomes negligible for the sample with a tri-layer h-BN spacer, as indicated by both the position and the intensity of the peak at 1.64 eV, which are nearly the same as single-layer WSe_2. The slight difference (0.01 eV) in the peak position is likely due to the fact that the boundary on the bottom side of WSe_2 has changed from SiO_2 to h-BN. On the other band, a single layer of h-BN does not fully suppress the interlayer interaction between WSe_2 and MoS_2. The PL spectrum of WSe_2/h-BN/MoS_2 shows a double peak feature centered at 1.6 eV with an intensity on the order of 1/3 of that of typical single-layer WSe_2. We interpret the lower energy peak component of the doublet as being the peak of the hetero-bilayer with reduced interlayer coupling due to the intercalation of the h-BN single layer. Indeed this peak falls in between the peak of the unperturbed single layer WSe_2 and strongly coupled WSe_2/MoS_2 bilayer. This demonstrates that the interlayer coupling can be readily tuned by intercalation of layered dielectric media into the van der Waals gap. The higher energy peak closely coincides with the peak of single layer WSe_2 and could be due to a competing spatially direct emission in single layer WSe_2 as the photo-generated electrons now see a BN barrier and would have certain probability of staying in the excitonic conduction band edge of WSe_2. This interpretation is also supported by the weak emission close to the position of single layer MoS_2.

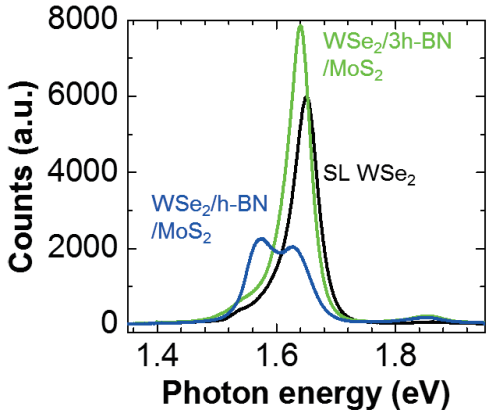

Figure S8. Absolute PL comparison of single-layer WSe_2, single-layer WSe_2/single-layer MoS_2 heterostructure with single- and tri- layer h-BN in between.

5.3.8 Electrical behavior of WSe_2, MoS_2 single layers

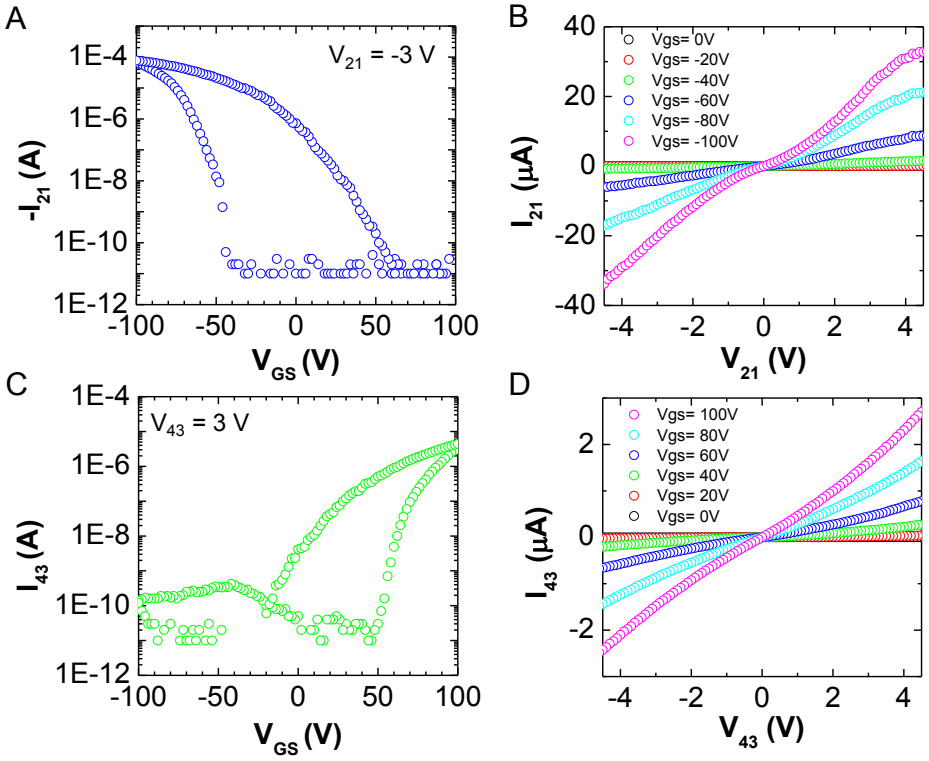

Figure S9. (A) Transfer characteristic of the single layer WSe_2 device in Fig. 5.4A of the main text (measured between terminal 1 and 2). (B) Output characteristic of the device in (A). (C) Transfer characteristic of the single layer MoS_2 device in Fig. 5.4A of the main text (measured between terminal 3 and 4). (D) Output characteristic of the device in (C).

References:

1. Novoselov KS, et al. (2004) Electric field effect in atomically thin carbon films. Science 306(5696):666-669.
2. Dean C, et al. (2010) Boron nitride substrates for high-quality graphene electronics. Nat Nanotechnol 5(10):722-726.
3. Ponomarenko L, et al. (2011) Tunable metal-insulator transition in double-layer graphene heterostructures. Nat Phys 7(12):958-961.
4. Fang H, et al. (2013) Degenerate n-Doping of Few-Layer Transition Metal Dichalcogenides by Potassium. Nano Lett 13(5):1991-1995.
5. Liu H, Neal AT, & Ye PD (2012) Channel length scaling of MoS_2 MOSFETs. ACS nano 6(10):8563-8569.
6. Fang H, et al. (2012) High-Performance Single Layered WSe_2 p-FETs with Chemically Doped Contacts. Nano Lett 12(7):3788-3792.
7. Zeng H, et al. (2013) Optical signature of symmetry variations and spin-valley coupling in atomically thin tungsten dichalcogenides. Sci Rep 3:1608.
8. Lee C, et al. (2010) Anomalous lattice vibrations of single-and few-layer MoS_2. ACS nano 4(5):2695-2700.
9. Terrones H, López-Urías F, & Terrones M (2013) Novel hetero-layered materials with tunable direct band gaps by sandwiching different metal disulfides and diselenides. Sci Rep 3:1549.
10. Urbach F (1953) The long-wavelength edge of photographic sensitivity and of the electronic absorption of solids. Phys Rev 92:1324-1324.
11. Van Roosbroeck W & Shockley W (1954) Photon-radiative recombination of electrons and holes in germanium. Phys Rev 94(6):1558.
12. Kost A, Lee H, Zou Y, Dapkus P, & Garmire E (1989) Band-edge absorption coefficients from photoluminescence in semiconductor multiple quantum wells. Appl Phys Lett 54(14):1356-1358.